Microfluidic Devices with Coarse Capillaries to Fabricate Bioengineering Products: Bubbles, Scaffolds and Nanoparticles

A thesis submitted in partial fulfilment of the

requirements for the degree of

Doctor of Philosophy

By

Xinyue Jiang

Department of Mechanical Engineering

University College London

Torrington Place, London WC1E 7JE, UK

Jan 2019

Declaration

I, Xinyue Jiang, confirm that the work presented in this thesis is my own. Where information has been derived from other sources, I confirm that this has been indicated in the thesis.

X

Xinyue Jiang

Abstract

Microbubbles fabricated by microfluidic techniques have garnered remarkable interest in many diverse fields for various applications such as ultrasound contrast agents, tissue engineering scaffolds and nanoparticles in drug delivery. Microfluidic T-junctions were used for this purpose owing to their ease of operation and fine control over the operation parameters. This thesis consists of two main sections: (1) microfluidic-assisted production of scaffolds and nanoparticles; and (2) multiple T-junctions for the reduction of microbubble size in size-restricted applications.

In section one, a single T-junction was used to produce microdroplets with pre-designed sizes for tissue-engineering applications. It was found that the scaffold structure and porosity can be tuned by altering the microdroplet size. Nanoparticles were formed by nanoprecipitation inside a microfluidic channel, inducing self-assembled polymeric particle patterns upon solvent evaporation. The processing parameters and materials properties were investigated for their effects on the sizes of microbubbles and nanoparticles.

In section two, the method of using multiple T-junctions to reduce microbubble size was explored. In some applications for microbubbles, size is a design constraint with smaller microbubbles being desired To overcome the limitation, the idea of combining multiple T-junctions with coarse capillaries for size reduction has been investigated. Firstly, a double T-

junction was assembled, and the effect of an additional T-junction on microbubble formation, stability and productivity has been thoroughly studied. A microbubble scaling prediction equation was proposed based on experimental data and the Garstecki equation. A triple T-junction was assembled to validate the proposed equation and to further reduce the microbubble size. Capillary number was introduced to investigate the microbubble fission regime. The critical capillary number was found experimentally to indicate the breaking and non-breaking microbubbles.

Thus, the microfluidic-assisted setup described in this work offers a feasible processing method for fabricating microbubbles, scaffolds and nanoparticles with good uniformity and low polydispersity index.

Impact statement

Honeycomb structure 2D and 3D scaffolds can be formed from microbubbles with good porous uniformity after bubble bursting and solvent evaporation. Porosity plays a vital role in scaffold formation. Uniform porosity can offer mechanical strength, good scaffold architecture and excellent cell proliferation. Microfluidic-assisted technique can produce scaffolds with desirable porosity and mechanical properties for various tissue engineering applications. Furthermore, 3D scaffolds can be achieved by stacking monodispersed microbubbles layer-by-layer. To fabricate the specially shaped scaffolds for tissue engineering applications, microfluidic devices can be incorporated into 3D printers. Various polymeric solutions can be applied in this setup for the regeneration of different types of tissues. For instance, 3D fabricated human nose shape scaffolds were produced in vitro to study the regeneration of replaceable noses.

Cancer nanotherapeutics are rapidly progressing and are being used to solve numerous limitations of traditional drug delivery systems; these include low biodistribution, poor water solubility, poor oral bioavailability and low therapeutic indices. To help the biodistribution of cancer drugs, nanoparticles have been made with desirable sizes and surface characteristics to boost the circulation time in the bloodstream. These nanoparticles can be also loaded with active drugs aimed at cancer cells to achieve targeted drug delivery.

Microbubble sizes of around 10µm are required in order for their use as ultrasound contrast agents. Capillary number is the main contributor for microbubble fission in triple T-junctions to reduce the size of microbubbles. This can be useful to design the future microfluidic devices to achieve microbubbles in the suitable range for ultrasound contrast agent's application.

This methodology described in this thesis has enormous potential in the preparation of microbubbles/droplets, scaffolds and nanoparticles with desirable sizes for versatile biomedical applications. The microbubbles/microdroplets produced in this work are highly monodispersed and offer the user with a good control over the operating parameters. The experimental setup can be scaled up by paralleling the T-junctions to increase productivity.

Table of Content

List of Tables

List of Figures

Acknowledgements

I would like to express my deep and sincere gratitude to my supervisor Professor Mohan Edirisinghe for the continuous support of my PhD study and related research, for his patience, motivation, and immense knowledge. His guidance helped me in all the time of research and writing this thesis. As a supervisor, he pushed me to develop my weaknesses and exploit my strengths. He gave me plenty of opportunities to deliver lectures, tutorials and demonstrations to practice my public speaking skills. He sent me to multiple international conferences and international research visits to improve my knowledge for multidiscipline research fields. I could not have imagined having a better supervisor and mentor for my PhD studies.

Many acknowledgements equally go to my second supervisor, Dr. Maryam Parhizkar, for her insightful comments and encouragement and considerable valuable advices which made me to broaden my research from various perspectives.

I would like to express my thanks of gratitude for my collaborators Dr. Merve Gultekinoglu and Dr Cem Bayram who gave me the golden opportunity to visit the University of Hacettepe and allowed me to experience various analytical technologies, which also collaborated with me in doing numerous researches and came to know so many cross-discipline knowledges. I really appreciate their friendship, encouragement and timely support.

I would send my special thanks to my friends and family. The days would have passed far more slowly without the support of my friends: Maryam

Crabble-mann, Yue Zhang, Ahmet Topcu, Amalina Amir, Ahmad Shah Idil, Sihong Chen, Xu Zhang, Lei Cheng etc., whom I thank for providing such a rich source of conversation, education and entertainment. I would like to thank Henry Lancashire especially, without his brilliant mind, timely support and constructive advice, I could not able to finish my triple T-junction paper.

Very sincerest thanks go to my parents and grandparents, Zhongwen Jiang and Ying Pan, Boqi Jiang and Ranfang Mi, who have been excellent for years and always love me, encourage me and support me to pursue my dreams. I am grateful for my family for always being there for me. I am forever indebted to my parents and grandparents for giving me the best opportunities they can give, and those opportunities and experiences that have made me who I am. They selflessly encouraged me to explore new directions in life and seek my own destiny. I would never be able to finish my PhD and enjoyed so many opportunities without the support from my family. A special thanks go to Wangcai, who's such a great company for my mom, when I am not around her.

I would like to thank my boyfriend Dr. Wai Keith Lau, who's always been there for me to encourage, love and support me. Thanks for taking time to proofread my thesis drafts and for many constructive suggestions. Thanks for encouraging me to become a better person and motivating me to achieve my dream. Thanks for the emotional support, for being understanding, for tolerating my temper, and for being such a great friend. I am so lucky to have you on my side.

Publication, Award & Conference Presentations

- **Publications**

1. X. Jiang, Y. Zhang, M. Edirisinghe and M. Parhizkar, Combining microfluidic devices with coarse capillary to reduce the size of monodispersed microbubbles. RSC Advances, DOI: 10.1039/C6RA09802A.

2. M. Gultekinoglu, X. Jiang, C. Bayram, K. Ulubayram and M. Edirisinghe, Honeycomb-like PLGA-b-PEG structure creation with T-junction microdroplets. Langmuir2018, 34, 27, 7989-7997, DOI: 10. 1021/acs.langmuir.8b00886 (X. Jiang and M. Gultekinoglu contribute equally to this work).

3. M. Gultekinoglu, X. Jiang, C. Bayram, K. Ulubayram and M. Edirisinghe; Generation of self-assembled micro stripe polymer patterning by sessile nanofluid droplets. Submitted to Nanoscale. (X. Jiang and M. Gultekinoglu contribute equally to this work).

4. C. Katsakouli, X. Jiang, W. Lau, J. Rohn and M. Edirisinghe; Generating Antibacterial microporous structure using microfluidic processing. *ACS Omega*, 2019, 4 (1), pp 2225–2233; DOI: 10.1021/acsomega.8b02573.

- **Conferences and awards**

1) Conferences

1. Xinyue Jiang, Maryam Parhizkar, Mohan Edirisinghe. Production of monodispersed microbubbles using capillary embedded T-junction microfluidic devices, UCL Mechanical Engineering PhD Students Conference 2015, 25 June 2015, Oral Presentation and Poster.

2. Xinyue Jiang, Maryam Parhizkar, Mohan Edirisinghe. Combining microfluidic devices with coarse capillary to reduce the size of monodisperse microbubbles, UCL Mechanical Engineering PhD Students Conference 2016, 31 May 2016, Oral Presentation and Poster.

3. Xinyue Jiang, Maryam Parhizkar, Mohan Edirisinghe. Microfluidic device with coarse capillaries to generate monodispersed PLGA-b-PEG microdroplets as porogen for honeycomb shaped structure, Material Research Society spring 2018 (MRS 2018), 4 April 2018, Oral presentation.

4. Xinyue Jiang, M. Gultekinoglu,. Bayram, K. Ulubayram and M. Edirisinghe. Generation of self-assembled micro stripe polymer patterning by sessile nanofluid droplets. Submitted to Nanoscale, the Minerals, Metals and Materials Society 2019 (March 2019), 14 March 2019, Oral presentation.

2) Awards

Xinyue Jiang. Combining microfluidic devices with coarse capillary to reduce the size of monodisperse microbubbles, Best Presentation Biomechanical Engineering Group, UCL Mechanical Engineering PhD Students conference 2016, 31 May 2016, Oral presentation.

Xinyue Jiang, joint fund by UCL mechanical engineering department and University of Hacettepe, establish a microfluidic laboratory in nanotechnology department at University of Hacettepe (Turky), Oct-Nov, 2018.

Chapter 1 Introduction and background

1.1 Introduction and background of microbubbles

Microbubbles, widely defined as bubbles with diameters in the range 1-1000μm, have numerous applications in scientific fields, such as in food and chemical industries (G. Campbell, 1999), oil and energy generation (Mikhailov, 2012), cosmetic and agricultural technologies (Ikeura, Kobayashi, & Tamaki, 2011; M. Parhizkar, Edirisinghe, & Stride, 2013). In addition, microbubbles are in great demand in the biomedical field for use as contrast agents and thrombus destruction (Ferreira & Trierweiler, 2009), drug carriers and gene delivery (Unger et al., 2002), and for bacterial scavenging and biosensing (Suntharavathanan Mahalingam, Xu, & Edirisinghe, 2015). Microbubbles can also be used to generate monodispersed honeycomb-like 2D or 3D scaffolds for tissue engineering application (Gultekinoglu, Jiang, Bayram, Ulubayram, & Edirisinghe, 2018). The burst of microbubbles can generate polymeric nanoparticles with narrow size distribution, which can be used as targeted drug delivery carries (Elsayed, Kothandaraman, Edirisinghe, & Huang, 2016). Microbubbles Different applications can have various requirements on microbubble size and size distribution, therefore the precise control of these is an essential factor, for example key biomedical uses of microbubbles such as ultrasound imaging and drug delivery demand the generation of near-monodisperse microbubbles in the 2-8 μm diameter range which are stable over a longer duration. Several methods have been utilised to produce microbubbles, including sonication (Q. Xu, Nakajima, Ichikawa, Nakamura, & Shiina, 2008a) , ink-jet printing, coaxial electrohydrodynamic

atomization and gyration (Farook, Stride, & Edirisinghe, 2009; Kukizaki & Goto, 2007; Suntharavathanan Mahalingam et al., 2015; Q. Xu, Nakajima, Ichikawa, Nakamura, & Shiina, 2008b). However, a major problem with all of these methods is the lack of total monodispersity of microbubbles produced (Peng et al., 2015).

In contrast to other microbubble making methods, microfluidic technology is one of the most promising tools to generate microbubbles due to its capability of consistently generating monodisperse microbubbles. However, the microbubble size formed is critically dependent on the size of capillaries used and therefore, for solutions with high viscosity, the production of fine microbubbles becomes difficult with this technique (Günther & Jensen, 2006). New attempts have been made to ease microbubble production in microfluidics, for instance, with multi-array microchips and the use of sudden deepened configuration in the micro-channel (Peyman et al., 2012; Shih, Hall, Hill, & Lee, 2013). Depending on the flow pattern and the output product characteristics, microfluidics are categorised into three main geometries: co-flowing, flow focusing and cross-flowing (Fu, Ma, Funfschilling, & Li, 2009; L. Q. Wang & Zhang, 2009; Xiong, Bai, & Chung, 2007) T-junction cross-flowing devices are one of the simplest and most reliable geometries for production of monodispersed microbubbles (Thorsen, Roberts, Arnold, & Quake, 2001). A remarkable advantage of the T-junction device in addition to reusability and cost efficiency is the control over the flow rate and hence reproducibility of microbubble formation satisfying similar criteria.

Albumin is extensively used as a stabilizing shell for microbubbles (M. Borden, 2010). It is often heated to denature and cross-link to form a stable shell for microbubbles.

Microbubbles produced with non-cross-linked albumin have a higher liquid-vapour pressure and as a result they are less stable than the cross-linked albumin-shell microbubbles. Achieving cross-linked albumin-shell microbubbles through microfluidics devices is difficult, resulting in very few dedicated investigations into production of stabilized albumin microbubbles, thus extending the stability of these in other ways are in demand at present. The production of bovine serum albumin (BSA) microbubbles, as biocompatible and non-toxic templates for scaffolds, has been previously investigated (Chen et al. 2014; Parhizkar, Sofokleous, et al. 2014; Nair et al., 2006). The pore size of the scaffold plays an important role in cell binding, migration and ingrowth, and microfluidic techniques can facilitate the formation of uniform microbubble templates for scaffolds having ordered and homogenous porous textures (Lien, Ko, & Huang, 2009). In this work, BSA as the main polymer has been used in single T-junction and modified double and triple T-junctions to further reduce the size of microbubbles for the biomedical application such as ultrasound contrast agents. Additionally, to explore the potential of microfluidic method for fabrication of biomedical products such as scaffolds and nanoparticles other than microbubbles, PLGA-b-PEG amphiphilic polymer was also used to generate scaffolds and nanoparticles through single T-junction microfluidic device. For microbubble biomedical application, a new microfluidic system is firstly proposed as a possible route to produce monodispersed microbubbles where coarse (200µm diameter) capillaries are used and several T-junctions are combined in series to attain the desired microbubble size. To demonstrate this advance, two capillary embedded T-junction devices were aligned in series in order to provide a simple geometry that provides two inlets for liquid flow and one to provide gas into the microchannels. For

the purpose of hydrodynamic analysis and to investigate how the addition of the second T-junction affects the size, structure and stability of microbubbles, both liquid inlet channels were fed with the same BSA solution. Thus, a comparative study on microbubble formation with the single T-junction setup has been possible and we put forward a scaling model which can predict the microbubble diameter generated by putting together more than one T-junction. Reduction of the microbubble size to < 10 μm diameter and modifying the microbubble chemistry (by using different materials and surfactants) were not specific aims of this work, however we demonstrate using our predictive model on how our new apparatus can be used to form microbubbles of < 10 μm by combining several junctions. In addition, two verification experiments did to check the correctness of the above results. In the first experiment, material has been changed from 15 wt. %BSA to 50 wt. % glycerol mixed with 2 wt. % polyoxyethylene 40 stearate to test whether it is the result of material properties of BSA to reduce the diameter of microbubbles produced from double T-junction. The following experiment is combining three T-junctions together to generate monodispersed microbubbles in order to verify whether the experimental result is still following the predicted trend proposed in this work by increasing the number of T-junctions. Microbubbles which size is around 10 μm were produced in this work, which increase the possibility of microbubbles produced in microfluidic methods as ultrasound contrast agents and therapeutical drug delivery carrier. Moreover, in this work, in order to erase the weakness of traditional double layer preparation process, a new microfluidic double T-junctions are introduced to try to generate double layered microbubbles in the future, based on the extraordinary geometry properties of double T-junction such as its good stability and production of

smaller monodispersed microbubble diameter. Later, microbubble size was further reduced by microbubble fission regime inside triple T-junction device. The critical capillary has been found as an indicator for breaking and non-breaking microbubbles. These results are useful for fabrication microfluidic devices for minimized microbubbles as polymer reactors.

1.2 Objectives of the research

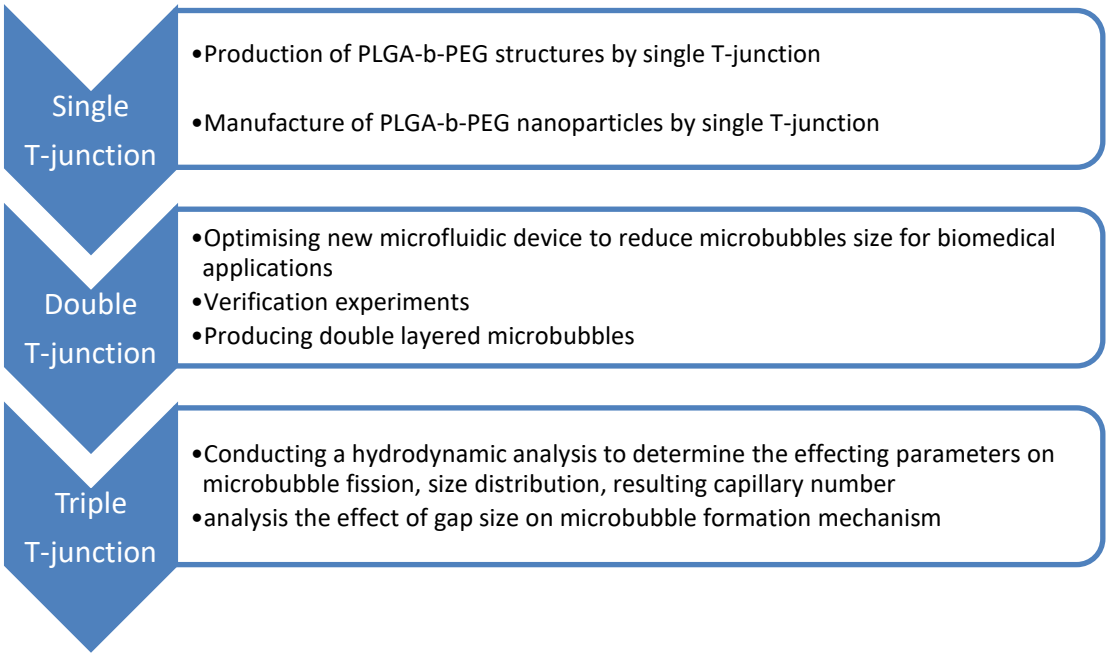

Figure 1-1: objectives of the research in this thesis

This thesis focuses on a microfluidic technique that utilises T-junction devices. In this work bubble reduction and bioengineering product fabrication were explored. Products such as microbubbles and nanoparticles were produced to form scaffolds for tissue engineering applications. There are numerous other techniques used to develop these bioengineering products such as the traditional microbubbling and scaffold production techniques of sonication, agitation, gas foaming and electrospinning, and the conventional nanoparticle fabrication methods of dispersion

polymerisation and solvent evaporation. The major drawbacks of these techniques are; lack of uniformity for microbubble formation, causing irregular spatial architecture for scaffold generation and the need for post-processing steps in nanoparticle fabrication. In chapter 4 section 4.1, a microfluidic, single T-junction was investigated to assess its potential as a versatile processing technique to produce microbubbles with a confined uniformed size and good stability, scaffolds with desirable porosity and nanoparticles with easy fabrication and size uniformity. Meanwhile, the operation parameters and solution properties were taken into consideration as the factors influencing the formation and size distribution of microbubbles, scaffold porosity and nanoparticle sizes. The drawback of the microfluidic technique is the relatively low yield. To solve this demerit, in Chapter 4 section 4.2, double T-junctions were assembled in order to enhance the productivity. Additionally, the microbubble size was reduced by using the double T-junction device compared to the single T-junction under the same conditions. Using this device, double layered microbubbles were also generated. In Chapter 4 section 4.3, a triple T-junction was assembled to further bring down the size. A bubble fission regime was identified at the third T-junction of the triple T-junction device bringing the size down further, the reason has been further investigated. The relationship among capillary number and gas pressure, liquid flow rate and gap size has been systematically studied separately. The experimental critical capillary number has also been found, where the critical capillary number can be a indicator to predict future bubble fission.

1.2.1 Production of bubbles, scaffolds and nanoparticles by single T-junction microfluidic device

The main aim of this research was to determine the parameters affecting the bubble/scaffolds/nanoparticles size and formation in a single T-junction device. Additionally, the purpose was to illustrate that single T-junction microfluidic device can successfully generate not only microbubbles but also scaffolds and nanoparticles and influence their size and formation under ambient pressure and temperature.

1.2.2 Optimised microfluidic device- double T-junction

For biomedical applications such as ultrasound contrast agents, microbubble size must be less than 8 μm to avoid embolism in blood vessels. This part of the research was focussed on the modification of the basic single T-junction by addition of another standard T-junction in parallel to generate bubbles with reduced size and offers a potential way to produce double layered microbubbles. The objective of this work is to investigate the effect of operation parameters in conjunction with the extra T-junction on bubble size and formation. The effect of outlet tubing length on microbubble formation has been studied. A triple T-junction was assembled to further bring down the size of monodispersed microbubbles.

1.2.3 Modified microfluidics device-Triple T-junction

The effect of the operation parameters in conjunction with capillary number on microbubble fission regime was studied thoroughly. By tailoring the parameters, microbubbles with diameters around 25 μm were achieved. This study demonstrated the potential of reducing the size of microbubbles via optimising microfluidics system for biomedical application.

1.3 Structure of this thesis

This thesis is processed by surveying literature review, setting up the experimental equipment, selecting materials and methods, and eventually performing experiments in order to explore the potential available in microfluidic devices as an operable device to generate microbubbles for biomedical and industrial applications.

Chapter 1 demonstrates a general introduction, background and research goals of this project.

Chapter 2 provides a literature review, where the viable industrial applications of microbubbles are illustrated. The stability of microbubbles is discussed. Additionally, the currently widely used microbubble preparation technologies have also been discussed in this section. Moreover, scaffolds and nanoparticles generated from microbubbles are also described in this section.

Chapter 3 shows the experimental setup and material properties employed in this project.

Chapter 4 Results and discussion

Chapter 4 section 4.1 presents the experimental results and discussions of single T-junction and its bioproducts such as bubbles/scaffolds/nanoparticles.

Chapter 4 section 4.2 describes the experimental results and discussion of double T-junction and its application: double layered microbubbles.

Chapter 4 section 4.3 describes the experimental results and discussion of triple T-junction.

Chapter 5 provides the conclusion driven from experimental results and future works.

Chapter 2 Literature review

2.1 Introduction

The aim of this literature review is to demonstrate an outline of techniques to produce microbubbles which are suitable for the basic criteria in food industries, cleaning technology, cosmetics, and for diagnostic imaging and therapeutic applications as ultrasound contrast agents and drug/gene delivery vehicles, and for generating scaffolds and nanoparticle from monodispersed microbubbles. In order to satisfy this aim, this literature review surveys the applications, properties, preparation and formation of microbubbles that are extensively used in different aforementioned industries.

2.1.1 Definition of microbubbles

Microbubbles are gas filled microspheres which shown below (Figure. 2-1). Due to the remarkable property characteristics of microbubbles, this technology have been investigated widely in many areas (Ago et al., 2005). For example, based on high surface area to volume ratio of microbubbles, they are excellent media for mass and energy transfer, which characteristic has been extensively used in marine products to increase the growth rate by enhancing oxygen mass transfer rate (Ago et al., 2005). Due to the long stagnation property of microbubbles, they can be used as a natural collector because of large surface area and comparatively slow rise velocities under water. Therefore, this property of microbubbles are widely applied in water and waste water purification treatment (Cassell, Kaufman, & Matuevic, 1975; Takahashi et al., 2003). For instance, when microbubbles flow up in waste water, they interact

with organic pollutants and then take them to the surface to form a collective foam layer for further separation processes (Rodrigues & Rubio, 2007). Because of microbubbles' high compressibility and good acoustic response to ultrasound signal, they act as ideal tool for ultrasound contrast agents (Dijkmans et al., 2004).

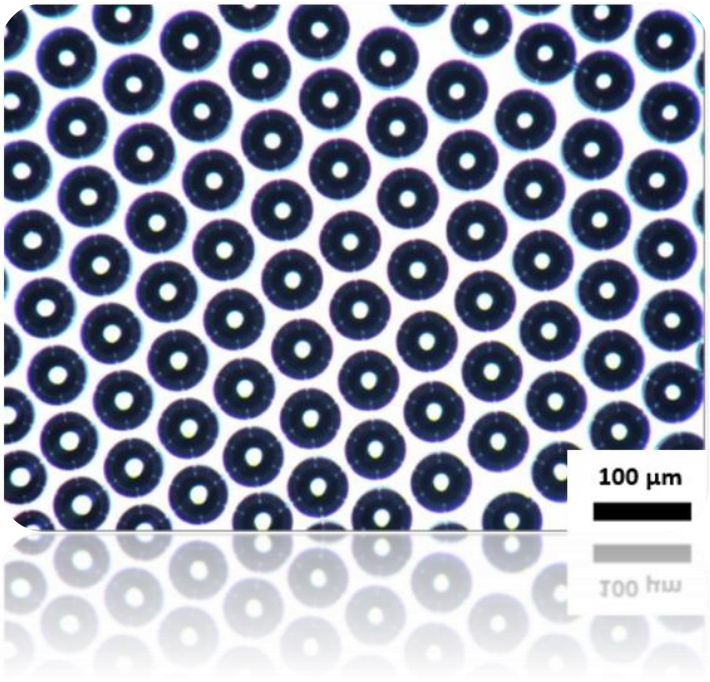

Figure. 2-1: monodispersed microbubble sketch

2.1.2 Application of microbubbles

Due to different applications and industries, the requirements of microbubbles properties such as size, size distribution and stability also vary widely.

2.1.2.1 Food industries

Bubbles play a significant part in many food products such as beers, cakes, ice creams and breads (G. M. Campbell & Mougeot, 1999). The reason why bubbles are extensively used in food industries is due to bubbles reducing the manufacturing

costs resulted from lowering the density of products, enhancing food mouthfeel and appearance owing to altering the texture and rheology and also increasing digestibility (G. Campbell, 1999; Zúñiga & Aguilera, 2008). For example, microbubbles create the creaminess of aerated chocolate bar, the fizziness of sparkling wine or champagne (Figure. 2-2) and softness of sponge cake (G. M. Campbell & Mougeot, 1999).

There are a lot of advantages from aerated food such as calorie reduction, food preservation, nutrition enrichment (Q. Xu et al., 2008b). For baked products, bubbles used in bread and cake can enhance the taste as well as softness, sweetness and volume (G. M. Campbell & Mougeot, 1999; Lau & Dickinson, 2005). For low-calorie food, in pastry baking, flour sugar is converted into CO2 which lost from pastry leading to lower calorie during fermentation procedure (G. M. Campbell & Mougeot, 1999). For food preservation, food appearance and shelf-time are dependent on the air amount dissolved in food, size distribution and stability of bubbles added in the food (Lau & Dickinson, 2005). In addition, not only the taste but also the nutrition value of food can be amended by adding dispersions of microbubbles. For nutrition enrichment, nourishing food can be achieved by adding microbubbles coated with nutritional ingredients or drugs as a food medical aid (Y. Shen, Longo, & Powell, 2008).

Figure. 2-2: The collapse of plenty of microbubbles on the glass surface radiates the cloud of droplets which create the sensual mouthfeel taste (Liger-Belair, Polidori, & Jeandet, 2008)**.**

2.1.2.2 Cleaning technology

Microbubbles have potential as cleaning agents, which can be produced by ultrasound, laser and hydrodynamic techniques (Verhaagen & Fernández Rivas, 2016). Microbubbles as cleaning agents are well used in dental clinic, clothing and textiles, heavy industries and waste water treatment (Mason, 2016).

- Dental clinic application

In dental hygiene clinic, different dental hygiene problems caused by various personal hygiene and dietary habits contributed to many oral bacterial strains attached in cavity (Guggenheimer & Moore, 2003). Dental plaques is one of the dental hygiene problems caused by bacteria accumulation on the surface of the teeth and mucosa

(Kapellas et al., 2014). It has been shown that ultrasound-induced microbubbles have a sufficient efficacy to remove oral dental plaques as well as reduce the risk of periodontal disease development (Lin, Chuang, & Chang, 2015). Ultrasound-induced microbubbles formed by air disintegration in the water absorbs detergent solution to enhance the contact surface between detergent air microbubbles and the exposure surface of teeth, resulting in reducing the bacteria accumulation on the surface of teeth, and further enhance the dental cleaning ability (Lin et al., 2015). The bacteria removal experiment can present the oral plague cleaning efficiency by ultrasound introduced microbubbles in tooth hygiene applications (Figure. 2-3). The cleaning efficiency was evaluated by the amount of dental plagues removed (Nance et al., 2013; Sharma, Gibcus, Van Der Mei, & Busscher, 2005). Figure. 2-3 suggested the variation of bacteria accumulation on tooth surface before and after applying ultrasound-introduced microbubbles cleaning technique (Lin et al., 2015).

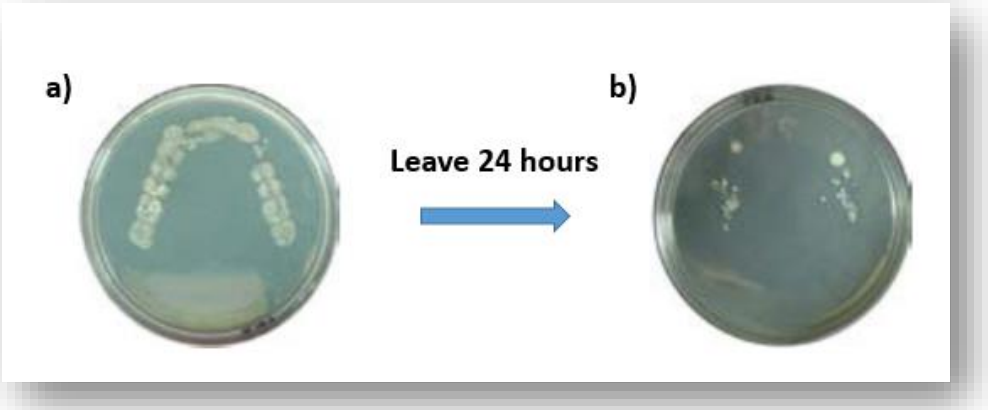

Figure. 2-3: Bacteria formation a) initial bacteria on tooth tray surface without microbubble cleaning; b) bacteria on the same tooth tray after 1 day with microbubble cleaning process (Lin et al., 2015)**.**

- Clothing and textiles application

In fabrics and textiles, conventional laundry methods are front-loading tumbler and top-loading washers which often contribute to heavy clothing damage because of fabric deformation and friction (Gotoh, Harayama, & Handa, 2015; Seeber, 1989). Organic commercial dry-cleaning solvents used for delicate fabrics have side effects on human and environment due to their toxicity and pollution (Uzma et al., 2008). Ultrasound has been applied into textiles cleaning due to its extraordinary oily soils removal ability from the polyester fabric without health issues and environment impacts (Gotoh et al., 2015). Cavitation, driven by ultrasound waves, is defined as the reason for generation of vapour bubbles in a liquid relevant to a sudden pressure drop under vapour pressure, whilst leading to increase liquid temperature (Hutli et al., 2016). Under ultrasound high intensity and pressure, bubble implosion happens and produces intense pressure pulses and shock waves which generate high stresses to remove the adjacent contaminants on material surface. As a results, the generation and deformation of cavitation bubbles play a significant role in ultrasound cleaning process (Chahine, Kapahi, Choi, & Hsiao, 2016). However, applying the high intensity ultrasound may increase textile surface roughness.

Ultrasound cleaning method not only works on soft materials such as fabrics and textiles but also have used in hard substrates like machines in heavy industries (Gotoh et al., 2015). The reasons why ultrasound is very helpful for surface decontamination are based on two facts; one is due to the formation of powerful jet, produced from the deformation of cavitation bubbles, emitting on the surface to dislodge dirt and bacteria. Another is based on exposure to the surface adhering dirt

due to the reduction of boundary layer surface thickness made by acoustic waves (Mason, 2016).

Figure. 2-4: Diagram of microbubble cleaning procedure (Cassell et al., 1975)

Figure. 2-4 shows microbubbles used in cleaning techniques have high surface area and relatively slow rise velocities. When microbubbles absorb oil residues, they interact with oil residue or small particles and then carry dirt to the surface to generate a collective foam layer for further separation and purification (Cassell et al., 1975; Rodrigues & Rubio, 2007).

2.1.2.3 Ultrasound contrast imaging

In the past decades, ultrasound imaging has been used as an imaging modality with plenty of applications, such as left ventricular opacification enhancement and Doppler signal intensity increase (Dijkmans et al., 2004). owing to its excellent safety, low cost and easy accessibility (Kang & Yeh, 2011), ultrasound contrast imaging is one of the most widely used medical diagnostic methods among other diagnostic imaging modalities such as computed tomography, positron emission tomography, and magnetic resonance imaging (MRI). However, due to the relatively low image quality

taken by ultrasound imaging technique, the methods to improve the contrast image becomes a key point amongst researchers (Dijkmans et al., 2004).

Microbubbles have become the most popular and effective type of contrast agents in ultrasound imaging since the late 1960s (Dijkmans et al., 2004; E Stride & Saffari, 2003). Microbubbles can enhance the sensitivity of conventional ultrasound imaging due to their superior compressibility and acoustic property (Kang & Yeh, 2011; E Stride & Saffari, 2003). Because of their compressibility, microbubbles oscillate volumetrically in an ultrasound field and therefore scatter more energy than conventional rigid ultrasound contrast agents of the same size (E Stride & Saffari, 2003). Due to their extraordinary acoustic property, microbubbles can respond with linear or non-linear oscillations to different ultrasound acoustic pressures, which creates an acoustic impedance mismatch between blood vessels and surrounding tissues in medical diagnostic imaging (Dijkmans et al., 2004) shown in Figure 2-5. It has been shown that more stable microbubbles composed of inert gas such as nitrogen or perfluorocarbon and coated with biodegradable material such as albumin, phospholipids, or polymers are the most effective methods of contrast enhancement in ultrasound imaging and multifarious commercial contrast agents (Dijkmans et al., 2004; Kang & Yeh, 2011). Size of microbubbles is also a crucial factor to enhance the acoustic properties (Gorce, Arditi, & Schneider, 2000). For instance, polydispersed microbubbles have uncontrolled broad uniformities of sizes and shell thickness which cause a wide acoustic responses (Abbaspourrad et al., 2013). Microbubbles with diameters smaller than 1 μm generate minimal acoustic contrast (Gorce et al., 2000; Soetanto & Chan, 2000). Larger microbubbles produce increased

acoustic contrast, but when the microbubble size is larger than 10 µm, they are rapidly filtered by lung. Additionally, microbubble size around 10 µm can increase the risk of an embolism (Butler & Hills, 1979; Fonslow et al., 2013). Microbubble destruction and contrast loss is dominated by the gas exchange in the alveoli (Wong et al., 2004). Smaller size microbubbles can efficiently travel cross lung pulmonary capillary beds, whereas bubble size larger than pulmonary capillaries are trapped (Shashank, Jameel, James, Shunichi, & Mark, 2010). Once the bubbles are occluded in the lungs, elimination takes place predominantly by the alveoli and, to a lesser extent, gas can be absorbed by the surrounding blood and tissues (Katz, Leiman, & Butler, 1988).The elimination rate of larger microbubbles is matched by alveolar excretion at a rate mainly dominated by pulmonary artery pressure (Verstappen, Bernards, & Kreuzer, 1977). By administrating a microbubble suspension to the blood, the ultrasound image contrast between their gas core and surrounding tissues is enhanced by several orders of magnitude (Cui et al., 2005; Kang & Yeh, 2011).

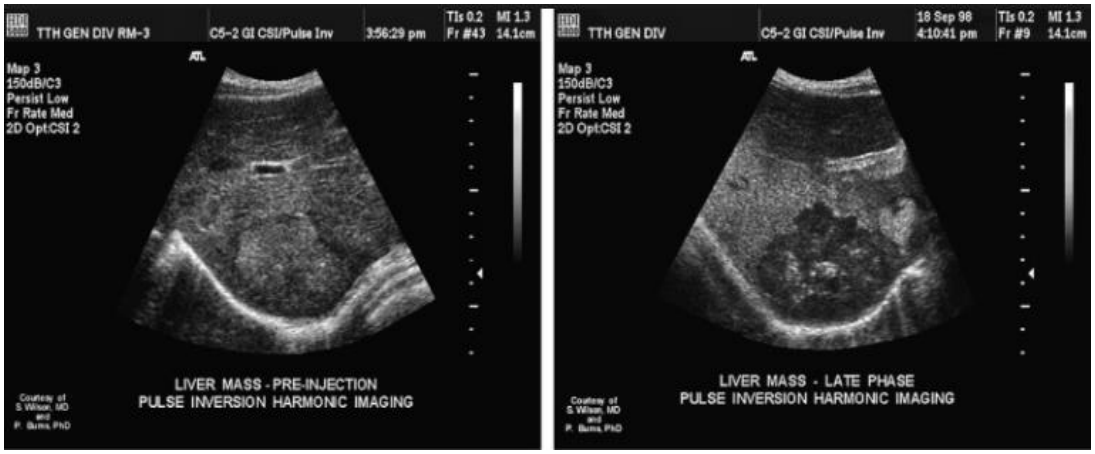

Figure 2-5: Ultrasound image of a liver without (left) and with (right) ultrasound contrast agents (Kremkau et al., 2015).

2.1.2.4 Therapeutic applications

Gas encapsulated microbubbles not only can be used as medical diagnostic imaging modality but also can be employed in therapeutic applications such as drug and gene targeted delivery carriers (Dijkmans et al., 2004). The basic aim for drug delivery and targeting is to enhance the efficiency of drug action in the affected region whilst lowering undesired side effects, for example toxicity, in the healthy tissues. Ultrasound irradiation has been added to improve the delivery of drugs and therapeutic genes, which allows microbubbles to be easily focused and penetrate more deeply into the tissues in microbubble intravascular ultrasound treatment (Hernot & Klibanov, 2008b). In gene and drug therapeutic treatment, the demanded therapeutic ultrasound agents are loaded in microbubbles, where they could be tracked to the affected region in human body via applying low-intensity ultrasound and further the pay-loaded agents are released locally by destroying the microbubbles through a high intensity burst and, as a consequence, avoiding side effects such as toxic chemotherapy (Eleanor Stride, 2009). Cell and tissue permeability can also be increased by destroying microbubbles loaded with a required therapeutic gene or drug. Destruction of microbubbles can produce high-energy microstreams, or microjets, which can generate high shear stress on the cell membrane and furthermore enhance cell permeability to increase drug deposition in tissues and cells (Dijkmans et al., 2004; Kang & Yeh, 2011). Figure. 2-6: demonstrates the mechanism of microbubbles as drug delivery carries after intravenous administration. Cancer cells have been targeted by applying external ultrasound. Cell membranes have been blasted via high intensity focused ultrasound. The broken

membranes allow the drug loaded microbubbles to enter in short period of time. Eventually, drug can be released to destroy cancer (Schantz, 2014).

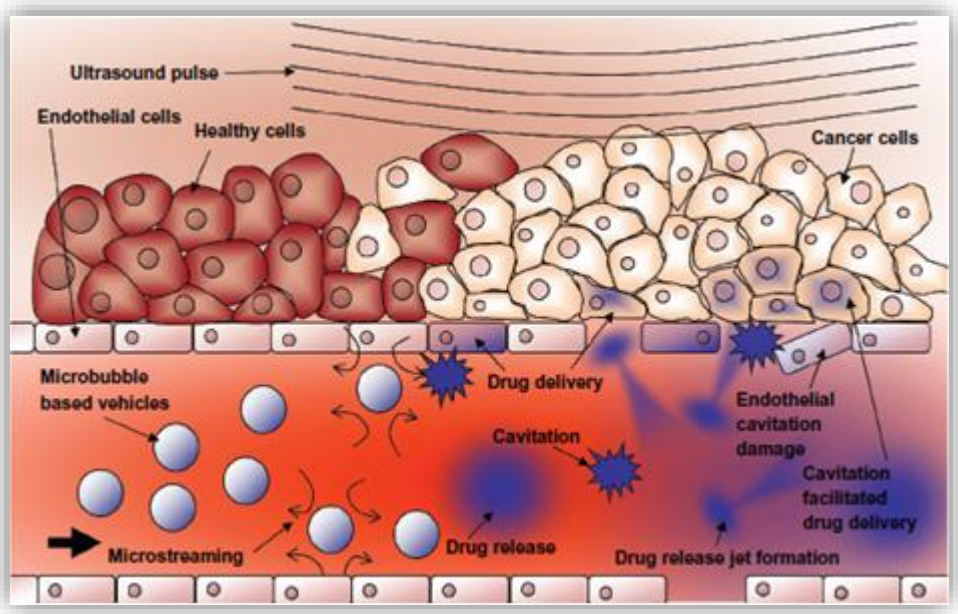

Figure. 2-6: Ultrasound aided microbubble drug delivery graph (Schantz, 2014)

2.1.2.5 Scaffolds for tissue engineering and regeneration

Tissue engineering arose two decades ago as an innovative method to repair and regenerate traumatized tissues of the human body. Tissue engineering commonly incorporates living cells with biodegradable and biocompatible substances i.e. scaffolds (O'Brien, 2011; M. Wang & Sultana, 2012). Scaffolds play a vital role in tissue engineering and regenerative medicine as porous substances engineered with various bio-products such as cells, drugs, genes and proteins (O'Brien, 2011). Scaffolds act as extra cellular matrices to offer temporary templates at the defect site until the injured tissue is repaired or regenerated and its further biomechanical function is restored. To fulfil this purpose, scaffolds should firstly offer sufficient porosity to promote cell viability, proliferation and differentiation. The porosity

which is defined as volume of pores to volume of substances should ideally be comparatively high (50-90%) (Karimpoor et al., 2018). Scaffolds should be engineered with high porosity where pores are both connected with each other and with the material surface. Pore interconnectivity is necessary for cell adhesion, tissue ingrowth and transportation of nutrients, oxygen and waste. The existence of isolated pores prohibits the gas and fluid diffusion between cells. However, the high surface pore size, matrix pore interconnectivity and architecture integrity affect the strength and mechanical properties of the scaffolds (M. Wang & Sultana, 2012). It is necessary for scaffolds to have appropriate mechanical properties to ensure the scaffolds maintain structural integrity and permit surgical handling during implantation. Materials and porosity are both the two key factors for scaffolding material properties. Generally, scaffolds can be fabricated from many types of biomaterials such as: ceramics, polymers (Natural or synthetic) and composite polymers (Pluta, Malina, & Sobczak-kupiec, 2015). Depending on the different types of tissue engineering applications, various mechanical properties are required. Scaffolds made purely from polymeric materials provide lower mechanical properties like mechanical strength, Young's modulus and toughness. This kind of scaffold is suitable for soft tissue engineering applications. Additionally, scaffolds made of composite materials (combination between polymer and ceramic materials) can improve their mechanical properties and these scaffolds are designed for hard tissue (bone) engineering (Li et al., 2017; Silva et al., 2006; M. Wang & Sultana, 2012). Additionally, mechanical properties can be further tuned through its structure porosity after choosing the suitable materials for the required tissue engineering application. Scaffolds with low and non-uniformed porosity have comparably lower

mechanical properties. A more porous structure has better mechanical properties and better gas/liquid diffusion ability to promote cell growth, such as uniformed honeycomb shaped scaffolds contribute to good compressive force and it's ideal for tissue engineering scaffolds (Wang et al., 2009). Therefore, it is essential to characterize the ideal porosity for different tissue engineering applications.

In order to manufacture suitable scaffolds for various types of tissues, there are numerous studies into the morphological scaffolds design including the pore shape and size, interconnectivity and spatial distribution of the scaffolds. Microbubbles as pore generators have been recently applied in the biomedical field. It is depicted by Stride et al. (Ahmad, Stride, & Edirisinghe, 2012) that a sponge-like, multiple-layered alginate scaffold have been made by piling alginate microbubbles on glass slides over a certain period of time, with identical size of pores of 250 μm which stimulated cell migration and distribution within scaffolds.

2.1.2.5.1 Conventional fabrication of scaffolds

A wide range of well-known manufacturing techniques are applied in scaffold fabrication for various tissue engineering applications. Some of the main manufacturing techniques are described below (figures shown in Figure 2-7 a), b) and c)). There is particulate leaching (Prasad, Sankar, & Katiyar, 2017), emulsion freeze drying (M. Wang & Sultana, 2012), foaming (Q. Z. Chen, 2011), electrospraying (Jayasinghe & Sullivan, 2006), electrospinning (X. Zhang, Reagan, & Kaplan, 2009) and phase separation (Liu & Ma, 2009). Scaffolds fabricated by the beforementioned techniques have coarse pore size and shape distribution with a high polydispersity index (PDI) which results in the inadequate transportation of nutrition, oxygen,

adhesion and migration of cells. Furthermore, the majority of the scaffolds' biocompatibility is hindered due to the use of organic solvents and particulate leaching, which further reduced the viability of cells among the beforementioned manufacturing methods (Bružauskaitė, Bironaitė, Bagdonas, & Bernotienė, 2016).

2.1.2.5.1.1 Particle leaching

Particle leaching technique (Figure 2-7 a)) encompasses various particles acting as the porogen in scaffolds, like salt, ice, sugar or other specifically premade spherical particles which were dissolved in the polymer sample and washed away later. This technique is widely used to produce scaffolds for tissue engineering, due to its operation simplicity (Peter X Ma & Langer, 1999; Pliable, Tissues, & Engineer, 1996). The pore size can be tuned by management of the size, shape and amount of the added porogen. The scaffolds fabricated with this technique can achieve porosity of above 90%, pore size around 500 μm and preferable crystallinity (Subia, Kundu, & Kundu, 2010). One of the merits of this technique is the generation of large pore sizes and the good control of the structural morphology of the produced scaffolds. Nevertheless, this technique is not suitable for water-soluble materials such as gelatine and bovine serum albumin scaffolds as the material residue after processing is likely to be toxic and further harm the tissue formation. Another main drawback is that this method can only manufacture scaffolds up to 3mm thickness and it is hard to achieve desirable pore interconnectivity (Subia et al., 2010).

2.1.2.5.1.2 Emulsion freeze drying

In the emulsion freeze drying method, the emulsion is made by introducing a water phase into a thoroughly mixed polymeric solution (oil) phase and then homogenized

by a homogenizer at various speeds to achieve a well-blended emulsion. This emulsion is rapid solidified by transferring to a freezer of a pre-set temperature of 35^{o}C. Then a freeze-drying vessel of pre-set temperature of -10^{o}C is run for at least 46 hours to remove the remaining solvent and the water phase from the pre-made frozen emulsion and the following porous polymeric scaffolds was made (Figure 2-7 b)). Subsequently, the scaffolds is placed in a vacuum desiccator at room temperature to completely remove any leftover solvent (M. Wang & Sultana, 2012; F. Zhang et al., 2011). The highlight of this method is that neither high temperature nor separate leaching procedures are involved to manufacture controllable pore sizes by the freezing rate. The demerits of this technique are the long fabrication time to achieve small pore size in scaffolds and the low pore permeabilities which restricts the cell growth and further the exchange of nutrients within the scaffolds.

2.1.2.5.1.3 Gas foaming

Gas foaming, namely high-pressure foaming, is conducted by introducing an inert gas, like carbon dioxide, to a dry polymer at high pressure to eventually form a single-phase polymer-gas solution. The following pressure is dropped to prompt the thermodynamic instability of the dissolved carbon dioxide gas, which leads to gas nucleation and growth to produce porosity within the polymer matrix (H. J. Chung & Park, 2007). The key advantage of this technique is to abandon the use of organic solvents and subsequently to reduce the toxicity of remaining residual solvents on cell growth and the following tissue formation (Subia et al., 2010). This technique is also helpful to incorporate heat sensitive biomolecules into scaffolds, due to no heating process involving during fabrication. The drawback of this technique is the

insufficiency in pore interconnectivity within the polymeric matrix and non-porous surface in most cases (H. J. Chung & Park, 2007).

2.1.2.5.2 Scaffolds made by microfluidics devices

Scaffolds fabricated by the beforementioned techniques have coarse pore size and shapes, therefore it is hard to conduct systematic investigations on the architectural effects on the differences in signalling, gene expression and organization (K. Y. Chung, Mishra, Wang, Lin, & Lin, 2009). To eliminate the interactional influence of cell-to-cell and cell-to-matrix due to the difference in structure, it is necessary to have well-ordered and uniformed spatial architectures of scaffolds. Furthermore, functional scaffolds are often fabricated with the addition of bioactive molecules, such as growth factors, drugs or adhesion peptides. A highly uniformed spatial architecture is beneficial to homogeneously diffuse the chemical stimuli (H. J. Chung & Park, 2007; Rowley, Madlambayan, & Mooney, 1999).

Scaffolds have been produced in a solid foam, which is created by rapid solidification of liquid foam. Liquid foam is formed by dispersion of gas bubbles in a liquid solution where they are thermodynamically metastable. Crystalline phases were subsequently self-assembled by monodispersed bubbles, which results in better mechanical strength and longer stability than polydisperse bubbles. Conventionally, monodispersed liquid foams containing 1-10 mm diameter bubbles are made by introducing a gas phase into a liquid column. Gravitational force dries the liquid rapidly in this length scale. Microfluidics is the technique to control fluidic flow on microscales, which offers a new method to manufacture monodispersed bubbles or droplets in the length scale of a few hundred micrometres. A range of sizes of

bubbles/droplets could be tuned by solution material properties, flow rate ratio and microfluidic channel designs (Khademhosseini & Langer, 2007). Eventually, pores of scaffolds are formed when bubbles are naturally drained (Figure 2-7 d)). Various microfluidics configurations have been adopted to introducing gas and liquid phases, such as flow focusing (Garstecki, Fuerstman, & Whitesides, 2005), cross flowing (Garstecki, Fuerstman, Stone, & Whitesides, 2006a), and coflowing (Anna, 2007). Many vigorous studies are conducted to investigate the dynamics, mechanism and scaling behaviours of bubbles (Garstecki & Whitesides, 2006).

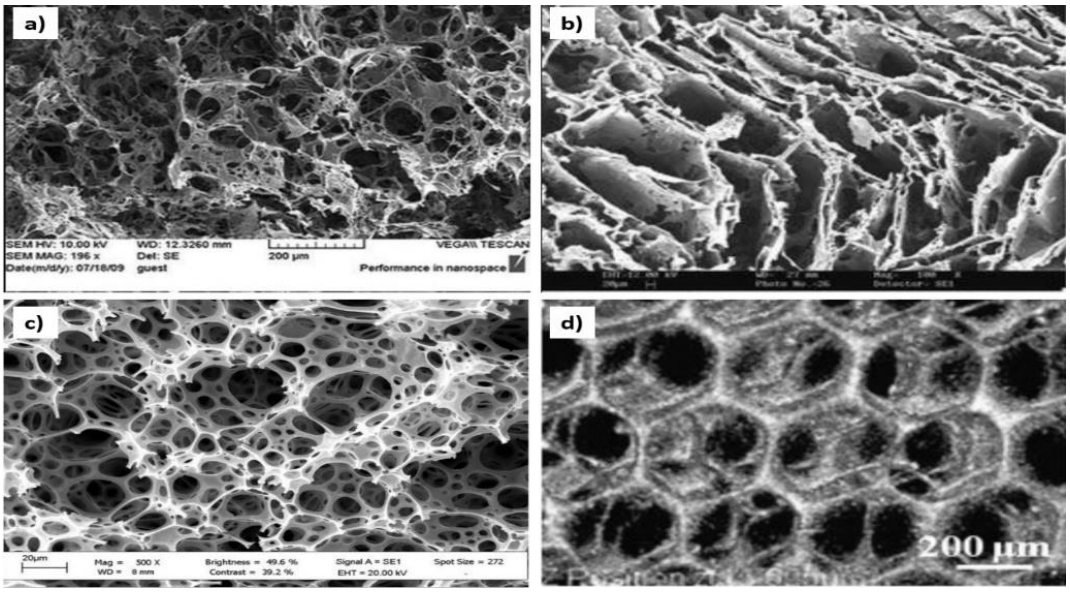

Figure 2-7: SEM images of porous scaffolds produced with various techniques of a) particulate leaching (Prasad et al., 2017)**, b) emulsion freeze drying** (M. Wang & Sultana, 2012)**, c) gas foaming** (Andrieux, Drenckhan, & Stubenrauch, 2018) **and d) microfluidics** (K. Y. Chung et al., 2009)**.**

2.1.2.6 Polymeric scaffolds

To manufacture scaffolds for tissue engineering applications, the use of biocompatible polymeric materials which are less likely to trigger an immunological or foreign body reaction are necessary. The chosen materials should be degradable, and its degradation rate should coincide with the rate of tissue regeneration. There

are numerous kinds of polymers used as tissue engineering materials which can be grouped as natural derived materials (collagen and fibrin) and synthetic polymers (PLA and PGA), and their copolymers (PLGA) (P X Ma & Choi, 2001). The merit of naturally derived polymers is that they can promote cell adhesion and function, however they may also be composed of pathogenic impurities and possess unwanted immunogenicity. Another demerit of natural materials are their poor scaffold mechanical properties and biodegradability along with batch to batch variability due to natural variations. Conversely, synthetic materials have the potential of mass production with desirable properties of mechanical strength, degradation rate and architectural structure. Since there is no polymeric material alone that can fit all criteria for scaffold design, composite materials are commonly used to fabricate scaffolds with an excellent combination between mechanical properties and cell adhesion to mimic the natural bone or tissue matrix.

To fabricate desirable scaffolds with a suitable decomposition rate, ideal biocompatibility, surface characteristics and good plasticity, materials, which vary from natural polymers like hyaluronic acid, alginate and chitosan to synthetic materials for example PGA and PLGA, have been intensively studies. However, most synthetic polymeric materials are hydrophobic which is unfavourable for cell adhesion and growth. In order to solve this problem, many techniques have been proposed such as introducing hydrophilic coatings on synthetic scaffolds or immersing it in growth factors by adsorption or cross-linking. As a result, these post-treatments promote the cell adhesion and growth on synthetic polymeric scaffolds.

On the other hand, they may change the scaffolds' morphology and physical properties.

2.1.2.7 Nanoparticles for targeted drug delivery

The evolution of nanoparticle delivery methods for targeted drug delivery has been recently explored (Moghimi, Hunter, & Murray, 2001). Targeted drug delivery systems can be categorized into two types: active and passive. Active targeting needs to conjugate the therapeutic agents directly onto a tissue or a cell-specific ligand (Lamprecht et al., 2001). Passive targeting is accomplished by loading the therapeutic agent into a nanoparticle which subsequently approaches the target sites. Drug-laden nanoparticles can passively target tumour sites via the enhanced permeability and retention effect (EPR effect), which indicates certain sizes of nanoparticles tend to accumulate in tumour tissue much more that they do in healthy tissue (Greish, 2010). There are several nano-sized drug delivery vehicles including nanocapsules, nanospheres and nanoparticles. Nanocapsules are a matrix system where drug is loaded in a cavity encapsulated by a polymeric membrane (Swarbrick & Boylan, 2003). Nanoparticles are one type of nanosphere, which are solid colloidal particles containing macromolecular substances which vary in size, from 10 nm to 1000 nm (Swarbrick & Boylan, 2003), where the macromolecular substance (i.e. drug) are physically and evenly dispersed. The drug of interest in most cases is dissolved, entrapped, adsorbed, encapsulated into or onto nanoparticles. The advantages of nanoparticles in targeted drug delivery are due to two key factors: small size and the employment of biodegradation materials. The small size of nanoparticles enables them to escape from blood vessels to sites of inflammation and also to deliver drugs

though biological barriers such as the blood brain barrier (BBB). Moreover, the nanoscale size of particles enhances the uptake efficiency by numerous cell types and promotes the agglomeration of the selected drug on the targeted sites (Manisha P., Vinod, Elka, Roberts J., & Gordon L., 1997; Panyam & Labhasetwar, 2003). Nanoparticle are ideal for intravenous delivery due to their smaller size. The smallest capillaries in human beings are around 5 – 6 µm in diameter, which require the particle size to be distinctly smaller than 5 µm to avoid embolism in the blood stream.

The usage of biodegradable materials for nanoparticles enables consistent drug release on the targeted site over a desired time span of days or even weeks. Nanoparticles made of biodegradable natural or synthetic polymers have drawn a lot research attention, owing to their good stability and simplicity of surface modification (Herrero-Vanrell et al., 2005). The choice of nanoparticle materials relies on several factors such as the antigenicity of the final products, biocompatibility and toxicity, level of biodegradability, suitable drug release profile, inherent drug properties and desired nanoparticle size and surface characteristics (Kreuter, 1994). Subsequently, nanoparticles can be adjusted to have both sustainable drug release and disease-specific localization by use of suitable polymers and surface treatments (Moghimi et al., 2001; Panyam & Labhasetwar, 2003). Once nanoparticles have accumulated on the specific targeted sites, hydrophobic biodegradable nanoparticles can act as drug reservoirs to release the encapsulated therapeutic compounds at defect sites such as tumours. As a result, nanoparticles generally can be employed to enable targeted drug delivery, enhance bioactivity, control drug release and protect active therapeutic agents against enzymatic degradation (Ge et al., 2002).

Nanocapsules, nanosphere and nanoparticles can be fabricated to have distinct properties and release profiles for desirable drug delivery or the addition of various therapeutic agents, through different manufacturing methods (Barratt, 2000; Pitt, Gratzl, Kimmel, Surles, & Sohindler, 1981). Different preparation methods of nanoparticles have been discussed below.

2.1.2.7.1 Traditional methods for the formation of polymer particles

There are numerous technologies to generate nano- or micro-scaled particles such as the dispersion polymerization, single-solvent evaporation, double emulsion, spray drying, electrohydrodynamic atomization and microfluidics. All technologies have their own strengths and weaknesses. In general, successful fabrication of polymeric particles requires a good size uniformity, high drug loading efficiency and scale-up potential. Here, we discuss some of the preparation techniques below.

2.1.2.7.1.1 Dispersion polymerization

Dispersion polymerization is a type of precipitation polymerization, which is carried out by adding stabilizer into the reaction medium. The selection of solvent in the reaction medium must be miscible with the monomer and the initiator but immiscible for the polymer (Rudin & Choi, 2013). During the polymerization procedure, the polymer precipitates when the remaining polymer weight in the reaction solution reaches the critical level (Kawaguchi & Ito, 2005). The particle is formed when the initial particle is stable and does not coagulate with other nearby particles. From this point of polymerization forward, the growth of stabilized particles is dependent on the addition of monomers in solution (Kawaguchi & Ito, 2005). Meanwhile, the stabilizers adhere covalently to the particle surface during the growth of polymeric

particles. There stabilizers can form an extra layer around particles to prevent coagulation, which subsequently limit the particle size and stability in the reaction system. Particle sizes of 0.1 – 15 μm in diameter are usually produced with the dispersion polymerization process.

2.1.2.7.1.2 Solvent evaporation method

Solvent evaporation is one of the most well-established and regularly applied techniques for the production of nanoparticles (Desgouilles et al., 2003). This technique is dependent on the emulsification of the polymer solution into an aqueous solution and the following polymer solvent evaporation. The water immiscible polymer and drugs are first dissolved into a suitable organic solvent such as dichloromethane, chloroform or ethyl acetate. The organic polymeric solution is then loaded with drugs and added into the aqueous solution (continuous phase) containing a surfactant to stabilize the water/oil emulsion. A homogenizer is applied to form a homogenous stable solution and to limit the size of the droplets. As soon as the homogenous emulsion is formed, the solvent is evaporated either by vacuum pump or by ultracentrifugation to precipitate nanoparticles. The colloidal suspension is then rinsed by distilled water to remove the surfactant residue or extra drug and subsequently stored after lyophilization (Song et al., 1997). The size range of nanoparticles is controlled by the concentration and type of surfactant, polymer concentration and homogenizer stirring speed (Kwon, Lee, Choi, Jang, & Kim, 2001). High-speed stirring often leads to the production of smaller size nanoparticles and vice versa (Zambaux et al., 1998). Furthermore, porous nanoparticles are produced after solvent evaporation. An illustration of this method is seen in Figure 2-8.

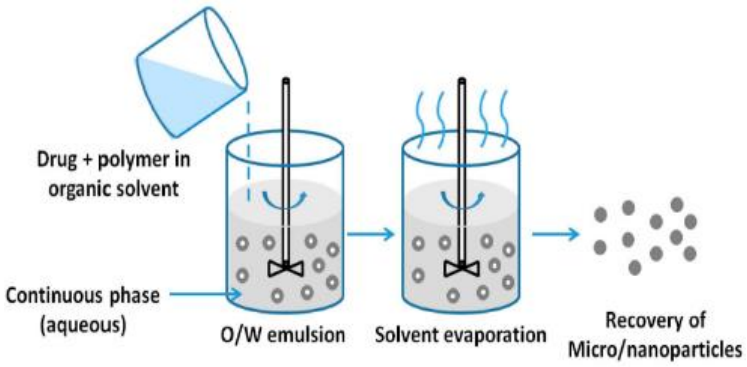

Figure 2-8: preparation of nanoparticles produced by solvent evaporation method (Y. Wang, Li, Truong-Dinh Tran, Zhang, & Kong, 2016)**.**

2.1.2.7.2 Nanoparticles made by microfluidics

The microfluidic method to produce nanoparticles for drug delivery has numerous advantages. When comparing the beforementioned techniques, this technique is able to incorporate the shear sensitive biomolecular drugs and sustain their bioactivity. There is also an advantage for the use of costly drugs with the microfluidic method compared to traditional methods owing to the small quantities required in microfluidics. Another reason is due to the waste caused by filtration of aggregation loaded with drugs in conventional methods. Another advantage of microfluidics is based on its ability to produce homogenous particles with narrow side distribution which also contributes to the sustainable drug release and enhancement (Karnik et al., 2008).

2.2 Stability of microbubbles

2.2.1 Theory of microbubble stability

Coated microbubbles have been used in an extensive variety of applications, from food engineering to ultrasound contrast agents in medical diagnostic imaging (M. A. Borden & Longo, 2002; Unger et al., 2004). Coating materials such as phospholipid,

surfactant, denatured human serum albumin or synthetic polymers are used to stabilize microbubbles (Unger et al., 2004). Furthermore, generally, the stability of coated microbubbles are superior to non-coated microbubbles (E Stride & Edirisinghe, 2008). In the majority of these usages, long-time or controlled stability of microbubbles is an important factor especially for medical applications (Lee, Lee, Lee, & Park, 2015) . However, microbubbles are naturally unstable in liquids due to the effect of interfacial tension (σ)(E Stride, 2008). Interfacial tension is the force which combine the surface of two phases together. Surface tension produces a higher interior pressure, compared with the outer pressure of microbubbles, which drives gas to dissolve to surroundings spontaneously (Katiyar & Sarkar, 2010). Moreover, this phenomenon can be described in terms of Laplace pressure which acts on the surface of microbubbles. (E Stride, 2008).

Equation 1

$$P_{Laplace}=\frac{2\sigma}{R}$$

Where σ is the interfacial tension and R is the curvature radius. Microbubble stability has also been affected by factors such as surface density, surface tension and bubble radii of curvature (Gerber, Pierre Krafft, Waton, & Vandamme, 2006).

In order to stabilize microbubbles, surfactant, lipid, or protein molecules are applied as molecular stabilizers or coating which densely assemble at the interface of gas and liquid (Lee et al., 2015). When the gas-liquid interface is totally saturated by molecular stabilizers, interfacial tension decreases remarkably. This process restrains the Laplace pressure at the gas-liquid interface, which furthermore enhances the

stability of microbubbles. The existence of the stabilizer both decreases the interfacial tension in the bubble surface and halts gas diffusion, therefore resisting rapid dissolution, coalescence and disproportionation process within the suspension (Mohamedi et al., 2012).

For gas-filled microbubbles suspended in a liquid environment at a fixed pressure and temperature, dissolution rate relies on the magnitude of the interfacial tension, bubble size, and the concentration and diffusivity of filled gas (Mohamedi et al., 2012). For example, air bubbles dissolve rapidly in blood vessels owing to the Laplace pressure action, arterial pressure, and oxygen metabolism for biomedical applications (Gerber et al., 2006). In order to stabilize microbubbles for diagnostic and therapeutic applications, microbubbles are stabilized by a thin film made of albumin, lipid, or polymer which can help microbubbles to pass the pulmonary capillary bed, however, the thin film cannot assist microbubbles to resist arterial pressure gradients (Dijkmans et al., 2004; Gerber et al., 2006). In addition, phospholipids employed as the main component of bubble cell due to the good resistance to gas permeation (Dijkmans et al., 2004). Moreover, there are three main effective mechanisms to stabilize microbubbles. They are adding extra layer coating of microbubbles, reducing gas-liquid surface tension of microbubbles, resisting the gas transport between microbubbles and their surroundings (M. A. Borden & Longo, 2002). Based on this stability requirement, heavy-molecular or inert gas are used as filling gas of microbubbles instead of traditional air to make stable microbubbles (Gerber et al., 2006).Therefore, a heavy-molecular-weight and low diffusivity gas like sulphur hexafluoride or perfluorocarbon has been used as the gas phase to enhance

survival and stability below higher pressure (Dijkmans et al., 2004; Kang & Yeh, 2011). For instances, Optison™, as second generation microbubble, is composed of albumin shell and perfluorocarbon gas as ultrasound contrast agents in diagnostic imaging (Browning et al., 2012).

2.2.2 Albumin coated microbubbles

The polymer chains are cross-linked or entangled together through covalent bond to form coated encapsulated microbubbles (J. L. Chen et al., 2014). The proteins are also covalently cross-linked to from a protective shell shown in Figure 2-9 (Sirsi and Borden, 2009). In addition, phospholipids have also been used as shell components due to its resistance to gas dissolution (M. A. Borden & Longo, 2002). The stability of microbubbles are effectively increased, when phospholipids are in condensed state and have greater molecular chain length (Unger et al., 2004). Therefore, phospholipids are utilized as the main bubble shell components (M. A. Borden & Longo, 2002; Unger et al., 2004). However, studies have shown that the albumin shelled agents Optison (GE Healthcare Ltd., Pittsburgh, PA, USA) have better performance than phospholipid shelled agents in biomedical applications such as ultrasound contrast agents and therapeutic targeted drug deliveries (Mulvana, Browning, Tang, Hajnal, & Eckersley, 2012; Wang et al, 2005; Alter et al, 2009). Albumin coated microbubbles have already built the way for several succeeding formulations which can go through the lung capillaries and enhance imaging contrast in the left heart ventricle (Alter, Sennoga, Lopes, Eckersley, & Wells, 2009). However, the mechanisms for this improvement have not been clearly explained or optimized due to the difference in microbubble formation and resultant properties (Browning

et al., 2012; Mulvana et al., 2012). Moreover, albumin-coated microbubbles also have great transfection efficiency in ultrasound targeted treatment (Browning et al., 2012). In addition, by altering microbubble composition, the material properties are also changed and thus, enhance its acoustic ability and transfection efficiency. For example, the stability of albumin-coated microbubbles is increased by adding different concentration of dextrose, compared with the stability of pure albumin-coated microbubbles (Browning et al. 2012).

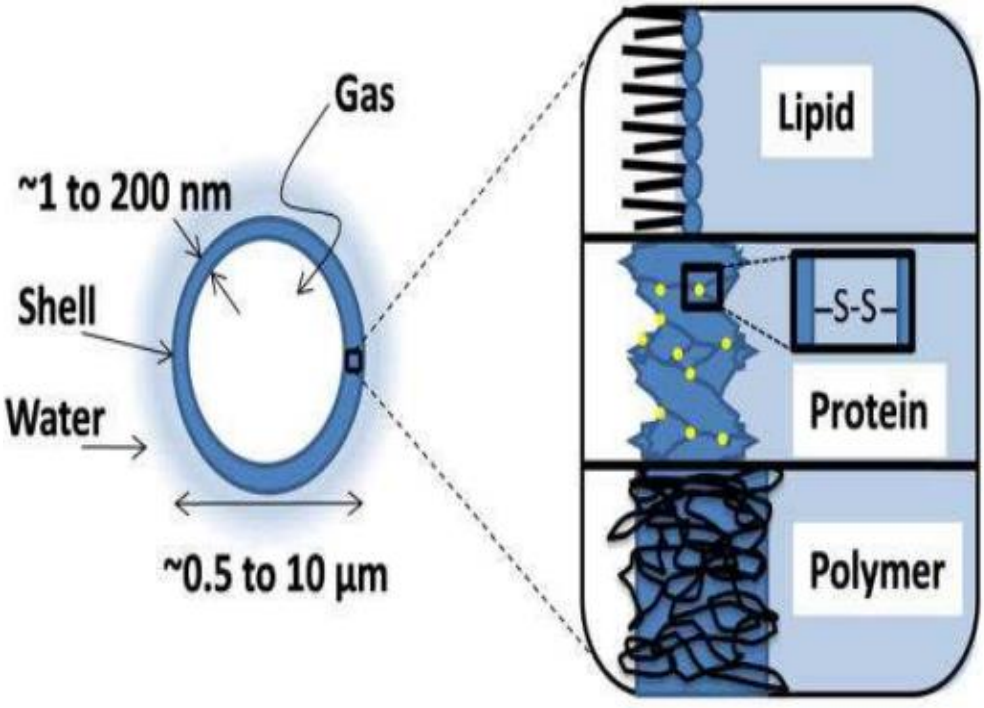

Figure 2-9: The stability of microbubbles has been achieved by three commonly used coating material: lipid, protein, and polymer (Maske et al., 2012)**.**

2.3 Current preparation methods

In the past several decades, plenty of methodologies have been utilized to produce microbubbles, including sonication, coaxial electrohydrodynamic atomization

(CEHDA) and microfluidic processing. These developed bubble formation techniques have been described in this section (Lee et al., 2015).

2.3.1 Sonication

One of most extensively used techniques for formation of microbubbles is sonication which includes introducing gas by using high intensity ultrasound in an aqueous liquid phase, composing of either surfactant or polymer solution to form a stable coating on the surfaces of microbubbles (E Stride & Edirisinghe, 2008). The sonication process is normally achieved with the help of either a sonicator or high-shear mixer which later introduced into a vial containing surfactant solution to produce a gas-liquid emulsion (Figure. 2-10)(Q. Xu et al., 2008a; Y.-Z. Zhao, Liang, Mei, & Halliwell, 2005). A suspension of microbubbles is generated by the emulsification process and the protective coating stabilizers are spontaneously attached on the surface of produced microbubbles. Consequently, the acoustic cavitation caused by gas-filled microbubbles creates high temperature and pressure in the suspension which results in chemical reaction on the microbubble surface and thus, enhancing the microbubble stability (E Stride & Edirisinghe, 2008; Eleanor Stride & Edirisinghe, 2009). However, this technique generates microbubble sizes with a large distribution and microbubbles with diameters larger than 10 µm that have to be filtered out (Hernot & Klibanov, 2008b). Studies have already shown that microbubbles with diameters > 10 µm are rapidly filtered by lungs and can cause the risk of an embolism after blood administration in biomedical applications (Butler & Hills, 1979; J. L. Chen et al., 2014; Hernot & Klibanov, 2008a). Furthermore, wide size distribution also leads to a broad range of resonance frequencies in microbubble ultrasound imaging

(Kooiman et al., 2009). Therefore, further filtration steps are necessary to remove any larger microbubbles and excess surfactant, thus, narrow the size distribution of microbubbles for biomedical applications (Borrelli et al., 2012; Nyborg, 2001; E Stride & Edirisinghe, 2008; Eleanor Stride & Edirisinghe, 2009). Moreover, In sonication preparation method, some key factors such as frequency, power and pulse regime of the ultrasound decide the microbubble size distribution (Kooiman et al., 2009).

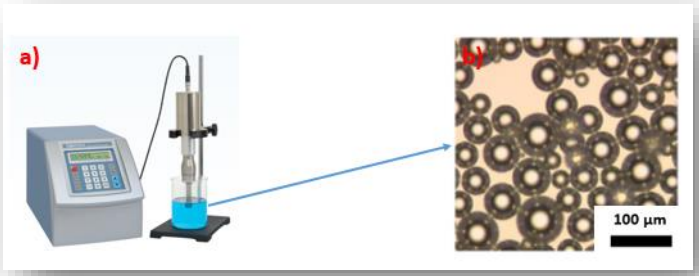

Figure. 2-10: a) A schematic illustration of sonication setup with standard probe. b) Micrograph of polydispersed microbubbles generated by using a) sonication setup (Q. Xu et al., 2008a)**.**

2.3.2 Coaxial Electrohydrodynamic Atomization (CEHDA)

Co-axial electrohydrodynamic atomization (CEHDA) is a modified method based on electrohydrodynamic atomization, which is a one-step method to produce multiple layered microbubbles having size < 10 µm (Lee et al., 2015). In this method, microbubbles can be formed under the influence of external electric field (E Stride & Edirisinghe, 2008). As illustrated in Figure 2-11, two immiscible polymer solutions are introduced into co-axial double layered metal needles via a pair of syringe pumps. The gas is supplied through the inner needle, while the outer needle is pumped with a suspension of the protective coating polymers. A co-axial cone-shaped jet is

generated under the effect of an electrical potential difference between the metal needle and an earthed ring electrode which is located a short distance from the exit of metal needle. Additionally, the diameter of the cone-shaped jet stream can be easily decreased via increasing the supplied electric voltage, and thus, reduction in the diameter of microbubbles. Furthermore, the size distribution of microbubbles depends on the applied gas-liquid flow rate ratio, needle geometry and fluid properties (Farook et al., 2009; Lee et al., 2015; E Stride & Edirisinghe, 2008; Eleanor Stride & Edirisinghe, 2009). Although CEHDA method can generate high output and narrow size distribution microbubbles (< 10 μm) at ambient condition, the monodispersity of microbubbles is still a main issue waiting to be solved (Farook et al., 2009).

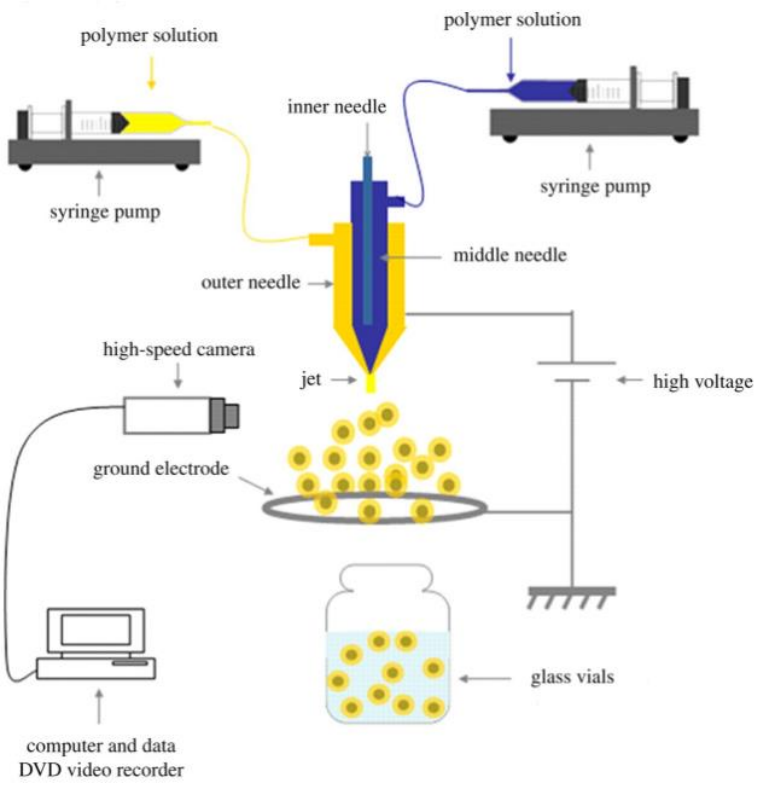

Figure 2-11: A schematic graph of CEHDA setup with coaxially aligned metal needle (Enayati, Ahmad, Stride, & Edirisinghe, 2010).

2.3.3 Microfluidic devices

Microfluidic method generates monodispersed aqueous droplets and gas-filled microbubbles by altering micro-scale fluids. It has been widely investigated and utilized in various industries (E Stride & Edirisinghe, 2008; C.-X. Zhao & Middelberg, 2011). For instance, Microfluidic devices are ideal for biomedical applications because they can generate monodispersed microbubbles in real-time and have the potential to be miniaturized to suit vasculature dimensions (Garstecki. 2004; Wang et al., 2013; Dhanaliwala et al., 2013). Microfluidic devices are also able to generate microbubbles in sufficient quantities to satisfy the requirement of acoustic contrast and drug delivery (Dhanaliwana et al., 2013; Dixon et al., 2013). The usage of microfluidic setups in preparation process of microbubbles has been illustrated to enhance the uniformity and offers the potential for further accurate manipulation over bubble diameter and size distribution. Size distribution and stability are two key points for microbubble formation. The microbubble formation starts at the orifice where the gas column and liquid flow reaches a stable and balanced state and then, microbubbles are generated by a ''pinch-off'' process (Eleanor Stride & Edirisinghe, 2009). The size distribution and monodisperses of microbubbles rely on the liquid physical properties, gas-liquid flow rate ratio and orifice and channels dimensions (Collins, Neild, DeMello, Liu, & Ai, 2015).

In the past decades, there are three main microfluidic geometries which have extensively been investigated and utilized to form microbubbles: co-flowing, flow-focusing and cross-flowing (i.e. T-junction) devices (Garstecki, Fuerstman, Stone, & Whitesides, 2006b; Lee et al., 2015; L. Q. Wang & Zhang, 2009; Q. Xu et al., 2008b).

Due to the microfluidic configuration dominating the microbubble formation, the mechanisms of microbubble formation vary among difference microfluidic devices (Xiong et al., 2007). Moreover, the structure of microfluidic geometries also has a great influence on the control of the liquid and gas flows. These widely used three microfluidic devices: co-flowing, flow-focusing and cross-flowing (T junction), are explained in this section.

2.3.3.1 Fabrication of microfluidic devices

2.3.3.2 Different types of microfluidic devices

2.3.3.2.1 Co flowing devices

The co-flowing microfluidic device is one of the methods employed to generate uniform droplets or gas-filled microbubbles (Collins et al., 2015). In this case, microbubble or liquid droplet formation is highly reliant on fluid velocities, viscosities, surface tension and densities of the used liquids (Collins et al., 2015; Xiong et al., 2007). Meanwhile, the configuration of the microbubble or droplet formation area inside the microfluidic setup is also crucial (Basova & Foret, 2014). The microbubble break-up procesure in co-flowing devices is similar to T-junction devices under the operating conditions (Xiong et al., 2007). Microbubbles and droplets are generated when gas, as dispersed phase for microbubbles, or liquid, for droplets, is separately forced into a small needle centred inside a larger sized needle fed with the continuous phase surrounding the dispersed phase in parallel as demonstrated in Figure. 2-12**.** Due to the continuous phase surrounding the dispersed phase, a bubble begins to grow and then breaks up when the drag and interfacial tension forces are equal at the end of the needle (Basova & Foret, 2014). In addition, the velocity component of

the continuous flow squeezes the bubble surface against the wall of the central needle, which also causes the formation of microbubbles in co flowing devices (Collins et al., 2015).

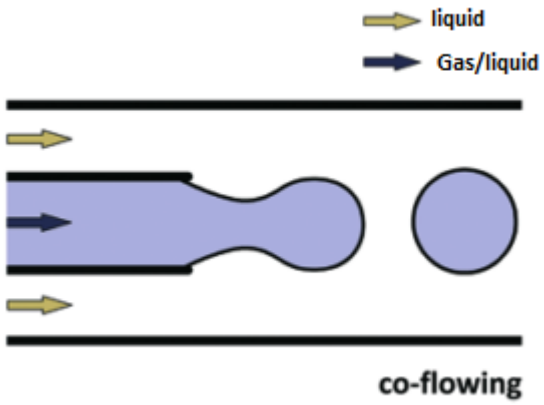

Figure. 2-12: Co flowing geometry, formed droplets or microbubbles. (Collins et al., 2015).

2.3.3.2.2 Flow focusing devices

Flow focusing is another widely used microfluidic technique (Figure. 2-13). This technique has already been extensively utilized for generating spherical monodispersed microbubbles and droplets (Q. Xu et al., 2008b). In the microbubble/droplet formation process, symmetric channels are fed with the continuous phase, surrounding the central channel providing the dispersed phase (liquid phase as dispersed phase for droplets; gas phase as dispersed phase for microbubbles). When the dispersed phase passes through the cross-sectional channel area, the continuous phase compels the dispersed phase flowing through a tiny orifice that is connected with a relatively larger channel feeding with the continuous phase. Consequently, microbubbles/droplets are generated. In the dispersed and continuous phase mixing channel, the continuous phase offers

pressure and shear forces to drive as well as separate microbubbles respectively (Basova & Foret, 2014). Under the flow focusing method, microbubble/droplet diameter, velocity, and frequency all can be altered by the gas-liquid or liquid-liquid flow rate ratio, material viscosities and the orifice dimension (Basova & Foret, 2014; Collins et al., 2015). Due to the central channel always being fed with the dispersed phase, the flow focusing setup compared with cross flowing devices (i.e. T-junction) normally produces spherical bubbles instead of slugs (C.-X. Zhao & Middelberg, 2011).

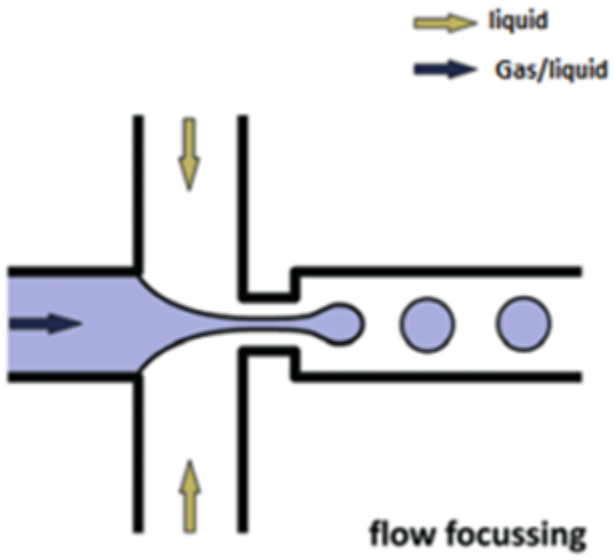

Figure. 2-13: Microfluidic flow focusing device (Collins et al., 2015)**.**

2.3.3.2.3 Cross flowing (T-junction) device

T-junction configuration is the most common and versatile method to produce microbubbles/droplets where the dispersed and continuous phases are fed perpendicularly into the main flow channel (Figure. 2-14)(Basova & Foret, 2014; Garstecki et al., 2006b; J. H. Xu, Li, Wang, & Luo, 2006a). The formation of microbubbles/droplets in T-junction is significantly different from the formation in

the flow-focusing method. The gas or liquid dispersed phase passes into the main fluid channel and a microbubble/droplet begins to grow until it blocks the main fluid channel. Due to the blockage of the channel and the pressure gradient, the fluid squeezes the microbubble/droplet and pinch-off occurs. The size distribution and uniformity of microbubbles/droplets are manipulated by tuning the gas-liquid/liquid-liquid flow rate ratio, material parameters and channel and orifice size (Garstecki et al., 2006b).

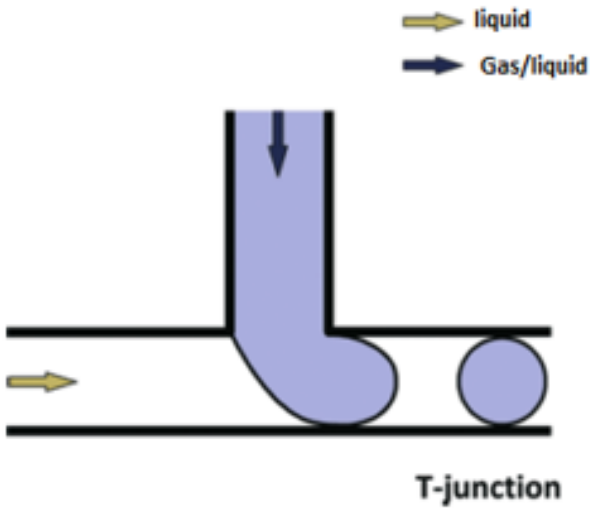

Figure. 2-14: Microfluidic cross flowing (T junction) configuration (Collins et al., 2015)**.**

2.4 Scaling models for microbubble breakup and size prediction in T-junction devices

Owing to the complexity of flow within the T-shaped microchannels, there is no accurate analytical equation for the size prediction of microbubble and droplets. However, several predictive scaling models have been proposed to determine the

size of microbubbles generated in a microfluidic T-junction (Garstecki et al., 2006b). It has been suggested that the mechanism of microbubble/droplet formation depends on the balance of shear stresses, interfacial tension and capillary number (Collins et al., 2015). On the contrary, according to Garstecki et al. (Garstecki et al., 2006b), when the capillary number is small, the mechanism of microbubble formation is controlled by the pressure balance of continuous phase and dispersed phase in the cross-sectional area inside T-junction. When the channel gas pressure is larger than the total Laplace pressure combined with flow resistance (R), the microbubbles start to grow. Laplace pressure is reduced with increasing bubble size. For a T-junction device, under different capillary numbers, there are three regimes on microbubble formation – dripping, jetting, and squeezing (Basova & Foret, 2014). In the squeezing regime for T-junction, the size of microbubbles/droplets is only dominated by the flow ratio of the two immiscible fluids (Garstecki et al., 2006b). The Garstecki scaling law can be seen below:

Equation 2

$$L = d\left(\frac{Qg}{Ql}\right) + w$$

Where L is the diameter of microbubbles, w is the width of channel, $\frac{Qg}{Ql}$ is two immiscible fluid flow rate ratio and D is the characteristic width of the microbubbles.

2.5 Double layered microbubbles

Double layered microbubbles help to reduce the microbubble dissolution and coarsening by splitting the inner gas and the outer fluid, which enables countless potential applications of microbubbles in lightweight materials, aerated foods,

ultrasound contrast agents (R. Chen, Dong, Xu, Wang, & Luo, 2012; Yoon et al., 2015). Moreover, a new possible usage of double layered microbubble is to sustain and even prolong the release of active ingredients in pharmaceuticals (R. Chen et al., 2012; Garti & Bisperink, 1998). Meanwhile, the monodispersity of double layered microbubbles also plays a critical role especially in biomedical applications (Fonslow et al., 2013; Gorce et al., 2000). For example, monodispersed microbubbles as ultrasound contrast agents can increase the ultrasonic imaging quality by enhancing the acoustic response (Fonslow et al., 2013; Gorce et al., 2000). In addition, they can also be used to prepare hollow or porous microspheres or particles, which have great interest in energy-storage materials, catalyst supports and drug delivery carries (Cao, Gao, Kang, & Luo, 2010). Traditional preparation methods have difficulties in sustaining and controlling the integrity and reproducibility of the structure of hollow or porous microspheres and also in producing monodispersed encapsulated microbubbles (R. Chen et al., 2012; J. H. Xu, Li, Wang, & Luo, 2006b). For instance, the traditional template removal process for the formation of hollow particles can damage the coating layer easily (Wan, Bick, Sullivan, & Stone, 2008). Therefore, one promising method for solving this limitation is using microfluidic devices which can precisely control size and shell thickness distribution and also acts as an ideal intermediate to generate hollow or porous microcapsules or particles (R. Chen et al., 2012; Wan et al., 2008). In addition, the stability of microbubbles is also a key factor for applications of microbubbles (Garti & Bisperink, 1998). In order to improve stability, microbubbles are formed with inert gas and coated with additional layers to minimize gas dissolution of microbubbles in liquid (Abbaspourrad et al., 2013). Additionally, microbubbles coated with polymer shells have the greatest stabilization

(Abbaspourrad et al., 2013). Furthermore, based on the distinguished advantages of T-junction such as simplicity, operability, reusability and cost-efficiency (Collins et al., 2015), a double T-junction device has the potential to be used to produce water-in-oil-in-water (L/O/L), oil-in-water-in-oil (O/L/O), gas-in-oil-in-water (G/O/L) double emulsions (Peng et al., 2015).

Chapter 3 Experimental details

3.1 Introductions

This chapter narrates the materials and procedures adopted for the experiments reported in this thesis. The materials used, their suppliers and product details are provided. The characteristic methods utilized to measure the materials and solutions are reported. A comprehensive description of the setup used with single, double and triple T-junction was also stated. All experiments were repeated three times to ensure reproducibility. All devices were calibrated before characterization of materials and solutions.

3.2 Materials

The pivotal material utilized in this thesis to evaluate of bubble formation and size with the aid of single, double and triple T-junctions was bovine serum albumin (BSA). For the experiments carried out to fabricate nanoparticle/scaffolds, nanoparticle formed micropatterns and nanoparticle loaded scaffolds by using single T-junction, PLGA-b-PEG was used. Acetonitrile, dichloromethane, chloroform was chosen as solvents. For the experiments conducted to produce double layered microbubbles with a double T-junction, silicone oil was chosen as the outermost layer encapsulating BSA and nitrogen as middle and innermost layer, respectively. Glycerol was used to validate the bubble fission regime in triple T-junction experiment.

3.2.1 Bovine serum albumin (BSA)

BSA (≥98% lyophilized powder, Sigma Aldrich, U.K), with a relative molar mass of 66,000 g/mol was used to prepare the solution (continuous phase) that enables formation of the shell material of the microbubbles. Glycerol (≥99% for molecular biology, Sigma Aldrich, U. K), with molecular weight 92.09 g/mol mixed with polyoxyethylene 40 stearate (Sigma Aldrich, U. K) was used to prepare the solution to conduct a verification experiment to compare with BSA experiments of single and double T-junction. In order to make double layered microbubbles through a double T-junction device, 50 mPa.s silicone oil was passed through the liquid inlet of second T-junction instead of 15% w/w BSA. Meanwhile, the first T-junction was still fed with 15% w/w BSA to produce silicone oil phase coated BSA double layered microbubbles. Distilled water was used to prepare 15% w/w BSA solution and 50% w/w glycerol mixed with 2% w/w polyoxyethylene 40 stearate solution, separately, by dissolving the above materials with magnetic stirrers in volumetric flasks until a homogeneous solution was formed. Nitrogen was chosen as the dispersed phase (gas) for all the experiments.

3.2.2 Poly (lactic-co-glycolic acid) (PLGA)

Poly (lactic-co-glycolic acid) is a copolymer which contains glycolic and lactic acid. Owing to the different ratios of lactide to glycolide applied for the polymerization, different forms of PLGA can be facilitated: these are normally identified by the molar ratio of the monomers used. Furthermore, the crystallinity of PLGAs can alter from fully amorphous to fully crystalline depending on the molar ratio and block structure. PLGA can also be dissolved in a broad range of solvents depending on the molar ratio.

Chlorinated solvents can be used to dissolve higher lactide content PLGAs. Fluorinated solvents such as HFIP are ideal to dissolve higher glycolide content PLGAs. PLGA is also a FDA approved polymer due to its biocompatibility and biodegradability. In this study, the PLGA copolymer 50:50 Resomer RG503H (Boehringer Ingelheim, Germany) was used with a molecular weight of 33000 kDa which contains of 50% lactic and 50% glycolic acid.

3.2.3 Poly (lactic-co-glycolic acid) – block – poly (ethylene glycol) (PLGA-b-PEG)

PLGA-b-PEG is a block copolymer composed of PLGA and PEG. PLGA-b-PEG has qualities of both its parent monomers. As a result, PLGA-b-PEG is one of the most promising materials for nanoparticle formation and *in vivo* drug delivery applications in the last decades. Regarding nanoparticle formation, PLGA still faces some challenge owing to various factors such as poor stability in aqueous solutions, large diameter (150-200 nm), and the rapid filtration of these big nanoparticles in blood streams by the liver and spleen, which lowers drug concentration dramatically in tumour tissue. Polyethylene glycol (PEG) is the most applied biopolymer for drug delivery use. This is because of its stealth behaviour which prevents the fast recognition by immune system and finally lowers the blood clearance of nanoparticles. Moreover, PEG is hydrophilic and capably of stabilizing nanoparticles by steric effects. As a result, PLGA-b-PEG copolymer has improved material properties with respect to the PLGA and PEG homopolymers, are widely used in the formation of nanoparticles as new drug delivery carries for nanomedical applications.

3.2.4 Glycerol

Glycerol was purchased from Sigma Aldrich, UK with a density of 1261 kg m^{-3}, molecular weight of 92.09 g mol^{-1} and viscosity of 1.4 mPa s, is a simple polyol compound. Glycerol is a colourless, odourless, non-toxic and viscous chemical which is widely used in the food industry and in pharmaceutical formulations. The chemical compound has three hydroxyl groups which are responsible for its solubility in water and its hygroscopic nature.

3.2.5 PEG40S

Polyethylene glycol (40) stearate (PEG40S) is well known to be a biocompatible, biodegradable and nontoxic non-ionic surfactant. It is broadly applied in the food and pharmaceuticals industries as excipients or carrier of various pharmaceutical formulations, food, and cosmetics. PEG40S is also an ideal surfactant to stabilize microbubbles. Moreover, its toxicity and safety have already been well characterized and approved by the FDA. In both short and long-term animal studies, PEG40S showed low acute and chronic toxicities and no reproductive or developmental toxicity. PEG40S was used in this research as a surfactant to stabilize and prolong the lifespan of glycerol microbubbles.

3.2.6 Silicone oil

Silicone oil has great commercial interest. Commonly, silicone oil has been used as heating baths in laboratories and as refrigerants in freeze dryers due to its comparatively high thermal stability and good lubricating properties. Silicone oil has also commercially been applied to control flatulence and treat retinal detachment in

medical uses. Silicone oil was purchased from Sigma Aldrich and used as the outermost layer to facilitate double layered microbubbles in this work.

3.2.7 Acetonitrile

Acetonitrile as a polar solvent is a colourless liquid and has a density of 786 kg m^{-3}, vapor pressure of 9.71 kPa (20^{o}C), molecular weight of 41.05 g mol^{-1} and viscosity of 0.4 mPa s. Acetonitrile is miscible with water and a wide range of organic solvents, which are commonly applied as the mobile phase in high performance liquid chromatography (HPLC), due to its ability to dissolve a broad range of ionic and nonpolar compounds. In this work, Acetonitrile was chosen to dissolve PLGA-b-PEG to produce nanoparticles in the microfluidics systems.

3.2.8 Dichloromethane

Dichloromethane (DCM) is a colourless, volatile liquid and frequently used as an organic solvent. It is polar and slightly miscible with water (17.5 g/L at 25^{o}C). DCM has the chemical formula CH_2Cl_2 with a molecular weight of 84.93 g mol^{-1}, density of 1327 kg m^{-3}, vapour pressure of 57.3 kPa (25^{o}C) and viscosity of 0.43 mPa s (25^{o}C). In this study, DCM was used as a solvent for PLGA-b-PEG to form the PLGA-b-PEG scaffold.

3.2.9 Chloroform

Chloroform is an organic compound and has the chemical formula $CHCl_3$. It is a colourless, dense liquid with a molecular weight of 119.37 g mol^{-1}, density of 1489 kg m^{-3} (25 ^{o}C), vapour pressure of 25.9 kPa and viscosity of 0.563 mPa s (20 ^{o}C). It is

slightly miscible with water (8.09 g/L at 20 ^{o}C). In this work, Chloroform is used as a solvent to dissolve PLGA-b-PEG to form scaffolds.

3.3 Solution Characterisation

3.3.1 Density

The density of the solutions utilized in this thesis was characterized with a 10ml DIN ISO 3507-Gay-Lussac type standard density bottle which purchased from VWR International, Lutterworth, UK. An electronic balance (AND HF-1200G A&D Instruments Ltd., Japan) was used to measure the weight of the empty bottle and the weight of the bottle filled with solution. The density (ρ) was calculated as below:

The weight of the empty density bottle = W_1 g

The weight of the density bottle filled with solution = W_2 g

Therefore, the weight of solution only = ($W_2 – W_1$) g

The density of the measured solution = ($W_2 – W_1$)/10 g cm^{-3}

The average value of three measurements was calculated as the density of solution and stated in this thesis. Measurements were taken at room temperature (22-25 ^{o}C).

3.3.2 Viscosity

The dynamic viscosity of the solutions was measured by a U-tube viscometer (BS/U type, Schott Instruments GmbH, Germany). A calibrated size C U-tube was utilized with nominal constant 0.03. The dynamic viscosity was calculated from the time

recorded (t_s) using the equation of $\mu_s = \frac{\mu_w * \rho_s * t_s}{\rho_w * t_w}$, where μ_w, ρ_s, t_s, ρ_w and t_w were the viscosity of distilled water, the density of the solution, the record time of solution running through the size C U-tube, the density of distilled water and the record time of distilled water passing though the size C U-tube. The measurements were taken at the ambient temperature (22-25 ^oC) and the average value of three measurements was reported.

3.3.3 Surface tension

The surface tension of the solutions was measured by Kruss Tensiometer K9 with standard Wilhelmy's plate method. The Wilhelmy plate is a thin plate commonly made from filter paper, glass or platinum which size is few square centimetres area. The plate is usually utilized to measure the equilibrium surface or interfacial tension at the gas-liquid or liquid-liquid interface. In this method, the plate is fasted to a digital balance and perpendicular to the interface. After it is submerged deep in the solution, the plate is gradually lifted, and the following surface tension is shown on the digital balance. Five measurements have been done for each sample and the plate was cleaned properly with ethanol or distilled water before each measurement to minimize the experimental errors.

3.4 Preparation of solutions

3.4.1 Preparation of BSA solution

Bovine serum albumin (BSA, molecular weight 66000 g mol^{-1}) was acquired from Sigma Aldrich (Poole, UK). Distilled water was used as solvent to prepare 15 %w/w BSA solution. BSA was dissolved by distilled water in a volumetric flask with magnetic

stirrers until a homogenous solution was formed. The weight of BSA was measurement on digital balance and it was calibrated before use. All the experiments were conducted at an ambient temperature of between 22-25^{o}C, ambient pressure of 101.3 kPa, and relative humidity of 55%. All experiments were carried out three times and the average relative value of error is 5 %. BSA was used in this thesis as a model polymer to investigate the effect of physical parameters on microbubbles formation, size and stability with single, double and triple T-junction separately. Table 3-1 below shows the material properties of 15 %w/w BSA used in this thesis.

Solution	Density (kg m^{-3})	Surface tension (mN m^{-1})	Viscosity (mPa s)
15 wt% BSA	1014.7	50.4	16.2

Table 3-1: Material properties of BSA solution used in this thesis.

3.4.2 Preparation of PLGA-b-PEG solution

Poly(lactic-co-glycolic acid)-poly(ethylene glycol) (PLGA-b-PEG) deblock copolymer was used in this thesis as the polymeric material to investigate the feasibility of single T-junction to produce biomaterial scaffolds and nanoparticles.

For scaffolds formation, DCM and chloroform were used as organic solvents to dissolve PLGA-b-PEG separately. The morphology of scaffolds produced with DCM was compared with scaffolds produced with chloroform and analysed in this work. To study the solution concentration on scaffold formation and morphology, 2.5 %w/v, 5 %w/v and 10 %w/v PLGA-b-PEG solution have been made by dissolving into DCM and chloroform. The morphology of scaffolds fabricated with different concentrations were investigated in this thesis.

For nanoparticle formation with resultant micro-stripes, to investigate the polymeric solution concentration on nanoparticle size formation, 2.5 %w/v, 5 %w/v and 10 %w/v PLGA-b-PEG were applied as oil phase in acetonitrile separately within the channel of single T-junction. Distilled water was used in this work to precipitate nanoparticles in a controlled manner though a microfluidic single T-junction device. Material properties of PLGA-b-PEG were shown below in the Table 3-2. Micro-stripes were formed after drying PLGA-b-PEG droplets collected on glass slides. All experiments were done three times.

Solution	Solvent	Concentration (wt%)	Surface tension (mN m^{-1})	Viscosity (mPa s)
PLGA-b-PEG	DCM	10	10.8±0.02	13.2±0.2
PLGA-b-PEG	DCM	5	10.9±0.01	1.3±0.4
PLGA-b-PEG	DCM	2.5	11±0.01	0.8±0.1
PLGA-b-PEG	chloroform	10	10.9±0.03	24±0.5
PLGA-b-PEG	chloroform	5	11.2±0.01	4.9±0.2
PLGA-b-PEG	chloroform	2.5	11.2±0.01	1.2±0.4
PLGA-b-PEG	Acetonitrile	10	13.1±0.01	7.4±0.7
PLGA-b-PEG	Acetonitrile	5	13.3±0.01	1.7±0.1
PLGA-b-PEG	Acetonitrile	2.5	13.2±0.02	0.8±0.3

Table 3-2: Characteristic properties of PLGA-b-PEG solutions used in this thesis

3.4.3 Preparation of glycerol mixed with PEG40S solution

Glycerol with 99% purity was diluted with distilled water at 50 %w/w concentration with material properties shown in Table 3-3 for the study of microbubble fission in triple T-junction. To reduce the surface tension and stabilize the newly formed microbubbles with a triple T-junction device, 2 %w/w PEG40S solution was added. Nitrogen was applied as the dispersed (gas) phase. All measurements have been carried out three times and the mean relative value of the error is 5%.

Solution	Density (kg m^{-3})	Surface tension (mN m^{-1})	Viscosity (mPa s)
50wt%Glycerol mixed with 2wt%PEG40S	1120	46	56

Table 3-3: Characteristic properties of 50wt%Glycerol mixed with 2wt%PEG40S solution used in this thesis

3.5 Characterisation of microbubbles, scaffolds and nanoparticles

3.5.1 Optical microscopy

Optical microscope is a technique dependant on visible light to magnify images of samples with sizes in the micron/submicron range through condensers and optical lenses. The image is usually captured with a light-sensitive digital camera to produce micrographs. In this study, an optical microscope fitted with light-sensitive digital camera (Nikon Eclipse ME 600, Nikon, Japan) with 5x, 10x and 20x magnifications was broadly applied to examine samples of microbubbles, scaffolds and nanoparticles. Due to the limitation of visible light, optical light microscope is commonly used to measure sample sizes > 200nm. These samples were collected on microscope glass slides from the tip of outlet of the microfluidic devices and checked instantly under the beforementioned microscope. For each sample, the size (diameter) of 100 bubbles per scaffold were checked within the given collection area of 1.5 mm^2 to minimize the measurement error. Scale bars were imported automatically using digital software. Later, Image J 1.48v as imaging analytical software was subsequently used to measure the size and shape of microbubbles and scaffolds.

3.5.2 High speed camera imaging

A phantom V5.1 high-speed camera (Vision Research Ltd. Bedford, UK) with a maximum resolution of 1024*1024 pixel at 1200 fps providing a recording time of 6.8

seconds was used in this thesis to record the real time video of the bubble formation process and to measure the bubble productivity and size. Cine viewer software (Vision Research, UK) was used to process all data generated by Phantom V5.1 camera.

3.5.3 Scanning electron microscopy (SEM)

The size, structure and morphology of the microbubbles, scaffolds and nanoparticles were analysed by optical microscope and scanning electron microscopy (Hitachi S-3400N, SEM) in this thesis. SEM is broadly applied to analyse materials' structure by weeping a series of electron beams on the surface of specimen. SEM samples were observed by optical microscope first to ensure the stability of their structure and morphology then they were left to dry for 24 hours prior to gold vacuum coating treatment. Typically, non-conductive samples used in this work were sputter gold-coated within sputtering machine (Edwards sputter coater S 1 50B) for 180s to ensure the surface conduction of samples prior to SEM studies. Then, the specimens were stuck on top of the aluminium stub by a carbon sticker and later put into the SEM chamber. The following electron micrographs were generated through Hitachi S-3400N SEM that was equipped with an electron gun which is used to emit electrons with an accelerating voltage of 5 kV. Analytical software Image J was used to process the images obtained from this SEM and later the average size and polydispersity index of bubbles, scaffolds or nanoparticles were calculated based on the data obtained from Image J.

3.5.4 Fluorescent microscopy

Fluorescent microscopy is the technique based on optical microscopy for observation samples which emit either nature (autofluorescence) or chemical (secondary fluorescence) fluorescent light. Life Evos XL fluorescent microscope (ThermoFisher Scientific, UK) was used to characterize microbubbles, scaffolds and nanoparticles with red channel of 570nm excitation wavelength in this work. Scaffolds and nanoparticles made of PLGA-b-PEG polymer were tagged with Nile red which is an UV-active dyes. Nile red was blended into the PLGA-b-PEG solution prior to nanoparticle formation.

3.5.5 Dynamic light scattering (DLS)

Malvern Instruments Zetasizer was used to measure the nanoparticle size distribution and electrokinetic potential. Disposable folded capillary cuvettes with 50 µl volume was utilized for both measurements. Zeta potential is a scientific jargon for electrokinetic potential which represents the potential difference between the solid particle surface and the surrounding conducting immersion liquid such as water. The zeta potential is s vital indicator of nanoparticle stability. The magnitude of the zeta potential reveals the level of electrostatic repulsion between charged nanoparticles in the suspension. Nanoparticles with high zeta potential either positive or negative are electrically stable, compared to the nanoparticles with low zeta potential which tend to coagulate or flocculate in the suspension. This is due to the nanoparticles are small enough to ensure the high magnitude charge to resist aggregation. In contrast, the attractive force of nanoparticles with low zeta potential may overtake the repulsion force and cause flocculate in suspension.

3.5.6 Small/wide angle x-ray scattering (SAXS/WAXS)

Small angle x-ray scattering (SAXS) was used to measure particle size and polydispersity index of PLGA-b-PEG nanoparticles. Nanoparticle crystallinity was checked by wide angle X-ray scattering (WAXS). SAXS/WAXS were performed using a GANESHA 300 XL SAXS/WAXS system equipped with a High Brilliance Micro focus source providing X-rays with a wavelength of 1.54 Å. Pilatus 300K solid-state photon-counting detector is located inside the vacuum chamber with fully motorization. The change/movement between SAXS ($0.005 \leqslant q \leqslant 0.3$) and WAXS ($2 \leqslant 2\Theta \leqslant 55$) configuration can be achieved within 1 min to allow fast data collection ($q = 4\pi/\lambda (\sin \Theta)$). Samples were contained in a custom designed glass cover transmission holder (Figure. 3-5). Cost-friendly ACADEMY glass cover slips were used as background substrate. Measurements were repeat three times for each samples and the size results have been compared to dynamic light scattering results to minimize the experimental errors.

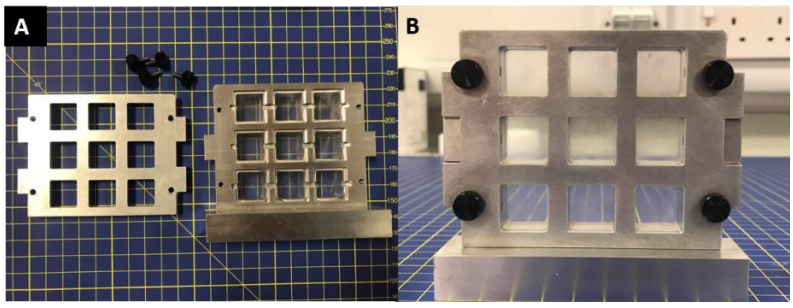

Figure 3-1: SAXS/WASX A) holder parts and B) customized sample holder.

3.5.7 Atomic force microscope (AFM)

In order to investigate the nanoparticle existence on the surface of PLGA-b-PEG scaffolds. Tapping mode atomic force microscope (Digital Instruments, Santa

Barbara, CV) was used to study the surface topography of PLGA-b-PEG scaffolds. A silicon nitride probe was fasted on cantilevers in tapping mode to prevent surface damage. The interaction force was around 10^{-9}N. The AFM images were captured under ambient temperature and pressure with a scan rate of 1 Hz. All measurements were conducted three times for each sample.

3.6 Experimental setup

A schematic of the microfluidics setup is presented in Figure 3-2. This setup consists of a microfluidic device (single, double or triple T-junction), gas cylinder and syringe pump. In all experiments, a pressurized nitrogen gas cylinder was connected to the top capillary of microfluidic device via a blue tubing with 6mm diameter to supple constant gas pressure P_g, which is tuneable via a regulator fitted with nitrogen gas tank. A digital manometer was coupled to the blue tubing to monitor the in-line gas pressure. A 10ml plastic disposable Becton Dickinson syringe (BD Ltd., New Jersey, USA) was connected to the liquid inlet of microfluidic device and placed on top of the Harvard syringe pump PHD-4400 (Harvard Apparatus Ltd., Edenbridge, UK) which provide aqueous phase in a constant flow rate. The number of pumps used in this work are relevant to the number of T-junctions. A high-speed camera was placed against polymeric PDMS microfluidic device to record the bubble/nanoparticle formation.

Microfluidic polymeric block was drawn on AutoCAD software in Figure 3-3. The design was utilized for the following fabrication of microfluidic chip. Although there are a plenty of available materials for use for instance glass, silicone, polymer mould. Polydimethylsiloxane was chosen to fabricate microfluidic devices in this work,

according to its good chemical resistance, high resolution, toughness and low price. The fabrication method affects the type and geometry of microfluidic devices. Precision mechanical machining was used to manufacture due to the low operation cost (in-house fabrication) and small numbers of devices needed. Microfluidic devices are made of several fundamental components to make the device functional and operable. There are channels, connectors, capillaries. The channels embedded into the microfluidic devices had dimension of 1.6 mm as diameter. Microcapillaries were made of Fluorinated Ethylene Polypropylene (FEP) with outer and inner diameter of 1.6 mm and 200 µm. This microfluidic device block is transparent, solid and can stand the high gas pressure up to 700 kPa.

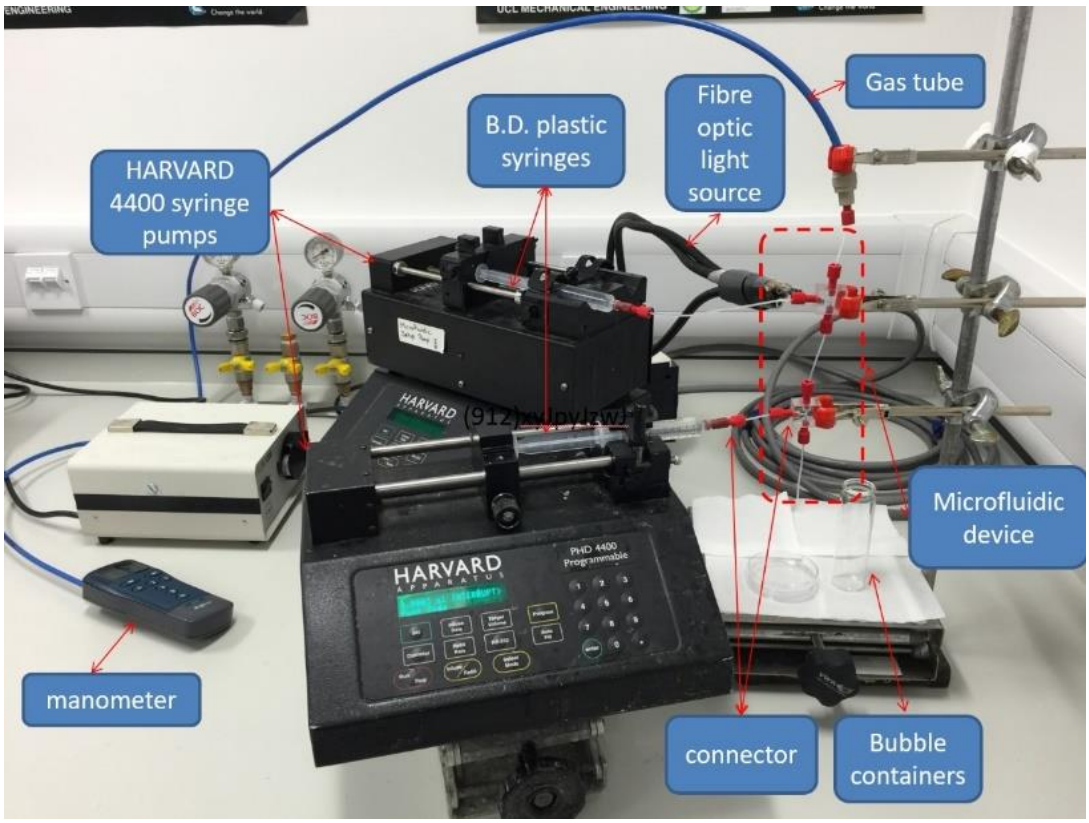

Figure 3-2: Laboratory microfluidic working setup including gas supplier, digital manometer, pumps and microfluidic device. The microfluidic device in this thesis could be the single, double and triple T-junction. Here it shows the microfluidic double T-junction.

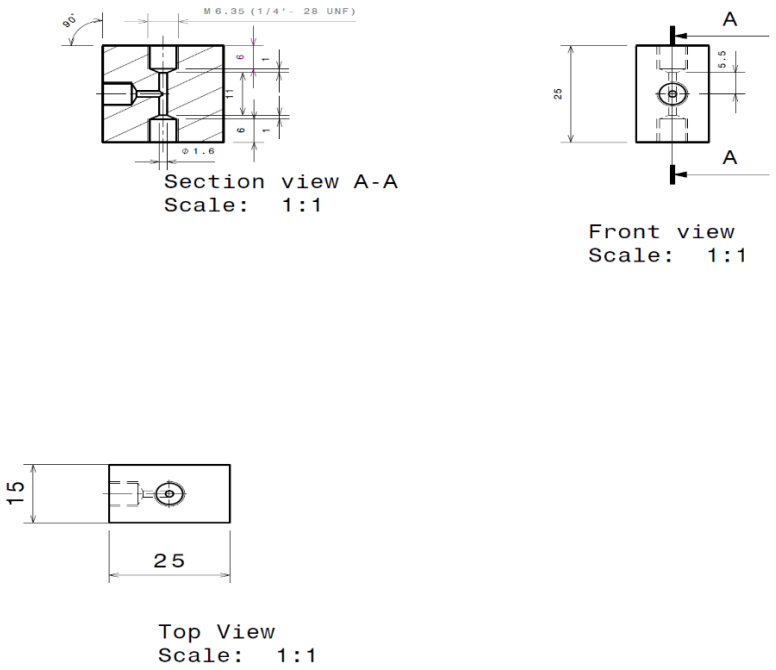

Figure 3-3: CAD drawing of microfluidic T-junction block.

3.6.1 Standard capillary embedded single T-junction

Based on the number of channels, microfluidic devices can be designed as T-type, Y-type and K-type junctions. In this study, T-junction is widely used as fundamental microfluidic device due to its ease of use. An illustration of the single T-junction device is shown in Figure 3-4 (i). This basic device comprises of two Teflon FEP (Upchurch, USA) capillaries with given inner diameter of 200 µm intruded into the beforementioned PDMS polymeric block to create a gap area of 200 µm. A third FEP capillaries was later introduced perpendicularly to these two capillaries. Each capillary was screwed securely to the block by a standard high-performance liquid chromatography connecter to avoid gas or liquid leakage during operation under high pressure or liquid flow rate. The gas inlet is supplied in the main vertical channel and the liquid inlet is in the perpendicular channel. All connections were secured

properly, and all capillaries were pre-washed to prevent leakage and blockage prior to experiments.

In order to study the effect of variation of liquid-gas flow rates on the microbubbles formation, stability and productivity, a given capillary of 200 μm inner diameter and gap size of 200 μm were chosen in this thesis.

3.6.2 Coarse capillaries embedded double T-junction

A schematic of the double T-junction device applied in this thesis is shown in Figure 3-4 (ii). The initial 1st T-junction was made with the beforementioned method in section 3.6.1. A second PDMS polymeric block (2nd T-junction) was connected to the outlet channel of the initial T-junction perpendicular to the second liquid inlet channel with the same inner diameter of 200 μm FEP tubing. The outlet channel was aligned with the exit capillary which is also the inlet for the second T-junction. To investigate the effect of microfluidic geometry on microbubble formation and size, both gap size of 1st and 2nd T-junction between the inlet and outlet were fixed at 200 μm.

3.6.3 Triple T-junction

A schematic graph of the triple T-junction device used in this thesis is illustrated in Figure 3-4 (iii). A third T-junction was inserted at the end of double T-junction which was assembled in the way described in the former section. The liquid inlet is parallel to both the liquid inlets for single and double T-junctions via FEP tubing with inner diameter of 200 μm. Gas supplier was though the main channel of T-junction which is perpendicular to the liquid inlet. The exit channel is aligned with gas inlet with the

ends gap of 200 µm. In this thesis, in order to investigate the effect of variance of gap size of the third T-junction on microbubbles formation and size, the two gaps of the first two T-junctions were fixed at 200 µm and the third gap was set at 150 µm which is small to the inner diameter of liquid inlet capillary, 200 µm which is the size of the inner diameter of liquid inlet and 400 µm which is 2 times larger than the size of inner diameter of liquid inlet.

To investigate the effect of second T-junction on microbubble formation, double T-junction is designed at the same length as the single T-junction. Since in single and double T-junctions microfluidic system, the maximum Reynolds number (Re) is 1.3 when volumetric flow rate Q_l is 200 µl/min. Reynolds number can be calculated by $\frac{\rho * v * D}{\mu}$, where ρ is the density, v is the average velocity, D is the hydraulic diameter of the pipe, µ is the dynamic viscosity (Garstecki et al., 2006a). Reynolds number of 1.3 is far smaller than 2100 which is the critical value for laminar flow transit to turbulent flow (Trinh, 2010). Therefore, the flow profile is laminar flow in single and double T-junction microfluidic channels. In laminar flow, the flow resistance R for a tube with circular cross-section can be calculated by $\frac{128 * \mu * L}{\pi * D^4}$, where L is the length of the tube (Kim, Chesler, & Beebe, 2006). This equation indicates that the flow resistance in a tube under laminar flow is proportionally to the length of the tube L. Therefore, single and double T-junction was designed with the same length (i.e. same flow resistance) to achieve the same flow resistance in the study of addition of second T-junction on the microbubble formation. The reason for the middle connection tubing was 110 mm (Figure 3-4 (ii) double T-junction) is due to the size limitation of T-junction cubic. The length of 110 mm is shortest length which can link two T-junctions together. The

effect of different length combinations of middle and outlet tubing from total length of 200 mm on bubble formation was not the aim of this research.

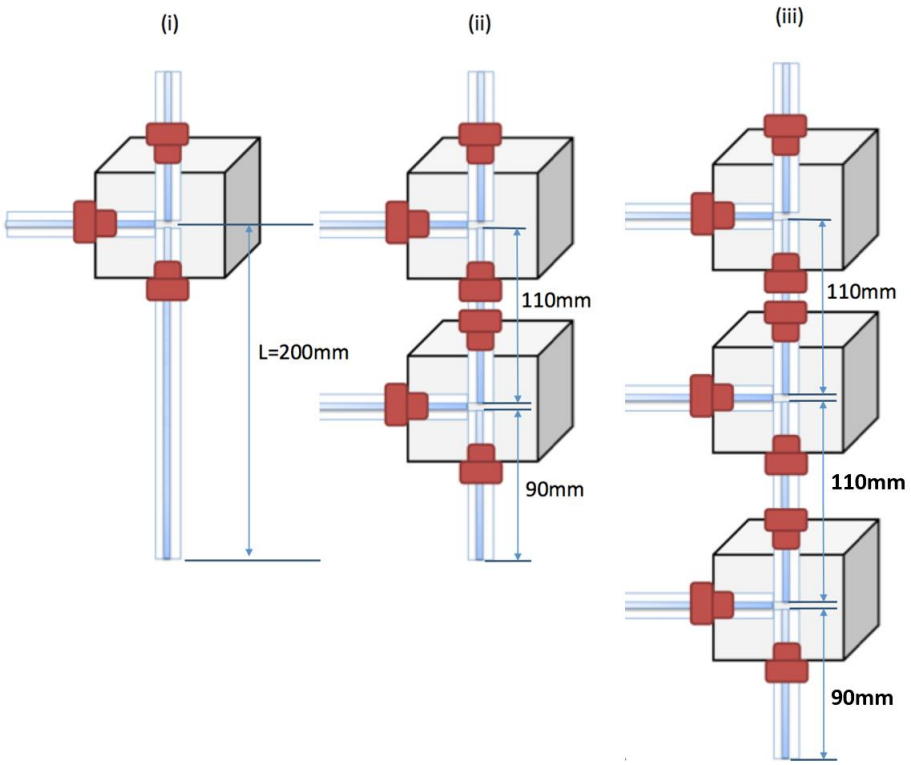

Figure 3-4: Microfluidic devices for this thesis. (i) single T-junction; (ii) double T-junction; (iii) triple T-junction with dimensions.

In Figure 3-4, configuration 1 (single T-junction) and configuration 2 (double T-junction) are kept the same length is to achieve the same capillary hydraulic resistance as one of the controlled variables for the investigation of the effect of the additional second T-junction on microbubbles size and stability in Chapter 4 section 4.2. Microbubbles were collected and measured from the outlet of configuration 1 and 2. Meanwhile configuration 3, triple T-junction, was built based on configuration 2 to study the microbubble fission regime occurred in the third T-junction. Triple T-junction work is an independent work from single and double T-junction works.

3.7 Bubble generation

A schematic of the double T-junction device used in this work is shown in Figure. 3-5. The initial T-junction was created by inserting two Teflon FEP (Fluorinated Ethylene Polypropylene) capillary tubing with inner diameter of 200 μm perpendicularly to each other in to a polydimethylsiloxane (PDMS) block as inlet channels for the gas and liquid flows. A third capillary of 200 μm diameter was inserted into the exit channel of the block and was aligned with the gas supply channel to create a 200μm gap that resulted in a confluence junction of two phases. A second PDMS block was used to insert the exit channel of the first T-junction perpendicular to the second liquid inlet flow with the same diameter (200 μm) FEP capillary tubing. The exit channel was aligned with the exit capillary tube of the initial T-junction that was inserted as one of the inlets of the second T-junction. The gap between the two aligned capillaries were kept constant at 200 μm. The gas was supplied via a tube to one of the first T-junction's inlets. A regulator and a digital manometer were also connected to the tube and used for pressure control and measurement, respectively. The liquid was supplied at a same rate to both T-junction inlets via Harvard syringe pumps (Harvard Apparatus Ltd., Edenbridge UK). The capillaries were fixed and secured to the channels using connectors to avoid leakage of gas and liquid. Microbubbles were collected using glass slides from the outlet capillary of the second T-junction.

For a solution with given viscosity and flow rate, monodisperse microbubble generation only takes place in a certain range of supplied gas pressures with the largest microbubble generated at the highest gas pressure and smallest microbubble

at the lowest gas pressure (M. Parhizkar et al., 2013). At gas pressures below this range, liquid pushes the gas upwards and liquid dripping occurs, while jetting occurs when the gas pressure is increased above this range and microbubbles with a large size distribution are produced. In this work, a range of gas pressures that produced monodisperse microbubbles for each flow rate and geometry were investigated.

For both single and double T-junction geometries, microbubbles were obtained at two flow rates, 100 µl/min and 200 µl/min. For the single T-junction geometry, the microbubbles were collected at every 5 kPa from 15 to 70 kPa and from 15 to 80 kPa at flow rate of 100 and 200 µl/min, respectively. For the double T-junction geometry at flow rates of 100 and 200 µl/min, the microbubbles were collected at every 5 kPa from 20 to 75 kPa and from 35 to 80 kPa, respectively. In order to determine the microbubble stability at different flow rates, gas pressures and geometries, the sizes of microbubbles collected at 20 to 65 kPa at flow rate of 100 µl/min; 35 to 80 kPa at flow rate of 200 µl/min, for both geometries, were monitored every 5 minutes until all the microbubbles disappeared or dried. All experiments were conducted at ambient temperature (21 ° C) and relative humidity of 45%.

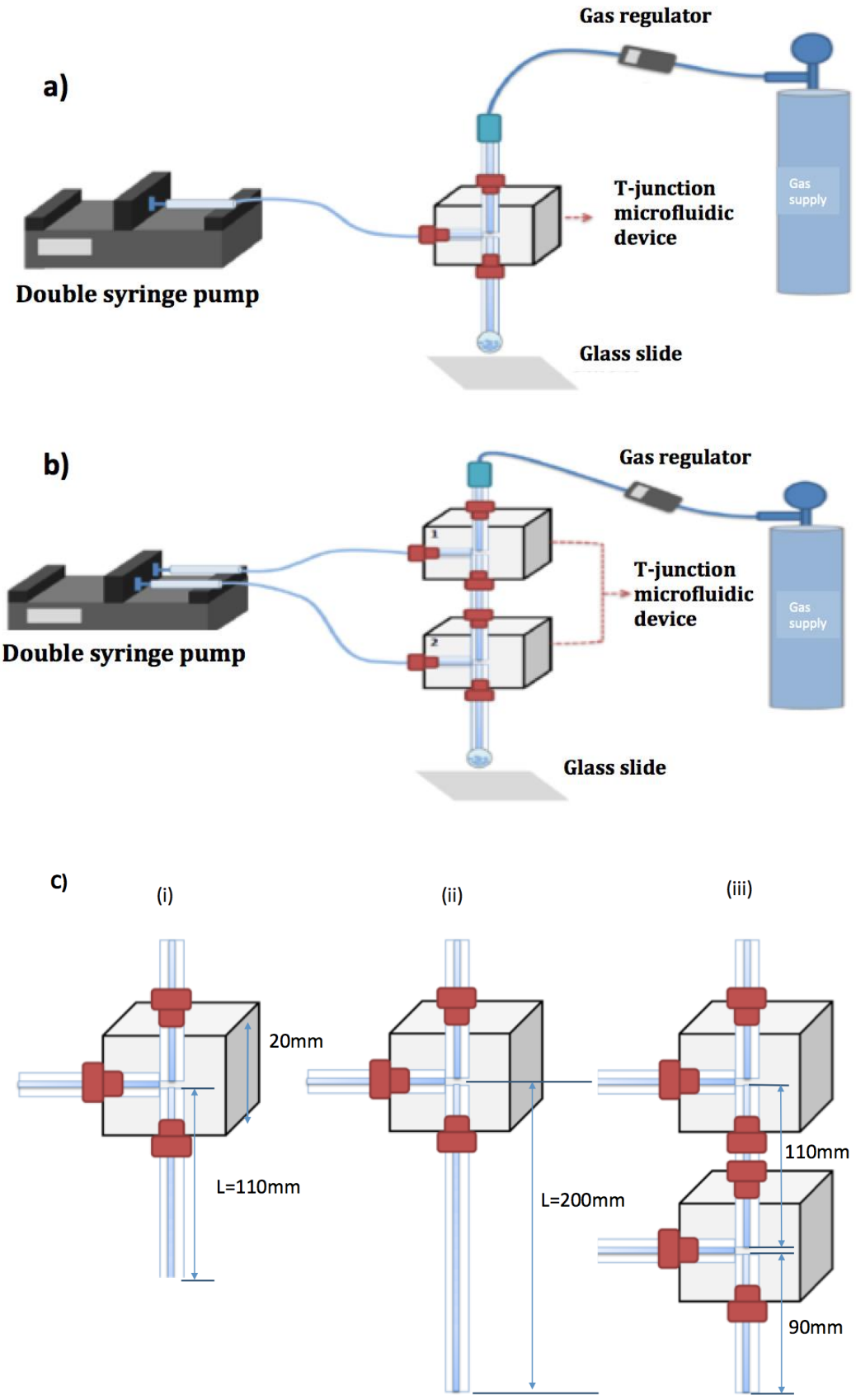

Figure. 3-5: Schematic of the (a) Single and (b) double T-junction cross-flow microfluidic device setup and c) single and double T-junction with different exit channel lengths of 110 and 200mm.

Chapter 4 Results and discussion

4.1 Single T-junction and its bioengineering fabrications: scaffolds and nanoparticles

4.1.1 Overview of single T-junction microfluidic device processing

The operation parameters of single T-junction microfluidic device are well studied by numerous researchers to produce microbubbles (Elsayed et al., 2016; Maryam Parhizkar, 2014). Here, this chapter focuses on the production of potential bioengineering products such as scaffolds and nanoparticles from single T-junction microfluidic device. For scaffold fabrication in section 4.1.2, polymeric material properties were characterized in section 4.1.2.1. The mechanism of microdroplet formation was investigated in section 4.1.2.2. The scaffolds were formed after drying the droplets produced from T-junction microfluidic device. The systematic study of scaffold structure and surface morphology was carried out in section 4.1.2.3. For the nanoparticle fabrication in section 4.1.3, material properties were studied in section 4.1.3.1 and the mechanism of nanoparticle formation in T-junction was explored in the following section 4.1.3.2. The correlation between material properties, and the size and polydispersity of nanoparticles were investigated in 4.1.3.3. The resultant micro-stripe pattern from nanoparticle self-assembling was studied in 4.1.3.4.

4.1.2 Honeycomb-like PLGA-b-PEG structure creation made by microfluidic microdroplets

4.1.2.1 Solution properties of PLGA-b-PEG oil phase

Solution properties, especially surface tension and viscosity, are the major dominant factors in microfluidic systems and known to effect micro droplet forming directly. Table 4-1 summarizes the properties of used solutions during the experimental

procedures. Viscosity of the PLGA-*b*-PEG was found to be increasing with concentration of the solution; however high viscosity at 10% concentration of both solvents did not cause any problem and homogenous micro droplets were generated. Surface tension decreased at elevated concentrations in both solvents. Additionally, surface tension values of PLGA-*b*-PEG were found higher in chloroform when the concentration was kept constant, since the surface tension of chloroform itself is higher than DCM at ambient temperature.

Solution	Polymer	Solvent	Concentration % (w/v)	Surface tension (mN/m)	Viscosity (mPa s)
1	PLGA-*b*-PEG	DCM	10	10,8	13,2
2	PLGA-*b*-PEG	DCM	5	10,9	1,3
3	PLGA-*b*-PEG	DCM	2.5	11	0,8
4	PLGA-*b*-PEG	Chloroform	10	10,9	24
5	PLGA-*b*-PEG	Chloroform	5	11,2	4,9
6	PLGA-*b*-PEG	Chloroform	2.5	11,2	1,2

Table 4-1: Solution properties of PLGA-*b*-PEG in terms of solvent, concentration, surface tension and viscosity.

4.1.2.2 Microdroplets formation with T-junction microfluidic device

In this work, the PLGA-*b*-PEG solution was fed at a constant flow rate provided by the syringe pump for the formation of micro droplets. The micro droplet generation process begins when the dispersed phase reaches the cross-sectional gap area of the T-junction, enters the continuous phase and droplet formation starts. There are three main micro droplet formation regimes: dripping, squeezing and transition (Baroud, Gallaire, & Dangla, 2010; De Menech, Garstecki, Jousse, & Stone, 2008). Capillary number (Ca) is the non-dimensional parameter which dominates micro droplet

formation regimes. Capillary number is the ratio of viscous force and surface tension of the interface between two immiscible liquids.

In the dripping regime, droplet generation happens when the viscous shear stress overcomes the interfacial tension and the micro droplets are produced under high Ca, before their size can obstruct the channel. On the other hand, if Ca is small enough (low Ca), squeezing regimes occurs where the emerging micro droplet will obstruct the channel and therefore the size of emerging droplets are confined by the microchannel dimension (Jian Hong Xu, Li, Tan, & Luo, 2008). This will lead to a dramatic hydrodynamic pressure increase in the upstream side of the micro droplets, which results in the pinch-off of the micro droplets. In between those two regimes is the transition regimes where both forces are important. The diameter of the micro droplet can be manipulated by varying the ratio of liquid flow rate, polymer solution material properties (viscosity, surface tension, concentration), and the channel dimension. For a solution with fixed viscosity and gas pressure, monodisperse micro droplet generation only occurs in a certain range of the provided liquid flow rate.

In this study, micro droplet generation happened passively. Owing to the small Ca value (0.003) in our experiments, the formation process is found to be in the squeezing regimes. Droplet formation in the T-junction is normally consisting of three steps. There are filling period, necking period and pinch-off (Glawdel, Elbuken, & Ren, 2012). In Figure 4-2 and Figure 4-2 (6), firstly the dispersed phase was pushed from the side channel to the main flow in Figure 4-1 a). The droplet grew until it reached the channel wall, which was balanced by the shearing force and droplet interface tension Figure 4-1 b). The droplet obstruction built up the upstream pressure of

droplets, which thins the dispersed phase to form a neck between droplet and dispersed phase and eventually the droplets are detached from dispersed phase Figure 4-1 c). Then micro droplets were generated. By varying the liquid flow rate, viscosity, surface tension and concentration of the two immiscible solutions, different size ranges of monodispersed micro droplets can be generated.

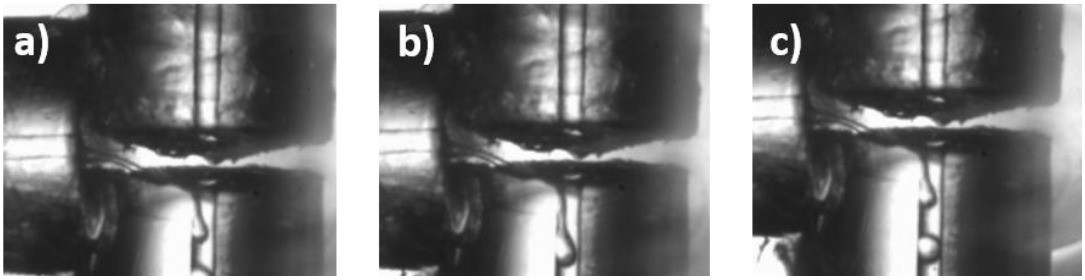

Figure 4-1: droplet formation inside T-junction. a) the filling stage: the droplet grew in microfluidic main channel; b) necking stage: the droplet blocked the main channel and necking formed. c) droplet detached from dispersed phase.

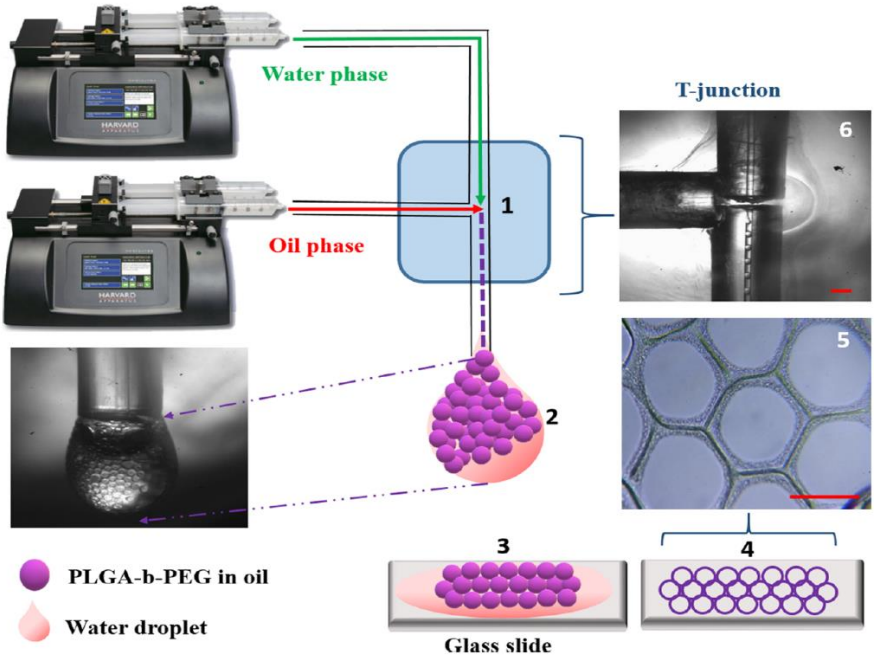

Figure 4-2:Schematic representation of microdroplets fabrication in T-junction microfluidic device setup (1-2) (insert shows the tip end of junction), collected layer on the top of glass slide (3) and the honeycomb-like structure production (4). The optical microscope image of the honeycomb-like structure, scale bar = 100 µm (5). High speed camera of T-junction module, scale bar = 500 µm (6).

4.1.2.3 Honeycomb-like structure made by T-junction device

Microdroplets obtained from the outlet of the T-junction on the microscope glass slides were examined under an optical microscope (Figure 4-2) Monodispersed droplets aligned in an ordered pattern in 2D environment, which later lead to porous honeycomb-like structures post bursting. The formation of porous honeycomb-like structures occurs in the aqueous phase by polymer diffusion (oil phase droplets). After the oil droplets exploded and dried, the PLGA-*b*-PEG amphiphilic polymer was precipitated in the aqueous medium as a honeycomb-like structure according to the circular spread of micro droplets. Figure 4-3 shows the schematic formation mechanism of porous honeycomb-like structures from PLGA-*b*-PEG containing perfectly organized monodispersed micro droplets. Here, volatile oil phase, either chloroform or DCM, starts to evaporate in w/o emulsion in this confined dimension and the interaction of PEG ends with water phase increases at the oil-water interface, subsequently rupture of polymeric sheath occurs. The resulting honeycomb-like membrane structure after drying consists of a PLGA-*b*-PEG pattern with uniform pore sizes. The parameters affecting the pore shape and size will be discussed in sections 4.1.2.3.1. and 4.1.2.3.2 Figure 4-4 shows the representative images of obtained porous honeycomb-like structures after drying. Both porous membranes and scaffold-like 3D structures were produced after drying micro droplets obtained on substrates depending on the collection type. 2D structures were collected as monolayer while 3D ones in multilayers on glass slides. Uniform 3D structure consisting micro-droplets are formed by up to 2-3 layers on glass slides, due to slip from top of one another. However, if the droplets are collected in confined volumes it is possible to collect multilayer scaffold like structures. In this work, I focused on

the production and characterization of the structures. In Figure 4-4, representative multi-layered examples were shown to point out the possibility of obtaining such structures and it is possible to obtain in both DCM and chloroform.

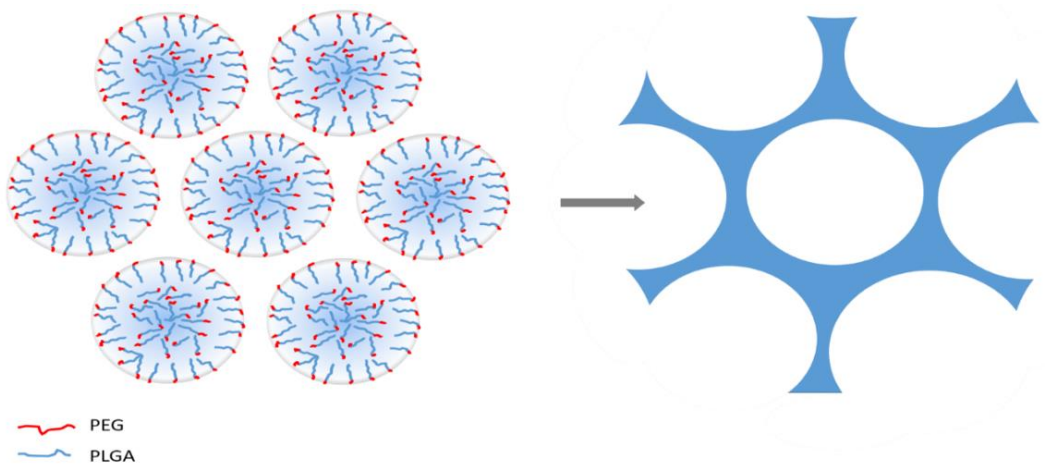

Figure 4-3: Schematic representation of PLGA-*b*-PEG micro droplets with the chain orientation of hydrophobic and hydrophilic counterparts (left) and honeycomb-like structures which occur after bursting and drying steps (right).

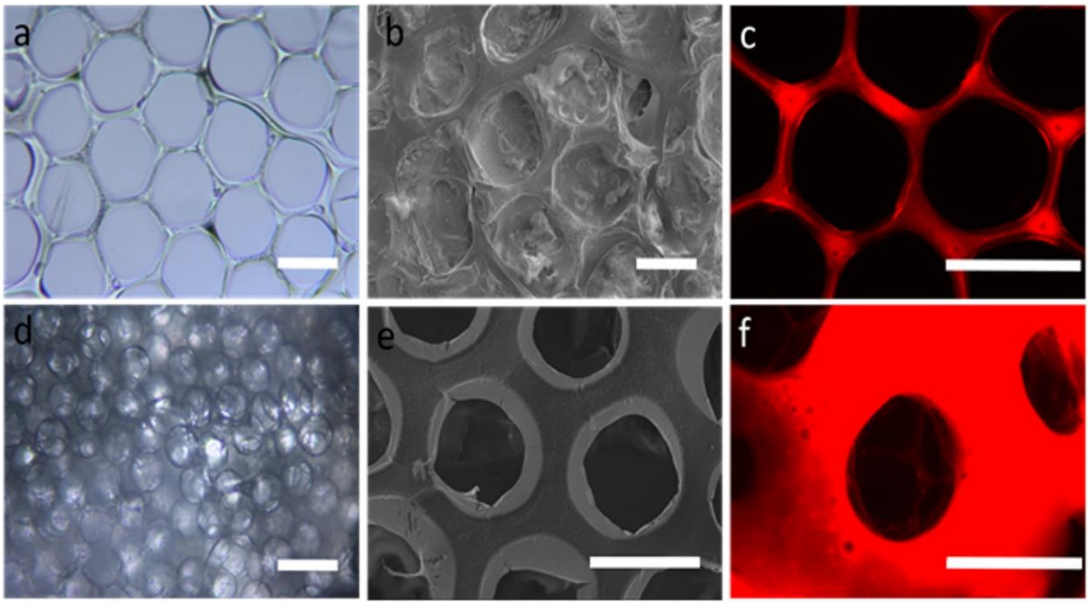

Figure 4-4: 2D (a-c) and 3D (d-f) honeycomb-like structures produced. Micrographs were taken with optical (a,d), scanning electron (b,e) and fluorescent microscope (stained with Nile Red) (c,f). The concentration of PLGA-*b*-PEG is 5%w/w in DCM and the water/oil flow rate was 1 in all samples. Scale bars indicate 100 µm (a,b,d,e) 200 µm (c) and 400 µm (f).

4.1.2.3.1 Effect of flow rate ratio on microdroplets/structure pore sizes

In a typical liquid-liquid fluidics process in T-junction geometries, two immiscible fluids form an interface and the penetration of discontinuous phase into the main channel generates the "droplet"(Nisisako, Torii, & Higuchi, 2002). As the droplet grows in the neck, the pressure applied by the continuous flow pushes the penetrated liquid extension downstream and the droplet breaks. The process repeats itself after the tip of the discontinuous phase retracts to the junction and penetrates again (Garstecki et al., 2006a). The volume of the droplet can be adjusted by the flow rates of both carrier and dispersion phases. Here, water phase (dispersion) / oil phase (carrier) (w/o) flow rate was chosen as the first parameter for the evaluation of porous structures. Then, PLGA-*b*-PEG concentration was kept constant at 10 % w/w during this investigation. Both DCM and chloroform were tested as organic phase during the investigation.

At a constant flow rate of 100 µL/min for the oil phase, water phase flow was increased from 50 µL/min to 300 µL/min by increments of 50 µL/min. The average droplet size was found to be increasing as the water/oil flow rate increased. The increase was observed in both solvents; however droplet formation could not be observed when the water/oil flow rate above 2 for chloroform. At water/oil flow rates of 2.5 and 3, necking part of discontinuous phase extends without a break-up of droplet, since oil phase cannot penetrate enough to be exposed to the shear stress exerted by the water phase, so the evaluation of flow rates on porous structures was investigated only between 0.5 and 2 with chloroform. According to the shearing model in T-junction droplet forming, at high water flow rates the applied shear stress

on the droplet at the end of the neck decrease because of the increasing difference of the speeds of two phases. On the other hand, this case was not observed when DCM was used as discontinuous phase. This situation can be explained based on the viscosity difference between two solutions as can be seen in Table 4-2. Viscosities were measured for 10% PLGA-*b*-PEG in both DCM and chloroform as 13.2 and 24 mPa s, respectively. Table 4-2 summarizes the pore size values of the 2D honeycomb-like structures after drying. Pore sizes directly related with the volume of the droplets broken up through the stream as can be seen in Figure 4-5 and Figure 4-6. The diameters of the pores were ranging between 84 to 165 µm with less than 8% deviation from the average, as the water/oil flow rate range was 0.5 to 2.5 when DCM used as solvent. The increase in diameters was also observed at 300 µL/min water flow rate, however in this case deviation was calculated as 13%, which brought an irregularity in pore shapes and orientations as a result of the high diameter differences in droplet size, which can be seen in Figure 4-5f. Same increasing trend and uniformity in pore shapes were observed in chloroform samples. Average pore diameters were found between 76 to 151 µm with less than 7% deviation at all flow rate because of monodispersed droplet formation. In addition, statistical analysis was carried out according to the pore size calculations. Pore sizes for each flow rate assayed were found as statistically not different using DCM and $CHCl_3$ ($p > 0,05$). However, the increase in pore sizes at flow rate increments between 0.5 to 1, 1 to 1.5, 2 to 2.5 and 2.5 to 3 were found statistically different for DCM and 0.5 to 1 and 1.5 to 2 for $CHCl_3$ ($p < 0,05$).

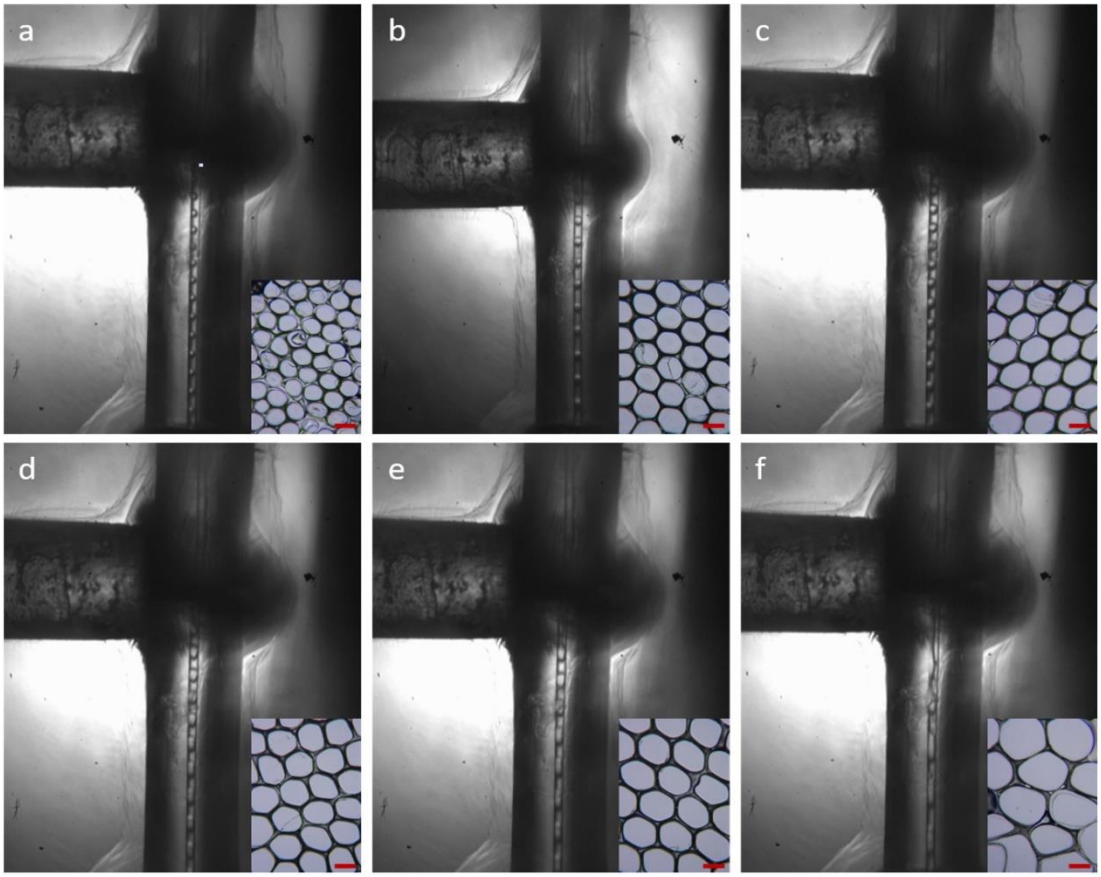

Figure 4-5: Effect of flow ratio on shapes and pore sizes of honeycomb-like structures formed using DCM. Flow rates (water/oil) are 0.5, 1, 1.5, 2, 2.5 and 3 for a to f, respectively. (Inset scale bars=100 µm)

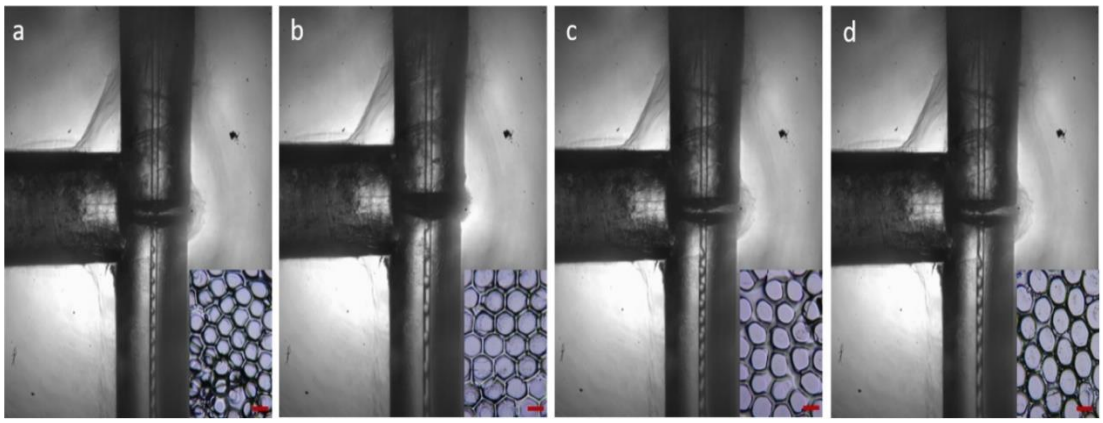

Figure 4-6: Effect of flow ratio on shapes and pore sizes of honeycomb-like structures formed using chloroform ($CHCl_3$). Flow rates (water/oil) are 0.5, 1, 1.5 and 2 for a to d, respectively. (Inset scale bars=100 µm).

		Flow rate (water/oil)					
	Solvent	0.5	1	1.5	2	2.5	3
Pore size (µm)	DCM	84±6	124±4	141±6	147±10	165±8	212±27
	Chloroform	76±3	129±6	134±5	151±10	N/A	N/A

Table 4-2: Effect of flow rate on pore size of honeycomb-like structures produced with % 10 (w/v) PLGA-*b*-PEG solution (N/A=not applicable).

4.1.2.3.2 Effect of polymer concentration on honeycomb-like structures

The structural and size-based investigation of honeycomb-like structures have been analysed when the PLGA-*b*-PEG concentration ranged between 2.5% and 10% (w/v). During the investigation water/oil phase flow rate was kept constant at 1 and monodispersed micro droplets were collected on glass slides. The average diameters were found to be decreasing with the increasing polymer concentration, nevertheless the change in size is not as remarkable as with flow rates as previously discussed. Table 4-3 summarizes the pore size investigation, with respect to PLGA-*b*-PEG concentration. The smallest pore diameter was measured as 124 µm at 10% (w/v) concentration of PLGA-*b*-PEG when DCM used as solvent. The same parameters resulted with 129 µm pores for the chloroform-based solution. The trend is also identical with 5% w/v PLGA-*b*-PEG concentration; however, 2.5% w/v solutions gives closer results for both solvents. At this point, relatively the large deviation in DCM solvent is remarkable and in addition to this, the distortion in porous pattern after bursting of perfectly aligned droplet structures is noticed. The source of this irregularity was observed as the rapid bursting of micro droplets which was caused by several factors as discussed below. Although both DCM and chloroform has the

same PLGA-*b*-PEG concentration, distorted patterns were only observed in DCM, which has lower viscosity with respect to chloroform i.e. viscosity value of PLGA-*b*-PEG (% 10 (w/w)) solution was found 13.2 mPa s for DCM and 24 mPa s for chloroform. As previously reported by Elsayed et al. (Elsayed et al., 2016), increasing the viscosity of the oil phase extend the life of the droplet surrounded by polymer, preventing chaotic pattern forming, which can be seen in the differences between the patterns in Figure 4-7a-c for DCM and d-f for chloroform. The pattern differences between two porous structures can also be related to the high vapour pressure of DCM. Micro droplets generated through the junction consists of aligned amphiphilic PLGA-*b*-PEG polymer chains, mainly deposited on the outer layer, because of interaction of PEG ends with water phase, as previously discussed. At low concentrations, deposited amount of polymer in the outer region cannot stabilize the spherical form of structure because of the high vapour pressure, leading to a quicker rupture of droplet. However, honeycomb-like membranes with uniform spherical pores were obtained with chloroform, because of the relatively low vapour pressure than DCM ($CHCl_3$:160 mmHg and DCM:353 mmHg at 20 °C). Both high viscosity and low vapour pressure of chloroform had a combined effect on droplet bursting, resulting in a uniformity in size. Wall struts of honeycomb-like structures were also observed to be thicker and denser, compared to DCM samples.

	Solvent	Concentration (w/w)		
		2.5	5	10
Pore size (μm)	DCM	141±17	126±7	124±4
	Chloroform	142±7	131±8	129±6

Table 4-3: Effect of PLGA-*b*-PEG concentration on pore size of honeycomb-like structures.

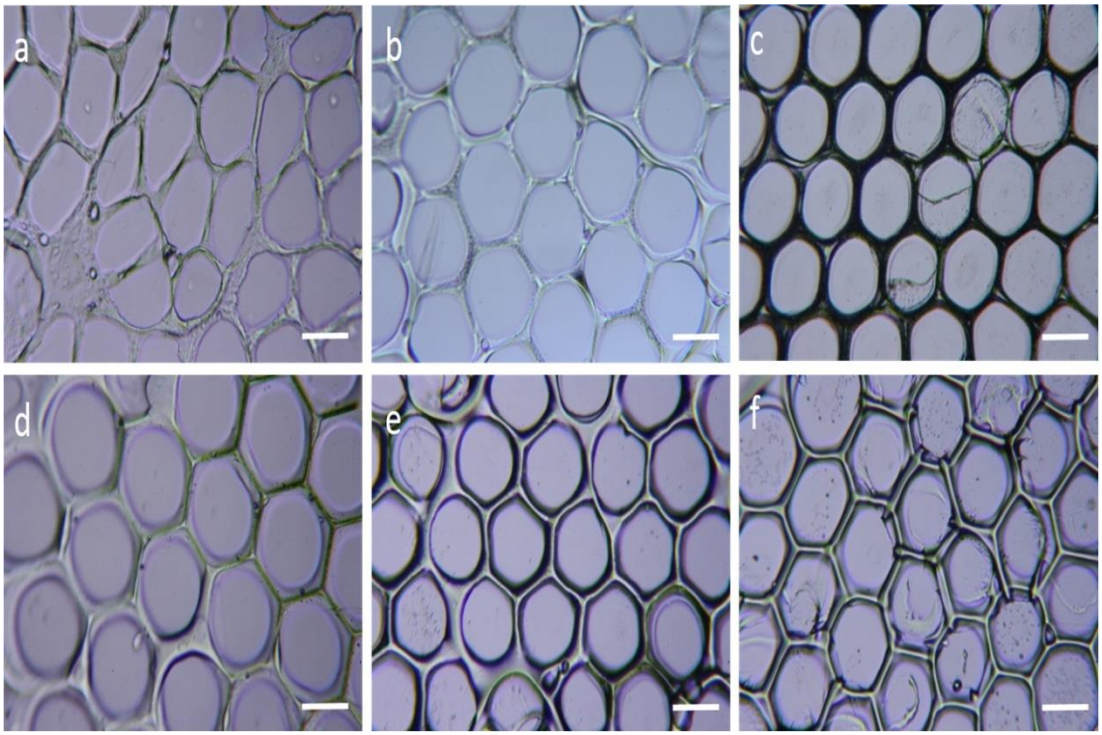

Figure 4-7: The effect of polymer concentration on honeycomb-like structure morphology in both DCM (a-c) and chloroform (d-f). PLGA-*b*-PEG concentrations are 2.5%, 5% and 10% by wt. from left to right, respectively. All scale bars indicate 100 μm.

4.1.2.3.3 Effect of solvent material properties on nanoparticle formation on structure

The effect of solvent type on honeycomb-like patterns was also investigated by a comparison between 5% PLGA-*b*-PEG solution (w/w) in both DCM and chloroform.

Although there were no major differences especially in size or morphology, as previously mentioned, tiny dark dots were noticed on honeycomb pattern struts in DCM (Figure 4-8d). During the high magnification SEM investigation, images of both samples were compared and spherical particles on DCM samples were noticed and further magnification of the area revealed that nanoparticles with size of 200-300 nanometres were embedded in the honeycomb strut walls. Breaking of fine droplets can give sub-micrometre size particles embedded in the structure after bursting (Elsayed et al., 2016). However, in our case nanoparticles were spherical and had low polydispersity. The mechanism of nanoparticle generation from oil droplets can be explained by the Marangoni bursting phenomenon, recently proposed by Keiser et al.(Keiser, Bense, Colinet, Bico, & Reyssat, 2017). The outer side of the PLGA-*b*-PEG containing DCM droplet evaporates at a rapid rate at the water-oil interphase. At this interface diffusion is controlled, as the polymeric PLGA-*b*-PEG nanoparticles can only form and disperse in the direction of the evaporating solvent. Nanoparticle generation is sourced to the small daughter droplets breaking from the main droplet and the mini-emulsions generated by the Marangoni effect, which was caused by the surface tension difference between the centre and the outer region (Visser, Kamperman, Karbaat, Lohse, & Karperien, 2018). The surface tension at the interphase where the emulsion created is lower than the centre of the droplet so there is a continuous flow of polymer chains (Kamaly et al., 2013). In this emulsion, daughter droplets disperse in the water phase and because of the amphiphilic nature of the PLGA-*b*-PEG, the orientation of chains are similar like surfactant structures, i.e. PEG blocks on the outer layer and longer PLGA chains entangled in the centre. Figure 4-8g shows the schematic representation of daughter droplet formation and

precipitation. As the solvent completely evaporates from the daughter droplets, homogeneous polymeric nanoparticles are formed owing to precipitation. This nanoprecipitation and instant forming phenomenon is addressed to interfacial interactions between two liquid phases (Luque-Alcaraz, Lizardi-Mendoza, Goycoolea, Higuera-Ciapara, & Argüelles-Monal, 2016). The formed particles up to complete burst of microfluidic droplet did not merge to create secondary structures since the solvent concentration (DCM) is too low to dissolve.

In contrast, this result was not observed in the case with use of chloroform as solvent, as can be seen in SEM image (Figure 4-8b). This discrepancy can be explained by the solubility difference between two solvents. Although both chloroform and DCM are known to be immiscible in water phase, the solubility of DCM is more than two times bigger than chloroform at ambient temperature, which makes DCM much more favoured in conventional nanoparticle synthesis (Baysal, Ucar, Gultekinoglu, Ulubayram, & Yabanoglu-Ciftci, 2017; Luque-Alcaraz et al., 2016). The Marangoni number (Ma) equation, which is defined as the proportion of thermal/surface tension forces divided by viscous forces is:

Equation 3

$$\mathbf{Ma} = -\frac{\boldsymbol{d\gamma}}{\boldsymbol{dT}}\frac{\boldsymbol{L\Delta T}}{\boldsymbol{\eta\alpha}}$$

Where “γ” is surface tension, “L” is length, “α” is thermal diffusivity, “η” is dynamic viscosity and “ΔT” is temperature difference (Guzman & Vasquez, 2016). Equation 3 explains the Marangoni flow is affected by several parameters, especially by temperature gradient between the surface and core of the droplet and viscosity

(Majumder et al., 2012; Rongy & De Wit, 2006). Since DCM has a lower boiling than chloroform the temperature at the outer layer is expected to be lower than that of chloroform, as the rest of the parameters are kept constant. Additionally, relatively high viscosity of chloroform compared to DCM with same concentration of PLGA-*b*-PEG, also decreases the Marangoni number, which reduces the Marangoni flow.

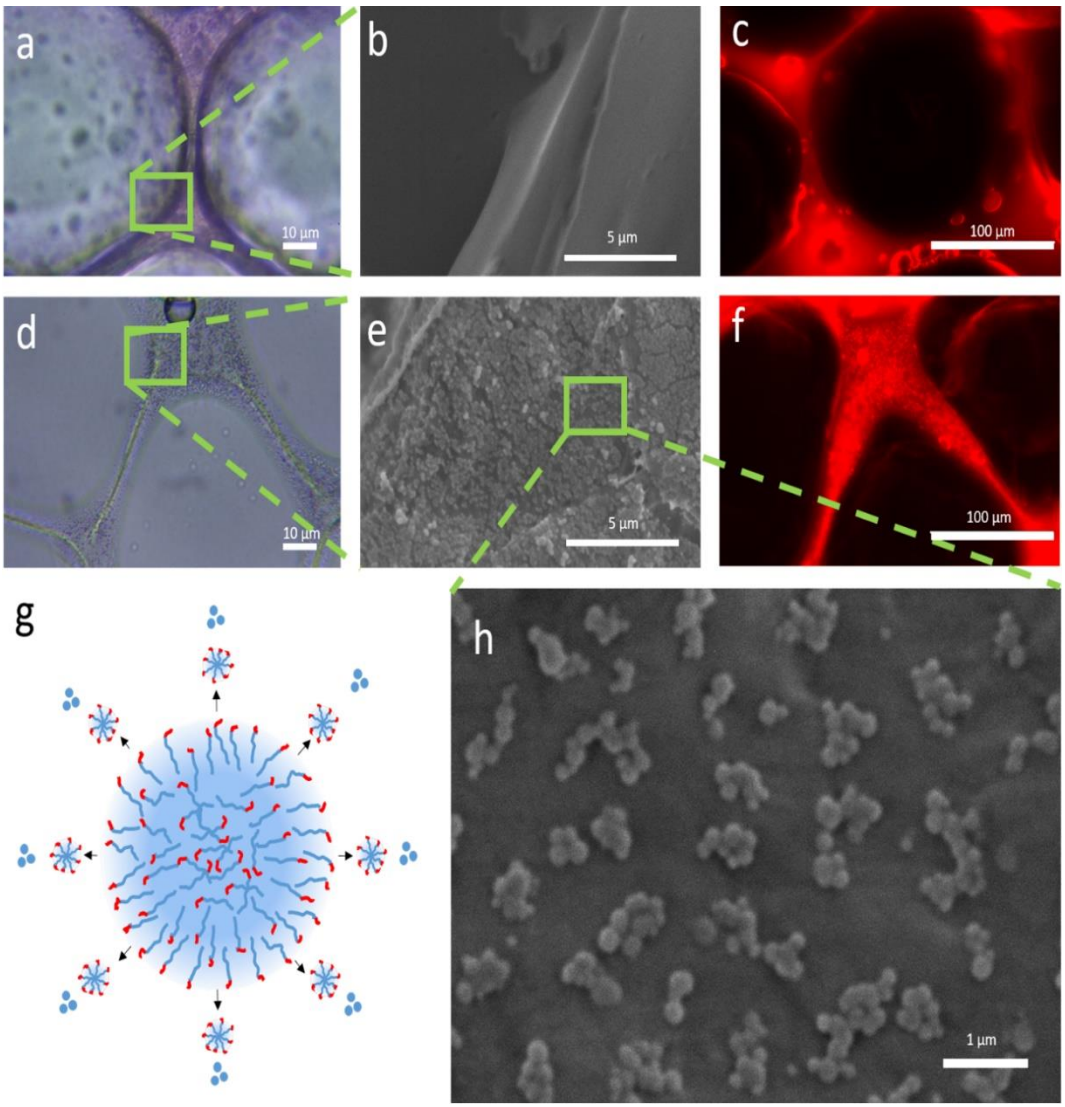

Figure 4-8: Solvent dependent nanoparticle formation on the PLGA-*b*-PEG honeycomb-like structure a)Optical microscope image of strut (scale bar=100µm), b)SEM image of strut (scale bar=5µm), c)Fluorescent microscope image of strut (scale bar=100µm) produced with chloroform as solvent, d)Optical microscope image of strut (scale bar=100µm), e)SEM image of strut (scale bar=5µm), f)Fluorescent microscope image of strut (scale bar=100µm) produced with DCM as solvent, g)Schematic representation of nanoparticle production via Marangoni bursting, h)SEM image of nanoparticles (scale bar=1µm) produced with DCM as solvent. Green boxes show nanoparticle absence (a) and presence (d and e).

4.1.3 Self-assembled micro-stripe polymer patterning with sessile nanofluid droplets

4.1.3.1 Material properties of PLGA-b-PEG in acetonitrile

PLGA-*b*-PEG nanoparticles were produced by microfluidic T-junction device and nanofluid production by the hydrodynamic flow focusing. Before feeding into T-junction microfluidic device, polymer solutions were characterized in terms of surface tension and viscosity. For 2.5, 5 and 10 % (w/v) concentration polymer solutions, surface tension values were determined as 13.2, 13.3 and 13.1 mN/m and viscosity values were found 0.8, 1.7 and 7.4 mPa, respectively (Table 4-4)

Polymer* concentration % (w/v)	Surface tension (mN/m)	Viscosity (mPa s)
2.5	13.2±0.02	0.8±0.3
5	13.3±0.01	1.7±0.1
10	13.1±0.01	7.4±0.7

Table 4-4: Solution properties of PLGA-b-PEG in acetonitrile

4.1.3.2 Formation of nanoparticles with T-junction device

Hydrodynamic flow focusing was performed in the T-junction with serial concentrations of PLGA-*b*-PEG in acetonitrile as oil phase. A soft boundary was formed by overlapping the oil and water phase in the centre of the outlet tubing of T-junction, due to the miscibility of acetonitrile and water. Furthermore, the width of soft boundary co-axial channel can be controlled by tailoring the liquid flow rates of two miscible liquid phases. Meanwhile, the size and yield of nanoparticles were proportional to the width of co-axial channel. Equation 4 represents the two-

dimensional hydrodynamic flow focusing model through the relationship between the fluid streams, diffusion and the flow rate of streams. In the Equation 4, τ_{mix} represents the mixing time of two adjacent streams and can be estimated from the flow ratios (R) of them through the equation. D represents the diffusivity of solvent, w_f is the focused stream width, w is the width of the channel (Karnik et al., 2008; Leung & Shen, 2018).

Equation 4

$$\tau_{\text{mix}} \sim \frac{w_f^2}{4D} \approx \frac{w^2}{9D} \frac{1}{(1+\frac{1}{R})^2}$$

Water and oil phases were fed into T-junction microfluidic device from different channels (x and y directions) with different flow rates. During the study, water phase was varied as 50, 100 and 150 µl/min at constant flow rate of oil phase (50 µl/min). In the T-junction device, when water run into oil phase, PLGA-*b*-PEG precipitated directly in the water phase and the nanoparticle formation occurred.

4.1.3.3 Effect of material properties on size of nanoparticles

It was found that PLGA-*b*-PEG concentration affected the nanoparticle properties (Table 4-5), this was confirmed by both DLS and SAXS measurements. From DLS dataset collected under constant flow ratio of 1:1, average nanoparticle size was determined to be 152 nm for 2.5 % PLGA-*b*-PEG. It decreased to 107 nm for 5% PLGA-*b*-PEG and then further decreased to 94 nm for 10 % PLGA-*b*-PEG. From SAXS dataset of the same constant follow ratio, average nanoparticle size was determined to be 128 nm for 2.5% PLGA-*b*-PEG, decreased to 106 nm for 5% PLGA-*b*-PEG and 94 nm

for 10% PLGA-*b*-PEG. In addition, similar decreasing trend was observed at higher water/oil flow ratio. Average particle sizes were measured as 144 nm, 107 nm and 102 nm at flow ratio 2 and 132 nm, 108 nm and 104 nm at flow ratio 3 for 2.5, 5 and 10 % PLGA-*b*-PEG respectively by DLS. Average particle sizes were 112 nm, 107 nm and 94 nm at flow rate ratio 2 and 128 nm, 109 nm and 100 nm at flow rate ratio 3 under 2.5%, 5% and 10 % PLGA-*b*-PEG respectively by SAXS. Moreover, increasing polymer concentration caused an increase in zeta potential values. Zeta potential value was -13.5 mV for 2.5 % PLGA-*b*-PEG, -8.5 mV for 5 % PLGA-*b*-PEG and -7.2 mV for 10 % PLGA-b-PEG at water/oil flow ratio kept 1 (50:50 µl/min).

It was concluded that increasing polymer concentration decreased size and increased zeta potential of nanoparticles (Figure 4-9A-B). Nanoparticle sizes measured by DLS in solution are larger than those measured by SAXS in solid state (Figure 4-9C). This is likely to be caused by the continuous growth of nanoparticles in liquid state caused by prolonged the interaction time between PEG hydrophilic chains and water. Cheng et al(Cheng et al., 2007) also concluded that PLGA-*b*-PEG nanoparticles size varies at different polymer concentrations in organic solvent but at a fixed PLGA-*b*-PEG concentration, water/oil phase differs particle size very slightly. In addition, Şimşek et al (Şimşek, Eroğlu, Kurum, & Ulubayram, 2013) reported that, in a conventional nanoprecipitation system, increasing PLGA-*b*-PEG concentration increases nanoparticle size, whereas constant PLGA-*b*-PEG concentration with increased PEG content decreases nanoparticles size.

This also showed that, obtained PLGA-*b*-PEG nanoparticles are highly mono dispersed, that the polydispersity index (PDI) is ranged between 0.17-0.04. In the

literature, PLGA-*b*-PEG nanoparticles PDI is generally around 0.2 (Baysal et al., 2017; Sari et al., 2015). In our case especially 5 % PLGA-*b*-PEG generated highly monodisperse nanoparticles with 0.06, 0.05 and 0.04 PDI values for 1, 2 and 3 water/oil flow rates respectively which is a very remarkable result compared with the literature.

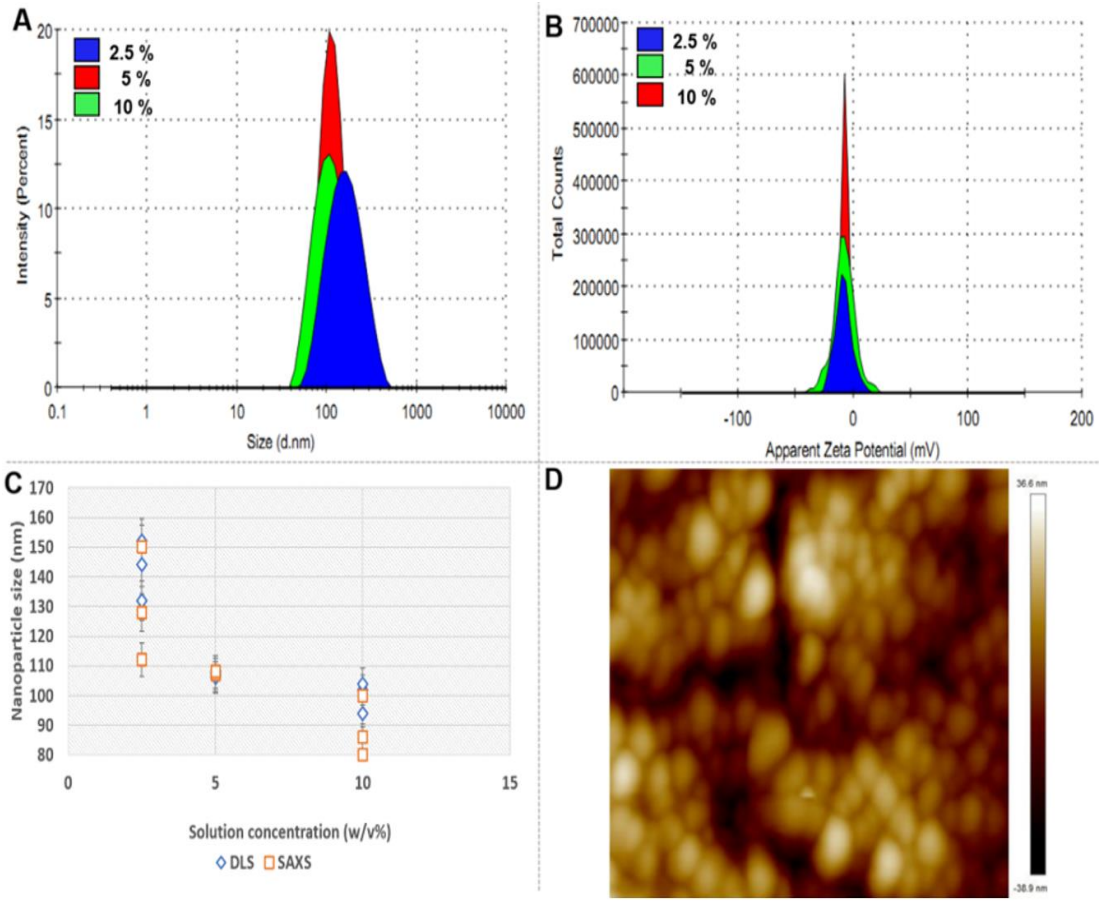

Figure 4-9: PLGA-*b*-PEG nanoparticles. A) average particle size (nm) and B) zeta potential (mV) distribution graphs of 2.5 %, 5 % and 10 % PLGA-*b*-PEG solutions (50:50 oil/water flow ratio), C) comparative size distribution graph of 2.5 %, 5 % and 10 % PLGA-b-PEG solutions, D) AFM micrograph of PLGA-*b*-PEG nanoparticles (50:50 oil/water flow ratio, 5 % w/v concentration).

In the Figure 4-9, comparative size (Figure 4-9A) and zeta potential (Figure 4-9B) graphs represent the concentration gradient for 2.5%, 5 % and 10% PLGA-*b*-PEG at flow ratio 1. In addition, PLGA-*b*-PEG nanoparticles size and morphology were also

investigated by AFM. Figure 4-9 D shows the AFM micrograph of highly monodisperse nanoparticles 5 % PLGA-*b*-PEG at flow ratio 1. AFM micrograph proved that the synthesized nanoparticles have spherical morphology and their size is around 100 nm. Then, 5% PLGA-*b*-PEG was chosen as representative group to study the effect of polymer concentration on nanoparticle size which analysed by DLS, SAXS and WAXS.

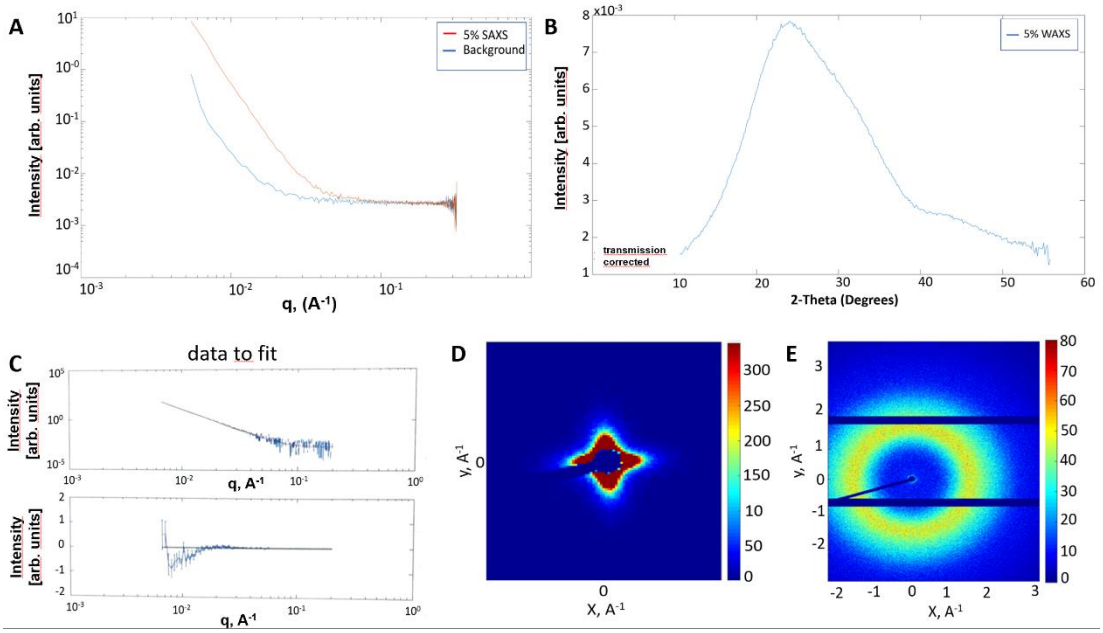

Figure 4-10: PLGA-*b*-PEG nanoparticles were initially formed in 5 % concentration solution at flow rate ratio of 1 and then measured in their native state by SAXS/WAXS. A) Log-log plot of SAXS scattering pattern, B) Lin-lin plot of WAXS scattering pattern shown in 2-theta configuration, C) full fit curve matched with data after subtract background, D) 2D scattering pattern collected in SAXS, E) 2D scattering pattern collected in WAXS configuration for sample 5 %.

It is known that results from SEM and DLS involve different kinds of post-synthesis operations, this may have huge impact on the particle size. For this reason, a specially-designed thin-film cell holder was employed in SAXS/WAXS technique to examine the particles in their native state on the glass cover, following pattern formation and drying. No grinding, post-preparation or any disturbance is introduced to the sample prior to the SAXS measurements. A custom-made sample holder fitted

with ACADEMY background cover slips was used to obtain structural information of the thin film nanoparticles in their native state. The difference between red curve (scattering from the sample) and blue curve (scattering from the blank glass cover, which is subtracted as the background) showed that that the noise-to-signal ratio is very low and therefore strong SAXS signals were collected to reveal true features of the nanoparticles (Figure 4-10A). It proved that this cost-effective cover slides are great substrates for nanoparticle thin films, they are also good alternatives to scatterless MICA/Kapton films which were widely used as window/background materials in SAXS measurement.

Here, The WAXS curve collected (Figure 4-10B) showed a typical amorphous scattering pattern with a very board (amorphous) bump. It is clear that PLGA-*b*-PEG nanoparticles remained amorphous during self-assembling and pattern formation processed. The observed high stability of this amorphous property is often key and preferred for optimising drug delivery, as unwanted crystallization or low bioavailability/dissolution rate have huge impact on drug safety, drug patent protection and other drastic issues in pharmaceutical industries.

Here 'SAXSGUI' was used to do 'Full Fit' from the background subtracted data to obtain particle size information (Figure 4-10C). A polydispersed sphere model was used to fit the curve, and a Gaussian distribution was applied as it is known that the nanoparticles are spherical with some degree of polydispersity (5% polydispersity from DLS measurement). The particle size determined by SAXS (106nm) is smaller than those obtained from the DLS (107nm) analysis. This small difference is expected because DLS gives hydrodynamic radius which is known to be bigger than the so

called ‘true radius’ measured from SAXS or microscopy. This indicated that in the process of the self-assembling and specific pattern formation, there is subtle change (or even no change) of these nanoparticle sizes from suspension state to solid state.

PLGA-*b*-PEG % (w/v)	Water/oil Flow ratio	Size (nm)	Poly dispersity index (PDI)	Zeta Potential (mV)	Pattern formation
2.5	1	152 ± 2	0.15	-13.5	Coffee-ring
	2	144 ± 1	0.14	-7.7	Coffee-ring
	3	132 ± 1	0.12	-7.2	Coffee-ring
5	1	107 ± 1	0.06	-8.5	Highly ordered micro stripes
	2	107 ± 1	0.05	-8.5	Highly ordered micro stripes
	3	108 ± 1	0.04	-6.4	Highly ordered micro stripes
10	1	94 ± 1	0.15	-7.2	Micro stripes
	2	102 ± 1	0.17	-7.7	Micro stripes
	3	104 ± 1	0.16	-6.3	Micro stripes

Table 4-5: The effect of PLGA-*b*-PEG concentration and water/oil flow ratio in the microfluidic device on nanoparticles properties and deposited pattern

4.1.3.4 Formation of micro-stripe patterning

At the first part of the study, synthesis of highly monodisperse PLGA-*b*-PEG nanoparticles with hydrodynamic flow focusing technique was achieved. Subsequently, PLGA-*b*-PEG nanoparticles were dried in a sessile droplet to generate self-assemble patterns. In the literature, most of the researchers focused on the self-assembling of nanoparticles with the aid of pH, light, polarity, temperature, hydrophobicity, metallic interactions etc (Y. Chen et al., 2018; Grzelczak, Vermant, Furst, & Liz-Marza, 2010; Sánchez-Iglesias et al., 2012). On the other hand, this study was focused on the self-assembling patterns created by drying sessile droplets of polymeric nanoparticle suspensions. The nanofluids, meaning nano-colloidal solutions, are made from nanoparticle suspension (Choi, 2008; Zhong, Crivoi, & Duan, 2015). Here, PLGA-*b*-PEG nanofluids were collected on a glass slide as sessile droplets

and dried at ambient conditions. After drying period, both snow flake and linear self-assembled structures with micro stripe conformation were obtained. In the Figure 4-11, optical microscope images of self-assembled PLGA-*b*-PEG nanoparticle patterns were shown at a fixed water/oil flow ratio (50:50 oil/water flow ratio) and different concentration of polymer solutions. In the Figure 4-11A, 2.5 % w/v concentration of PLGA-*b*-PEG solution was used but the obtained patterns do not have highly ordered stripes, which are not linear as well. Figure 4-11A have more randomized patterns than Figure 4-11B-C. Amongst three figures, Figure 4-11B, PLGA-*b*-PEG NPs has the most uniform and highly ordered linear patterns. This tendency can be explained with the extremely low PDI of 5 % PLGA-*b*-PEG such that PDI of Figure 4-11A and C are 0.15 whereas Figure 4-11B is 0.06. Figure 4-11C have uniform linear patterns as well but they are thicker than the Figure 4-11B since Figure 4-11C has higher polymer concentration (10 %) and higher concentration of nanoparticles in an equal amount of sessile droplet.

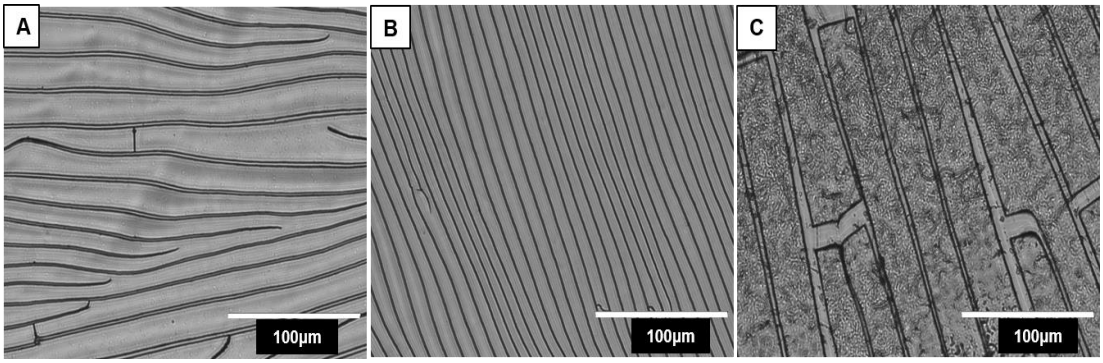

Figure 4-11: Optical microscope images of deposited pattern. A) 2.5 % B) 5 % and C) 10 % w/v concentration of PLGA-*b*-PEG solutions after nanoparticle fabrication and sessile drop drying of nano-fluids (50:50 oil/water flow ratio).

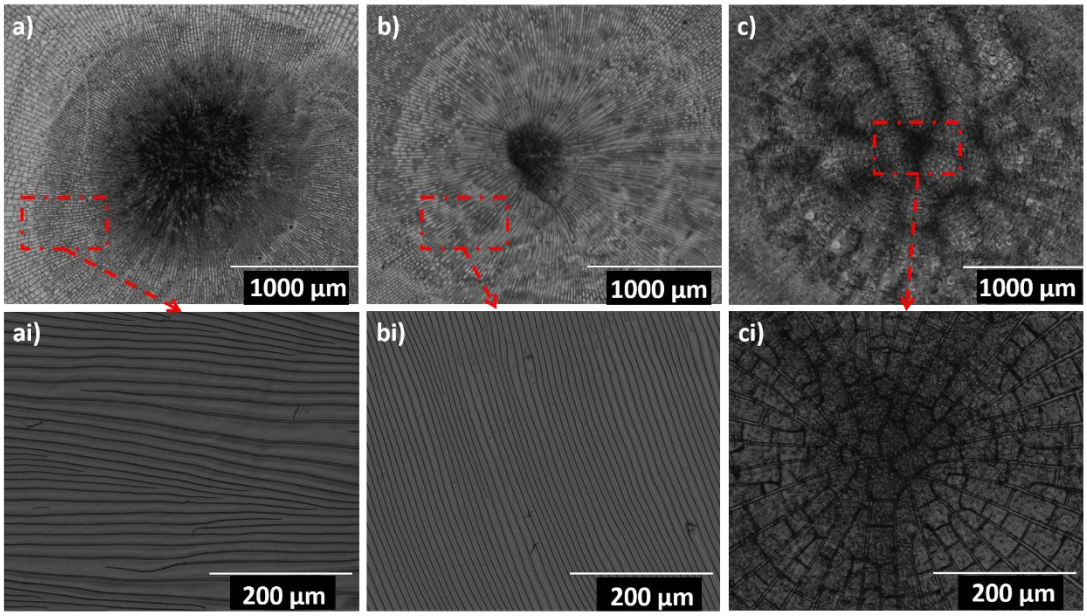

Figure 4-12: Optical microscope images of deposited pattern in overall region. a) 2.5%, b)5% and c) 10% w/v concentration of PLGA-PEG solutions after nanoparticle fabrication and sessile drop drying of nano-fluids (50:50 oil/water flow ratio). Image a), b) and c) were taken under optical microscope with x4 magnification. ai), bi) and ci) were the enlarged area from image a), b) and c), examined under optical microscope with x20 maginification.

Contact angle values of PLGA-*b*-PEG nanofluids were determined by sessile drop technique on a glass slide. Because of using glass slide as collector during the whole study it is important to determine and compare solution characteristic on the same surface. The contact angle of water on a glass is ~20° in the literature (Ozkan & Erbil, 2017). In this study oil/water flow ratio was fixed at 1 (50:50) and contact angle of 2.5 %, 5 % and 10 % w/v concentration of PLGA-*b*-PEG solutions were measured after nanoparticle fabrication. The contact angle results were tabulated in the Table 4-6. The results showed that, increasing polymer concentration increased contact angle values as well. Contact angles of 2.5 % and 5 % w/v PLGA-*b*-PEG were found as 12.3° and 13.6° respectively. On the other hand, 10 % w/v PLGA-*b*-PEG concentration increased contact angle value to 25.2° since the increasing amount of hydrophobic polymer content of nanofluid solution decreased hydrophilicity with increasing

contact angle. Vafaei et al (Vafaei et al., 2006) studied the effect of nanofluid concentration on surface wettability and stated that the contact angle of nanofluids increase with increasing concentration.

Solution	Polymer	Oil/water flow ratio	Concentration % (w/v)	Contact Angle°
1	PLGA-*b*-PEG	50:50	2.5	12.3
2	PLGA-*b*-PEG	50:50	5	13.6
3	PLGA-*b*-PEG	50:50	10	25.2

Table 4-6: Contact angle values of PLGA-*b*-PEG nanoparticle contained nanofluids

Sessile nanofluid droplets were produced from 50:50 oil/water flow ratio for 2.5, 5 and 10 % (w/v) of PLGA-b-PEG in acetonitrile and then collected on the glass slide surface directly. The sessile droplets dried at ambient conditions and different patterns were spotted out for different PLGA-*b*-PEG polymer concentrations. The obtained patterns monitored by fluorescence and optical microscopy as shown in Figure 4-13. Evaporation of sessile nanofluid droplets is driven by two main flow regimes which are Capillary flow and Marangoni flow (Karpitschka, Liebig, & Riegler, 2017; Parsa, Harmand, & Sefiane, 2018). Here, nanofluid droplet which was prepared from 2.5 % (w/v) concentration of PLGA-*b*-PEG, created coffee-ring deposition with snow flake fingering structures in the central (Figure 4-13A-D). On the other hand, nanofluids from 5 and 10 % (w/v) concentration of PLGA-*b*-PEG created self-assembled and highly ordered micro stipe patterns after drying (Figure 4-13B-E and Figure 4-13C-F). Deegan et al.(Deegan et al., 1997) reported that, coffee-ring deposition is forced by Capillary flow which starts from a pinned contact line (CL). Moreover, Hu and Larson explained that Marangoni effect should be supressed to

obtain coffee-ring deposits. Because, Marangoni effect forces to obtain self-assembled highly ordered pattern (Hu & Larson, 2005b, 2005a). Here, sessile drops of nanofluid solutions dried sequentially. Vapour pressure of acetonitrile is higher than water, hence acetonitrile evaporates at first. Acetonitrile concentration becomes higher at the edge of sessile droplet and reduces the surface tension of droplet. Marangoni flow was induced by the change in surface tension and recirculation occurred inside the sessile droplet. The Stokes equation (Equation 5) gives the relationship between the gravitational force, settling velocity, density, viscosity and the particle size (Majumder et al., 2012).

Equation 5

$$Vs = \frac{2}{9}\frac{(\rho_p - \rho_f)}{\mu} gR^2$$

Where Vs is the settling velocity, ρ_p is particle density, ρ_f is the nanofluid density, μ is nanofluid dynamic viscosity, g is gravity and R is the radius of the nanoparticles.

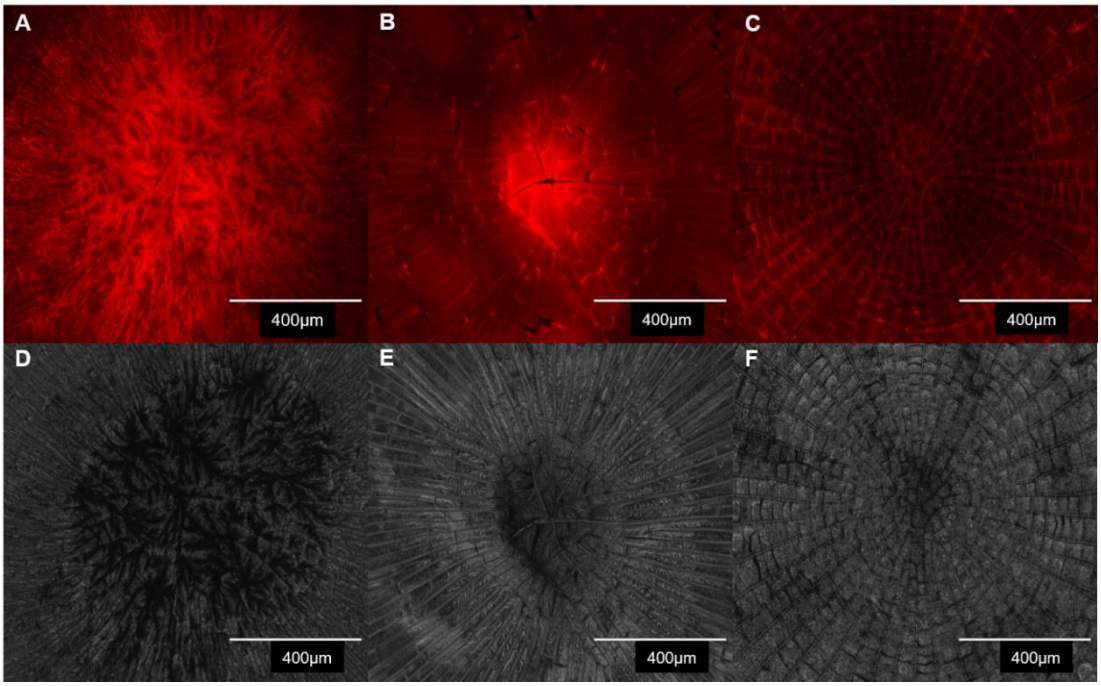

Figure 4-13: Fluorescence and optical microscope images of self-assembled PLGA-*b*-PEG nanoparticle layers produced at 50:50 oil/water flow ratio with different polymer concentration. A) 2.5% B) 5 % C) 10 % (w/v) of PLGA-*b*-PEG in acetonitrile (fluorescence microscope images). D) 2.5% E) 5 % F) 10 % (w/v) of PLGA-*b*-PEG in acetonitrile (optical microscope images) (Scale bar: 400 µm).

Marangoni effect was suppressed for 2.5 % (w/v) concentration of PLGA-b-PEG sample group and the snow flake coffee-ring deposits were obtained (Figure 4-14A-D). Besides, 5 % and 10 % (w/v) concentration of PLGA-b-PEG were performed ordered micro stripe patterning due to the Marangoni flow with the optimal particle size for self-assembly patterns (Figure 4-14B-C-E-F). Shen et al (X. Shen, Ho, & Wong, 2010) reported that, coffee-ring structure formation have a threshold particle size. They reported that, polystyrene latex particles can form coffee-ring structure with 100 nm nanoparticles but smaller size (60 nm and 20 nm) nanoparticles form uniform pancake patterns. In our study, Figure 4-13A-D snow flake patterns resulted in with 150 nm nanoparticle size, otherwise uniform stripes were obtained at Figure 4-13B-E and Figure 4-13C-F with 107 nm and 94 nm nanoparticle sizes respectively. In the

present study, uniform stripe formation threshold was found ~100 nm for PLGA-*b*-PEG nanoparticles. Cai et al (Cai & Newby, 2008) also reported that 100 nm polystyrene NPs were assembled stripe like patterns with the Marangoni flow. This particle size threshold can be clarifying with the Equation 5. Because nanoparticles circulation velocity is proportional to the square of particle radius. Moreover, velocity and flow type affected not only by particle size but also density of nanoparticles and nanofluids. For instance, 5 and 10 % w/v concentration of PLGA-*b*-PEG have the same particle size and they both deposited as micro stripe patterning. Besides, 5 % sample group have highly ordered micro stripe patterns due to the lower particle and nanofluid density gradient (Equation 5). It was also concluded that highly monodisperse (relatively low PDI) particles deposits as thinner stripes (Figure 4-11B-C and Figure 4-13B-C).

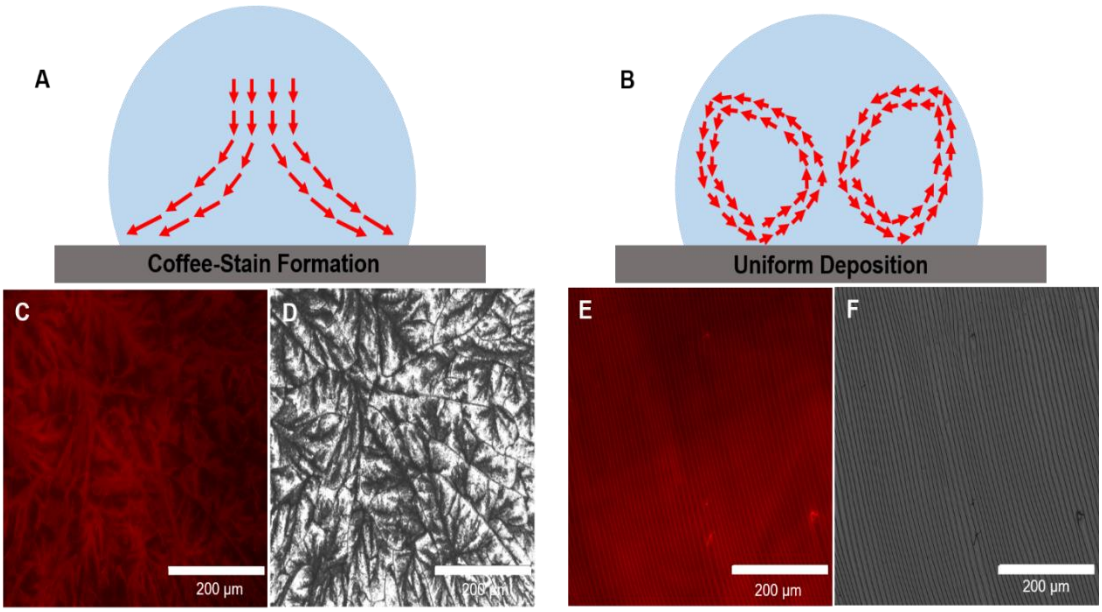

Figure 4-14: Schematic representation of nanoparticles motion at A) coffee-stain formation, B) uniform deposition, (C-E) fluorescence microscope and (D-F) optical microscope images of coffee-stain and uniform deposition of 2.5 and 5 % (w/v) concentration of PLGA-*b*-PEG nanofluids respectively (50:50 oil/water flow ratio).

The uniform strip formation was monitored by optical microscope in a time dependent manner in Figure 4-15 for 5 % w/v concentration of PLGA-*b*-PEG sample group. Stripes are growing continuously by ~100 nm nanoparticles at 2 seconds intervals from Figure 4-15-A to Figure 4-15-H. Stripes have uniform morphology in terms of both linearity and diameter with the aid of Marangoni recirculation inside the sessile nanofluid droplet.

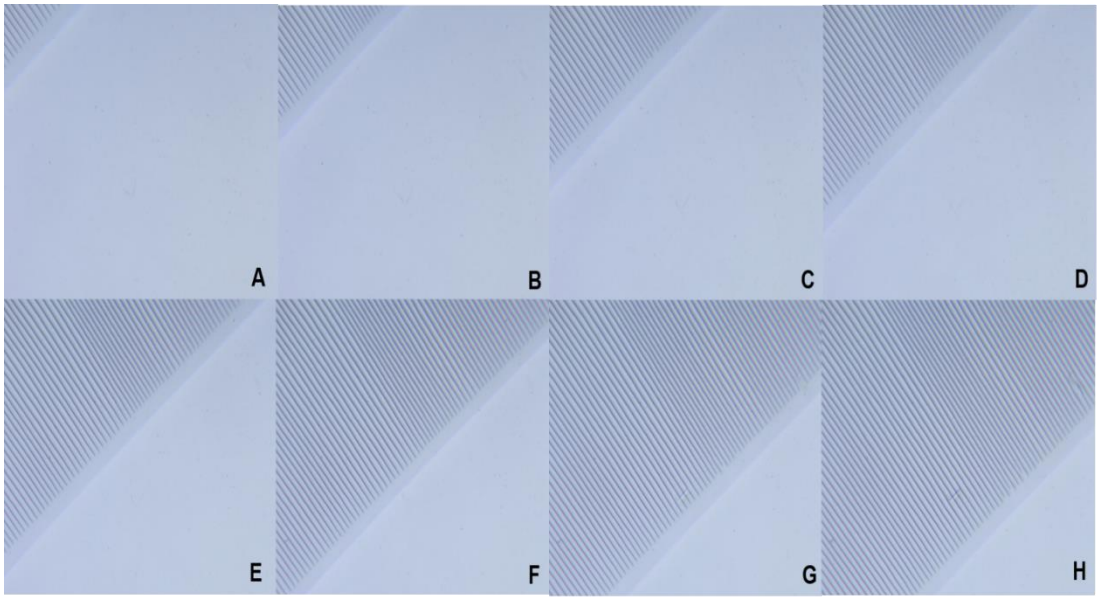

Figure 4-15: Optical microscope images of 5 % w/v concentration of PLGA-*b*-PEG solutions after nanoparticle fabrication and sessile drop drying by the time (A-H, time intervals=2 seconds, 50:50 oil/water flow ratio).

The uniform stripe patterns and the nanoparticles they contain are shown in Figure 4-16 with SEM micrographs. Figure 4-16A shows that, self-assembled stripes were deposited in 3D structures. In addition, Figure 4-16B and Figure 4-16C showed clearly that the stripes are composed of nanoparticles directly. Also, nanoparticles were shown at Figure 4-16D-F at different magnifications and the nanoparticles size are confirmed by SEM, DLS measurement and AFM results with ~100 nm particle size.

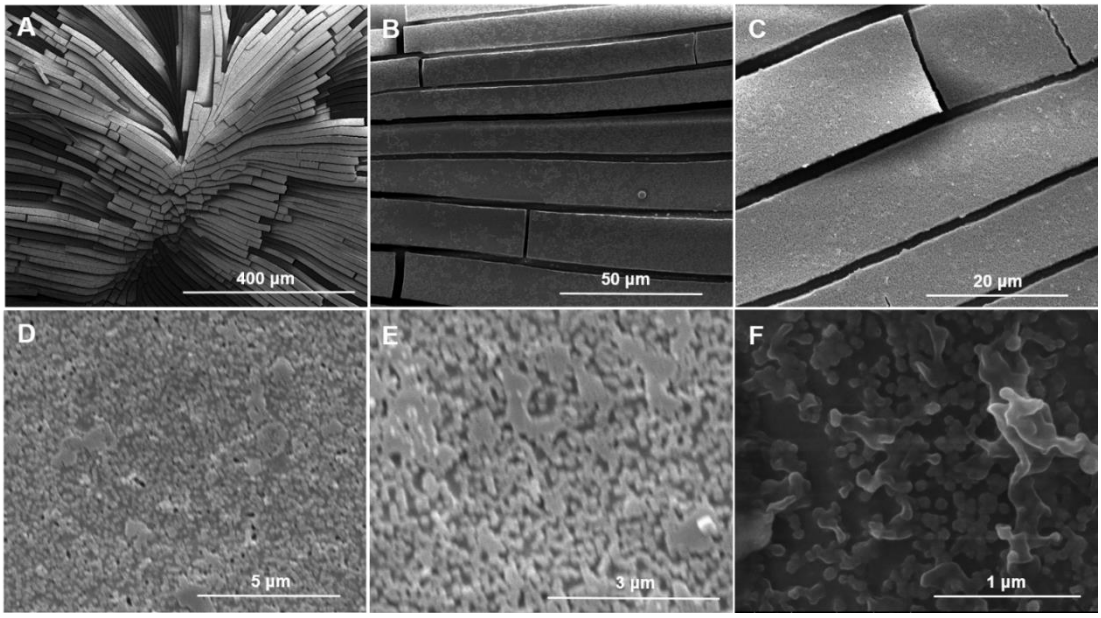

Figure 4-16: Scanning Electron Microscopy (SEM) micrographs of self-assembled nanoparticles fabricated from 5 % w/v concentration of PLGA-*b*-PEG solutions. A) 400µm B) 50µm C) 20µm D) 5µm E) 3µm and F) 1µm scale bar.

4.1.4 Summary

In this study, single T-junction shows the great potential to precisely control the size and formation of scaffolds and nanoparticles. The effect of material properties on the formation of micro droplets and nanoparticles was systematically studied in this chapter. In section 4.1.2, PLGA-*b*-PEG porous structures with a honeycomb-like surface pattern were obtained via highly uniformed micro droplets generated with a T-junction microfluidics system. Micro droplets were collected on glass slides and porous structures were obtained after the bursting of droplets. In addition to that, nanoparticle embedded struts were also noticed in some samples indicating that PLGA-*b*-PEG gathered at the edge of the droplet creating a ring structure. The break-up of this ring before complete bursting of the micrometre size droplet results in nanoparticle formation. T-junction processing of honeycomb-like surfaces has great potential and can be used in biomedical applications, especially in drug delivery

related studies with nanoparticle forming ability and cellular responses to different surface morphologies. In section 4.1.3, highly monodisperse PLGA-*b*-PEG nanoparticles were obtained by surfactant free hydrodynamic flow focusing technique in a T-junction microfluidic device. Synthesized nanoparticles were collected as nanofluid solutions and the nanofluids were dried on the glass slides as sessile droplets. Due to the internal flow type of the sessile droplets, different deposition patterns were obtained on the glass slides. Internal flow type and the related deposition patterns are affected by the polymer concentration, nanoparticles size and polydispersity index. PLGA-*b*-PEG nanoparticles which have extremely low PDI and ~ 100 nm particle size, deposited as highly uniform self-assembled parallel stripes. T-junction microfluidic devices are ideal systems for the surfactant free, highly monodisperse nanoparticle fabrication and these nanoparticles exhibit highly ordered and self-assembled stripe patterns under optimized conditions.

4.2 Double T-junction and its bioengineering product: double layered microbubbles

4.2.1 Overview of double T-junction microfluidic device processing

Microbubbles can be applied to a wide variety of biomedical applications due to their good size uniformity and stability (Hernot & Klibanov, 2008b). Different sizes are required for different types of applications. For instance, to achieve the desired scaffold porosity, the ideal range for microbubbles' sizes is between 200 µm to 400 µm to ensure sufficient oxygen and nutrient exchange from the scaffold matrix to its surroundings (Bružauskaitė et al., 2016). However, to produce microbubbles for ultrasound contrast agents, microbubble size has to be smaller than 8 µm to avoid clogging vessels and to overcome the surrounding blood stream distortion (Gorce et

al., 2000). However, it is still a challenge to produce 8 µm microbubbles by microfluidic techniques especially with microfluidic T-junction devices. This is due to the size of microbubbles being confined by the channel size.

To produce suitable sized microbubbles as ultrasound contrast agents, the microfluidic channel size must be around 10 µm. However, it is very easy to block small channels with a viscous solution. Hence, a coarse channel size of 200µm was chosen to assemble the double T-junction microfluidic devices in this work. Material properties (viscosity and surface tension) can also alter microbubble size in microfluidic T-junction (Glawdel et al., 2012). To reduce microbubble size with constant material viscosity and coarse channel size, a double T-junction device was assembled. Here, the aim of this body of work is to investigate the microbubble size reduction with the aid of a second T-junction.

In section 4.2.2, monodispersed BSA microbubbles were successfully produced with a double T-junction device presented in this work. The effect of the second T-junction on microbubble formation was investigated in section 4.2.2.1. The correlation between microbubble size and gas-liquid flow rate ratio is shown in section 4.2.2.2. Microbubble productivity can be calculated by channel length and bubble residence time. The microbubble productivity and stability of single and double T-junction can be seen in sections 4.2.2.4 and 4.2.2.5.

In section 4.2.3, two verification experiments were done to check firstly the feasibility of microbubble production though double T-junction. Secondly the feasibility of microbubble production though triple T-junction. In section 4.2.3.1, Polyoxyethylene

40 stearate was added to glycerol as a surfactant. This mixture was used as the polymer solution to generate microbubbles with a double T-junction device. In section 4.2.3.2, a triple T-junction device was assembled, and monodispersed microbubbles were produced. The effect of gas pressure and liquid flow rates on bubble size has also been investigated.

In section 4.2.4, an attempt at producing of double layered microbubbles was successfully completed.

4.2.2 Monodispersed BSA microbubbles produced by double T-junction

4.2.2.1 Effect of the addition of the second T-junction on the formation of microbubbles

In this part of the work, high speed video images were used to analyse how the addition of the second T-junction affects the flow and shape of microbubbles within the microchannels. At a constant liquid flow rate of 100 µl/min for both liquid inlet channels, gas pressure was increased from 130±5 to 190±7 kPa (experiments have been repeated three times). As shown in the micrographs in Figure. 4-17 a)i-c)i, by increasing the gas pressure, microbubble size increased in the same manner as a single T-junction from 220 to 340 µm. The shape of microbubbles within the channels changed from nearly spherical to plug-like by increasing the gas pressure, which lead to a larger microbubble diameter after collection. Another factor that was observed through the high-speed camera images is that by introducing the second T-junction, the distance between generated microbubbles was increased in all the cases after they passed through the second T-junction. For instance, the initial distance between two microbubbles prior to passing the second T-junction was L_1=410 µm at gas

pressure of 130 kPa, which increased to L_2=620 µm. The same trend was detected for higher gas pressures (Figure. 4-17 a)ii, b)ii and c)ii). This can be explained as being caused by introduction of an additional liquid flow in the second T-junction that increases the liquid phase velocity in the second T-junction and hence the liquid phase pushes the adjacent microbubbles away from each other.

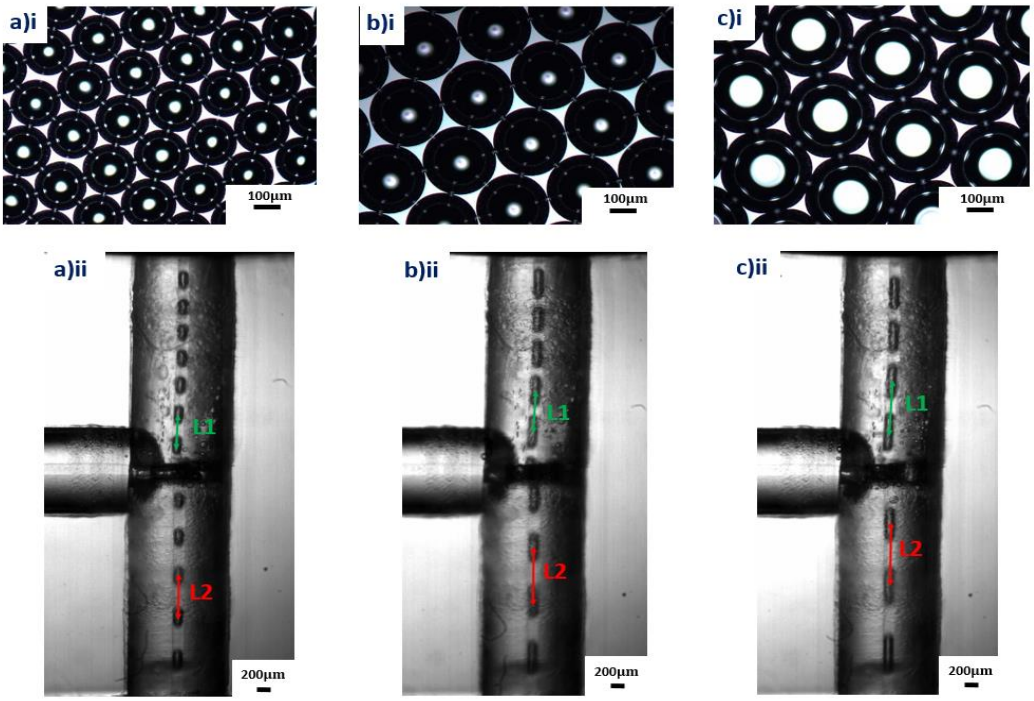

Figure. 4-17: Micrographs and high speed camera images of microbubbles produced in the double T-junction geometry at a constant flow rate of 100µl/min and gas pressures of a) 130±5, b) 160±10 and c) 190±7 kPa. Microbubble diameter, L1 and L2 for each case (in µm) is a) 220, 410, 620, b) 280, 715, 995 and c) 340, 945, 1080.

4.2.2.2 Effect of flow rate and geometry on microbubble diameter

Flow rates of 100 and 200 µl/min were selected and applied to both the single and double T-junctions. Once the microbubbles were formed at the minimum gas pressure for a given flow rate, the gas pressure was systematically increased. The flow rate ratios as well as the microfluidic geometry determine the minimum gas pressure that enables microbubble production. In order to determine this minimum

value, gas pressure was increased slowly until microbubbling was achieved. The minimum gas pressures that produced the smallest microbubbles using the single T-junction at flow rate of 100 and 200 µl/min were 15 and 20 kPa, respectively. The value of the minimum gas pressure was increased to 20 and 30 kPa with flow rates of 100 and 200 µl/min, respectively using the double T-junction. Microbubbles were not formed below the minimum gas pressure of both single and double T-junctions. Microbubble formation in a microfluidic device is governed by the pressure balance between continuous and disperse phase at the junction (Castro-Hernández, van Hoeve, Lohse, & Gordillo, 2011). Generally, the fluid phase is infused into the side channel of microfluidic T-junction by a syringe pump, while the gas phase is fed into the main channel which perpendicular to the liquid channel by a nitrogen cylinder. Microbubbles are formed as a result of the balance between the surface tension and viscous force. Inherently, the surface tension tends to minimize the surface area, which is important in the microbubble formation and for their stability. Viscous forces are to extend and stretch the surface tension.

For the case of liquid and gas, these two phases meet at the cross-sectional area of microfluidic T-junction, when the gas pressure of 3 kPa was applied (3kPa is smaller than the pressure provided by liquid flow rate of 100 µl/min), the liquid column starts forcing the gas backwards and liquid occupies all channels in microfluidic T-junction Figure 4-18 a).Hence no bubbles were formed under the minimum gas pressure To generate microbubbles the gas pressure has to be increased so that it penetrates the liquid column and microbubble formation begins (Maryam Parhizkar, Stride, & Edirisinghe, 2014). When the gas penetrates the liquid column, eventually the gas

column obstructed the channel and subsequently restricted the liquid phase (Figure 4-18 b1), b2) and b3)) This leads to an increase of hydrodynamic pressure in the microfluidic junction, which sequentially causes the pinch-off of the microbubbles (Figure 4-18 b4) and b5)). Monodispersed microbubbles were produced by repetitive pinch-off method in microfluidic T-junction (Figure 4-18 b6)). The pinch-off of microbubbles is dominated by the competition between shear forces to deform the gas-liquid interface and surface tension to resist the deformation. When gas pressure was increased to 100 kPa which is over the maximum gas pressure of 80 kPa, gas column overtakes liquid columns and occupied all channels (Figure 4-18 c)).

Consequently, at low liquid flow rates using the single T-junction, microbubbling occurs at relatively low gas pressures. On the contrary, at high liquid flow rates, high gas pressure is required to enable microbubble formation. However, the minimum gas pressure that enables microbubble production is always higher using the double T-junction than that of single T-junction even at the same liquid flow rate. This is most likely due to the fact that the additional liquid flow into the second junction causes the total flow rate of the liquid to increase; therefore, the ratio of liquid to air flow is increased. Subsequently, in order to start microbubbling, higher gas pressure is required for the double T-junction.

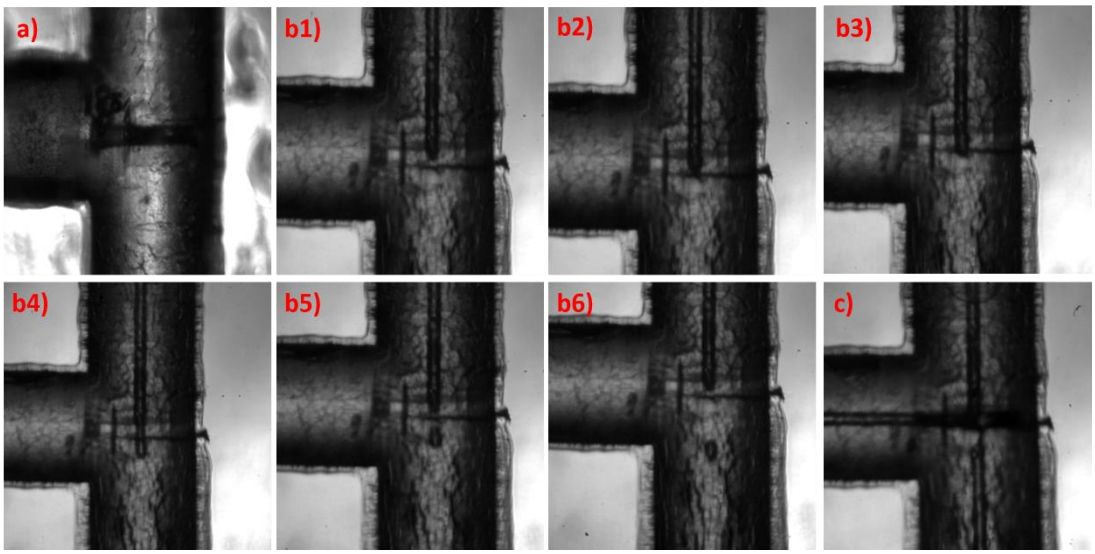

Figure 4-18: shows microbubble formation inside single T-junction geometry; a) the liquid column (pumped from the side channel into T-junction) forced gas column backwards (gas channel was perpendicular to the liquid channel). i.e. liquid phase was occupied the T-junction channels under liquid flow rate of 100 µl/min and gas pressure of 3 kPa; no microbubbles were formed. b1) gas column started to penetrate the liquid column when gas pressure increased from 3 kPa to 30 kPa; b2)-b6) microbubble formation began; c) gas column occupied the all T-junction channels when gas pressure was further increased to 100 Kpa. No microbubbles were formed.

As shown in Figure. 4-20, the largest microbubble was obtained from the single T-junction at the lower flow rate 100 µl/min and highest gas pressure, whilst the smallest microbubble was obtained using the double T-junction with higher flow rate (200µl/min) and lowest gas pressure. At a lower flow rate of 100 µl/min, the microbubbles generated using double T-junction had smaller dimensions than that formed by a single T-junction. Similarly, at the higher flow rate of 200 µl/min (Figure. 4-20), the size of microbubbles obtained was smaller in the double T-junction. For a fixed flow rate and gas pressure, double T-junction geometry provides microbubbles with smaller diameters. According to the scaling law from Garstecki et al., the length of the immiscible slug, L, is proportional to the flow rate ratio in a T-junction:$\frac{L}{d} = 1 + \alpha \frac{Q_g}{Q_l}$ where d is the width of the channel, Q_l and Q_g are the liquid and gas flow rates,

respectively, and α is a constant (Garstecki et al., 2006b). By calculating the capillary numbers *Ca*=0.002 and 0.003 (*Ca*<0.01) of the liquid phase at both flow rates of 100 and 200 µl/min, respectively, the breakup mechanism of microbubble formation in this work is found to be in the squeezing regime. The capillary number is defined as the magnitude of the viscous shear stress compared with the surface tension applying on gas-liquid interface (Christopher, Noharuddin, Taylor, & Anna, 2008).Therefore, microbubble diameter is dominated by the flow rate ratio $\frac{Q_g}{Q_l}$ (the pressure balance between liquid and gas phases) (Christopher et al., 2008). The reason for microbubble size reduction by double T-junction is that a new liquid and gas pressure balance was reached by adding extra liquid inlet through second T-junction. At the given liquid flow rate of 100 µl/min and gas pressure of 54 kPa, Microbubble size was observed to be smaller from the first T-junction out of the double T-junction (Figure 4-19 b)), compared to the bubble size formed from single T-junction under the same gas pressure of 54 kPa and liquid flow rate of 100 µl/min (Figure 4-19 a)). The bubble size generated from single T-junction inside microfluidic channel was 275 µm (Figure 4-19 a)) and the bubble size produced from first T-junction out of double T-junction inside microfluidic channel was 266 µm (Figure 4-19 b)). Both bubble formations were recorded by high-speed camera. The length of microbubble (labelled by red arrow in Figure 4-19) was used to indicate the microbubble size within the microfluidic channel and it was measured by Image J.

Since there is an additional liquid phase supplied to the second T-junction at a given flow rate (100µl/min) and constant gas pressure (45kPa), the total flow rate ratio of gas and liquid for double T-junction is no longer the same to the gas-liquid flow rate ratio for single T-junction.

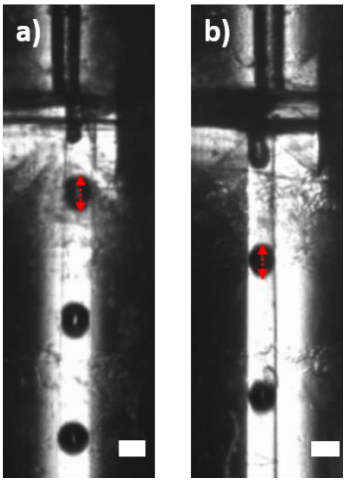

Figure 4-19: Bubble formation from a) single T-junction and b) the first T-junction out of double T-junction. The operation conditions were kept constant at gas pressure of 54 kPa and liquid flow rates at 100µl/min for both single and double T-junction. Scale bar are 200µm.The length of microbubbles within the channel (labelled by red error) was measured by Image J.

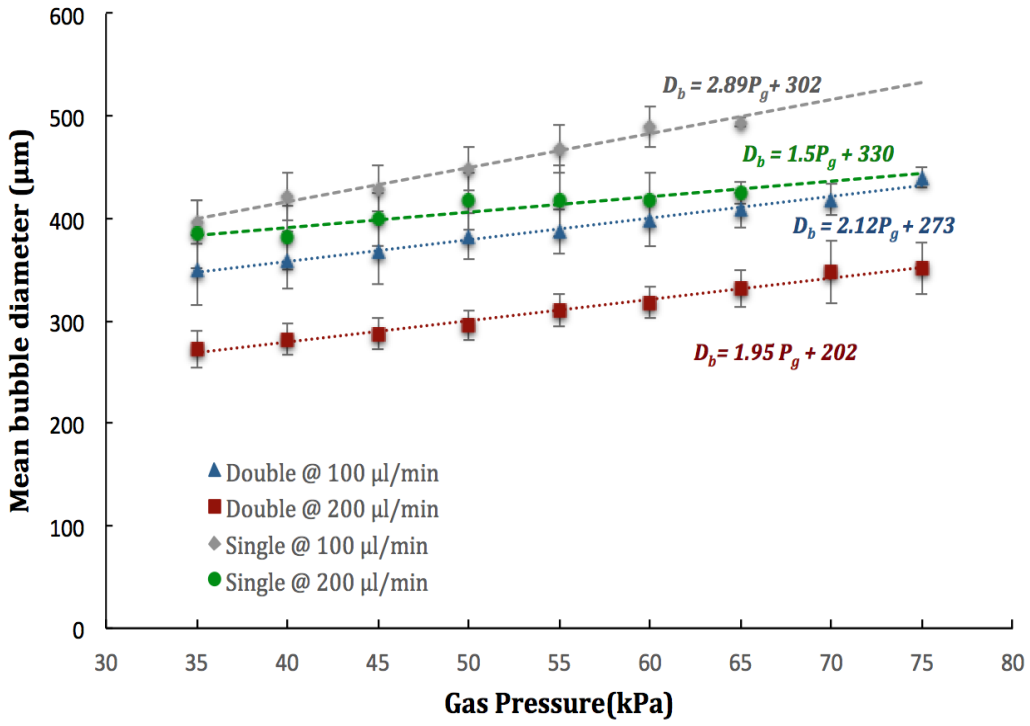

Figure. 4-20: Graphs demonstrating the range of microbubble diameters obtained at various gas pressures for liquid flow rates of 100 and 200 µl/min for both single and double T-junction geometries. (Db and Pg. are the diameter of bubble and gas pressure, respectively)

4.2.2.3 Effect of outlet tubing length on microbubble formation time

To study the effect of outlet tubing length on microbubble formation time, two configurations were assembled (Figure. 3-5 C) (i) and (ii)). Configuration (i) is the single T-junction with outlet tubing length of 110mm. Configuration (ii) is the single T-junction with outlet tubing of 200 mm. High speed camera was used to capture the microbubble formation and to record the bubble formation time inside the channel. Later, bubble travelling velocity can be calculated by the length of outlet tubing divide bubble residence time. Bubble residence time is the time measured within the outlet tubing from bubble formation to collection. Residence time will be discussed thoroughly in the following session 4.2.2.4.

The bubble formation time was counted from the gas column intruding the outlet channel and the reduction of the neck until the breakup of the formed microbubbles. The behaviour of the gas-liquid interface was recorded at constant liquid flow rate of 100 µl/min and gas pressure of 45 kPa. The gas pressure of 45 kPa chosen for this research was within the range of bubble production for BSA solution. Once the bubbles were generated, their diameter were measured under an optical microscope. Figure 4-21 demonstrates the high speed camera images showing the time evolution of formed bubble breakup from the gas column. From the footages obtained, it is clear that under the constant operation conditions, bubble formation times were both 4ms for single T-junction with 110 mm and with 200 mm outlet tubing length. The size of microbubble produced from single T-junction with outlet tubing length of 110 mm was 440 ±2 µm, and the bubble size produced by single T-junction with outlet tubing length of 200 mm was 429 ± 5 µm. Bubble travelling velocity within exit channel can be calculated by the channel length divided by the

bubble residence time within the channel. In this study, bubble travelling velocity for single T-junction with 110mm and 200mm outlet tubing length were 0.132 ± 0.03 m/s and 0.168 ± 0.04 m/s, respectively. It is shown that the length of outlet tubing does not affect the bubble size, formation time and its travelling velocity.

In microfluidic microbubble formation, microbubbles are formed by the formation and deformation of the gas-liquid interface between the two immiscible phases. Capillary number plays an important role in microbubble formation. Capillary number, representing the relative effect of viscous drag force versus surface tension acting across an interface between a liquid and a gas, can be calculated by the formula $Ca=\frac{\mu V}{\sigma}$, where μ is the dynamic viscosity of the liquid, V is a characteristic velocity and σ is the surface tension between the liquid and gas phases. In this work, dynamic viscosity μ was 0.0162 Pa.s; surface tension σ was 0.0504 N/m. The capillary number is used to determine which forces dominate in microbubble formation. Generally capillary number indicates microbubble size. For example, with an increase in capillary number, there is a smaller decrease in microbubble/droplet diameter (Maryam Parhizkar, 2014). To be more specific, long plug-like microbubbles/droplets are formed at low capillary number and spherical droplets/microbubbles are formed at the high capillary number. Capillary number for single T-junction with 110 mm outlet tubing length was 0.042 and the capillary number for single T-junction with 200 mm outlet tubing length was 0.054. It can be confirmed from Figure 4-21 that microbubbles formed under capillary number of 0.054 was more spherical shape (Figure 4-21 b)), compared to the bubble formed under capillary number of 0.042 (Figure 4-21 a)).

Reynolds number (Re=$\frac{\rho \vee D}{\mu}$), under liquid flow rate of 100 µl/min, is 0.6 which far smaller than 100. Due to the small dimensions of microchannels, the Reynolds number is normally smaller than 100 for microfluidics. The flow transition to turbulent flow normally takes place when Reynolds number is 2000. Thus, flow regime is completely laminar flow in this work.

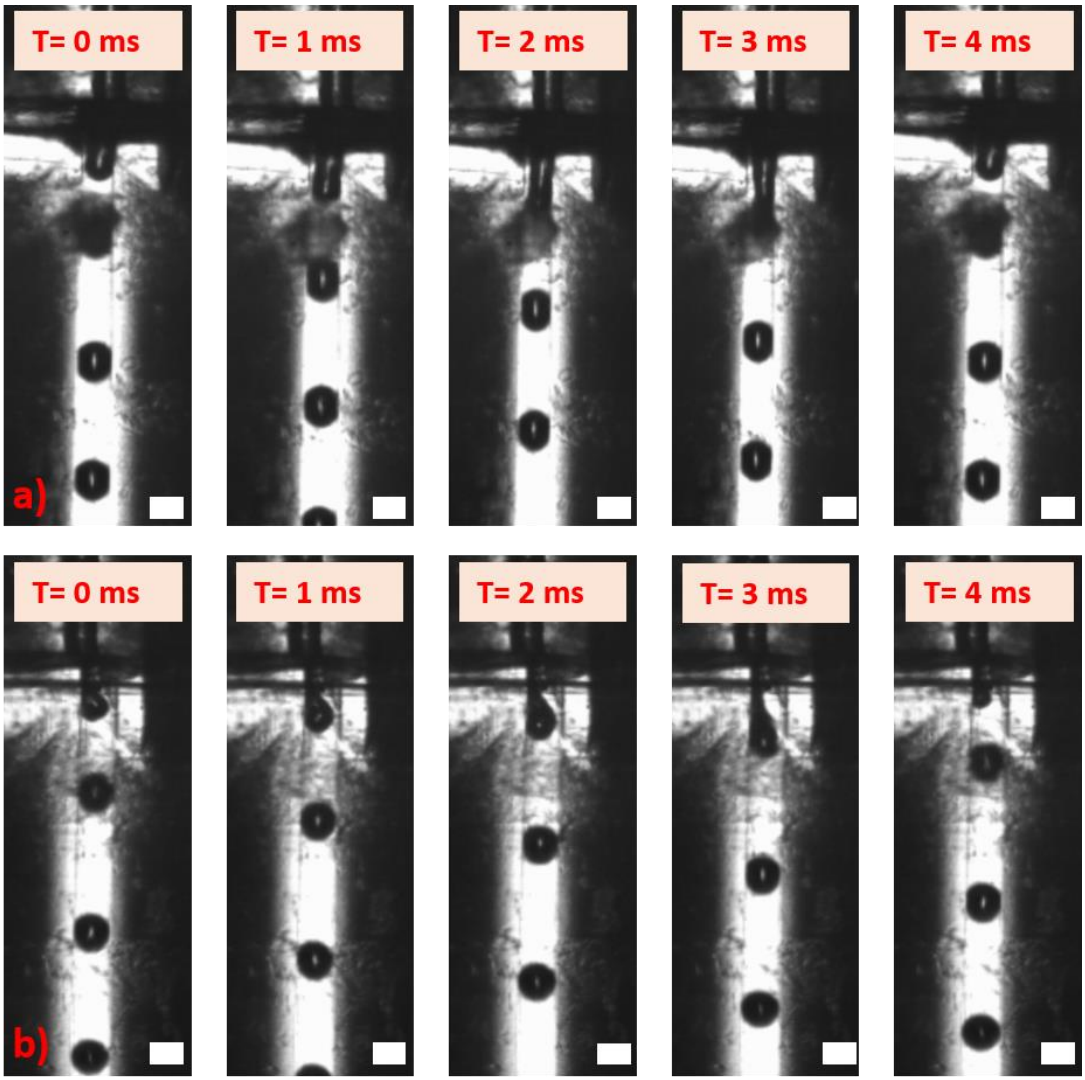

Figure 4-21: High speed camera footages of the microbubble formation time for a) bubble formation from single T-junction with outlet tubing length of 110mm. b) bubble formation from single T-junction with outlet tubing length of 200mm.Scale bar is 200 µm. Bubbles were formed for both configurations at liquid flow rate of 100 µl/min and gas pressure of 45 kPa.

4.2.2.4 Microbubble residence time within the channels and production rate

In this part of study, the microbubble residence time within the exit channel from formation to collection was measured using three different configurations shown in Figure. 3-5c. In order to verify the findings, microbubbles with different size and formation time were investigated by increasing the supplied gas pressure from 50 to 70 kPa at a constant flow rate of 100 µl/min. Microbubbles are formed at the orifice of the exit channel of the single T-junction and the first T-junction in case of double T-junction. Two different lengths were chosen for the single T-junction of 110 and 200 mm. From the measured data taken from high-speed camera images, plots of residence time are shown in Figure. 4-22. The residence time for shorter channel length was smaller (1.3 to 1.6 s). The graph of residence time for the single T-junction with 200 mm exit channel length has shown the highest values of 2.7 to 3.1 s. Microbubbles produced in the double T-junction had a smaller residence time than for the single T-junction with 200 mm exit channel length.

The microbubble production rate of the junction used in this study are given in Table 4-7**.** This data shows that for a fixed $\frac{Q_g}{Q_l}$ valve, the addition of a second T-junction was increasing production rates. Usually, microfluidic devices give lower microbubble production rates compared with jetting techniques such as co-axial electrohydrodynamic atomisation (Farook, Zhang, Edirisinghe, Stride, & Saffari, 2007; S Mahalingam, Meinders, & Edirisinghe, 2014). However, in the electrohydrodynamic jetting method the size distribution of the microbubbles generated is much wider and it is experimentally impossible to produce monodisperse microbubbles like in the

present work. Multi-array lithographic microfluidic devices can be effective in increasing microbubble production rates and the size of microbubbles generated (Farook et al., 2007; E Stride & Edirisinghe, 2008). However, lithographic technology is expensive compared to our new idea and device combing T-junction in series which also offer both increased production rates and reduction microbubble size. The production rates reported in this paper are lower than that values for T-junction microbubble production rates given in the review literature, however these also depend on capillary and microbubble size and flow rate (Epstein & Plesset, 1950).Microbubble production rate depends on operation parameters (gas pressure, liquid flow rate ratio), microfluidic channel size and solution material properties (S. Wang, Dhanaliwala, & Hossack, 2012). Previous studies have demonstrated that the bubble formation frequency depends on the flow conditions and gas-liquid flow rate ratio (Eleanor Stride & Edirisinghe, 2008). The higher the gas pressure/liquid flow rate ratio, the higher the microbubble production rate (Gañán-Calvo & Gordillo, 2001). Microbubbles production rate was 2 x10^7 microbubbles/min in the literature review However this production rate is only valid in a narrow range of gas-liquid flow rate ratio (E Stride & Edirisinghe, 2008). The production rate in this paper is lower than that in the literature review is due to the different application of solution material properties. A different gas-liquid flow rate ratio was adapted in this study to balance the variance of material surface tension and viscosity drag force. Thus, monodispersed microbubbles were produced under different gas-liquid flow rate ratio. Therefore, the production rate in this work is lower than the production rate in literature review.

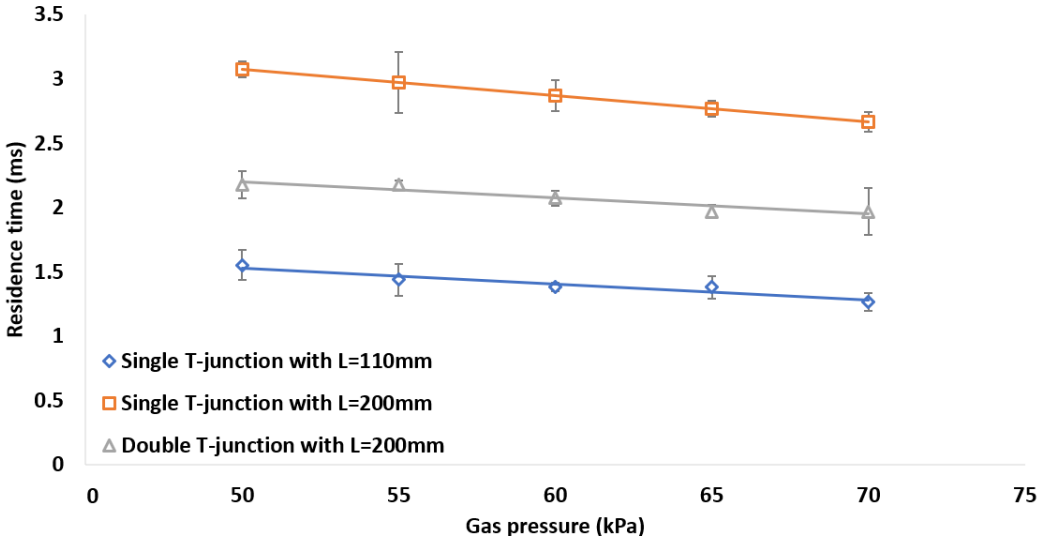

Figure. 4-22: Graphs representing residence time of microbubbles from formation to collection within the microchannels at different lengths of 110 and 200mm for constant liquid flow rate of 100 µl/min.

Q_g/Q_l	Single T-junction Production rate (microbubble/min)	Double T-junction production rate(microbubble/min)	% Increase
1.45	$1.697x10^4$	$2.787x10^4$	64
1.60	$1.971x10^4$	$2.790x10^4$	42
1.74	$2.039x10^4$	$2.923x10^4$	43
1.89	$2.112x10^4$	$3.001x10^4$	43
2.04	$2.242x10^4$	$3.750x10^4$	40

Table 4-7: The effect of gas-liquid flow rate ratio and number of T-junctions used on measured microbubble production rate at a constant liquid flow rate of 100 µl/min. The percentage increase in microbubble production due to second T-junction is also given.

4.2.2.5 Stability study of microbubbles generated with different geometries

The mean diameters of microbubbles generated at different gas pressures for a given flow rate and geometry were measured as a function of time. For each sample, 100 microbubbles were randomly selected and measured every 3 to 5 min until all the microbubbles disappeared or their BSA shell dried. As demonstrated in the micrographs in Figure.4-23, the least stable microbubbles were produced from the single T-junction with flow rate of 100 µl/min at 65 kPa and with flow rate of 200 µl/min at 80 kPa with mean diameter of 484 ±8.9 µm and 447 ±6.5 µm, respectively. On the other hand, microbubbles produced with liquid flow rate of 200 µl/min for both liquid phases at 35 kPa using double T-junction were found to be the most stable, with an average diameter of 272 ±5.2 µm, being stable up to 40 minutes after collection.

Microbubbles shrink with time due to gas dissolution to the surroundings, and those produced with smaller size were found to be more stable. This behaviour could be explained by the fact that microbubbles made of a solution with given viscosity have a constant surface tension which is responsible for cohesive forces among liquid molecules. For microbubbles with larger size, their gas-liquid interface is loosely packed and therefore gas dissolution is more likely to take place (J. L. Chen et al., 2014). Consequently, smaller microbubble whose gas-liquid interface is more densely packed were stable for a longer period.

The effect of liquid flow rate on microbubble stability was studied by comparative experiments. As shown in Figure. 4-24, microbubbles that were generated at higher liquid flow rates were found to be more stable than those generated at lower flow rates in both geometries. This is most likely to be due to the fact that microbubbles produced with higher liquid flow rate at the same gas pressure are smaller. Since the stability of microbubbles exposed to atmospheric conditions is dominated by their radius, smaller microbubbles have lower gas exchange rate with surroundings, hence they are more stable. On the other hand, the stability of the same size microbubbles generated at different flow rates and consequently different gas pressures were also studied. Microbubbles which were obtained from single T-junction with flow rate of 100 µl/min at gas pressure of 20 and 50 kPa have mean diameter of 315 ±3.9 and 405 ±5.5 µm, respectively. Microbubbles with mean diameter of 321 ±4.0 and 407 ±6.3 µm were obtained with higher liquid flow rate of 200 µl/min at higher gas pressures of 35 and 65 kPa, respectively. It was observed that both these microbubbles with similar diameter of 315 and 321µm (1.9% variation) lasted for 20 minutes after collection, and microbubbles with diameter of 405 and 407 µm (0.49% variation) were stable for 15 minutes. This behaviour of microbubble stability is consistent with previous findings (Suntharavathanan Mahalingam et al., 2015). Thus, we can assume that, the stability of microbubbles with same diameter generated via single T-junction is not significantly influenced by either flow rate or gas pressure.

More importantly, the influence of the microfluidic production geometry on microbubble stability was significant. As illustrated in Figure.4-23 and Figure. 4-24, for a given flow rate and gas pressure, microbubbles generated from double T-

junction were relatively more stable than that generated from the single T-junction. For instance, microbubbles generated from single T-junction lasted for 10 minutes, however, the microbubbles obtained from the double T-junction at 200 µl/min and 80 kPa lasted for 20 min. Also, microbubbles produced from the double T-junction have a steadier size decrease rate, whereas this is more rapid for microbubbles collected from the single T-junction. This could be attributed to size difference between microbubbles made form single and double T-junctions. As mentioned before, the addition of the second T-junction reduced the microbubble diameter, hence delivering improvement in the stability. Interestingly, for the same size microbubbles which were made from both single and double T-junctions at the same liquid flow rate, it was experimentally observed that the stability of the microbubbles generated from the double T-junction is higher. For instance, at liquid flow rate of 100 µl/min, microbubbles generated using the single T-junction at 20 kPa and double T-junction at 20 kPa have approximately similar size of 315 ±3.9 and 308 ±6.6 µm, respectively, and lasted for 20 and 25 min accordingly. Similarly, at higher flow rate, microbubbles (305 ±6.2 µm) obtained from the double T-junction lasted up to 30 minutes after collection, while microbubbles (300 ±3.8 µm) produced with the single T-junction were stable for only 20 minutes. This could be attributed to stabilization by the additional liquid phase formed at the second T-junction of double T-junction.

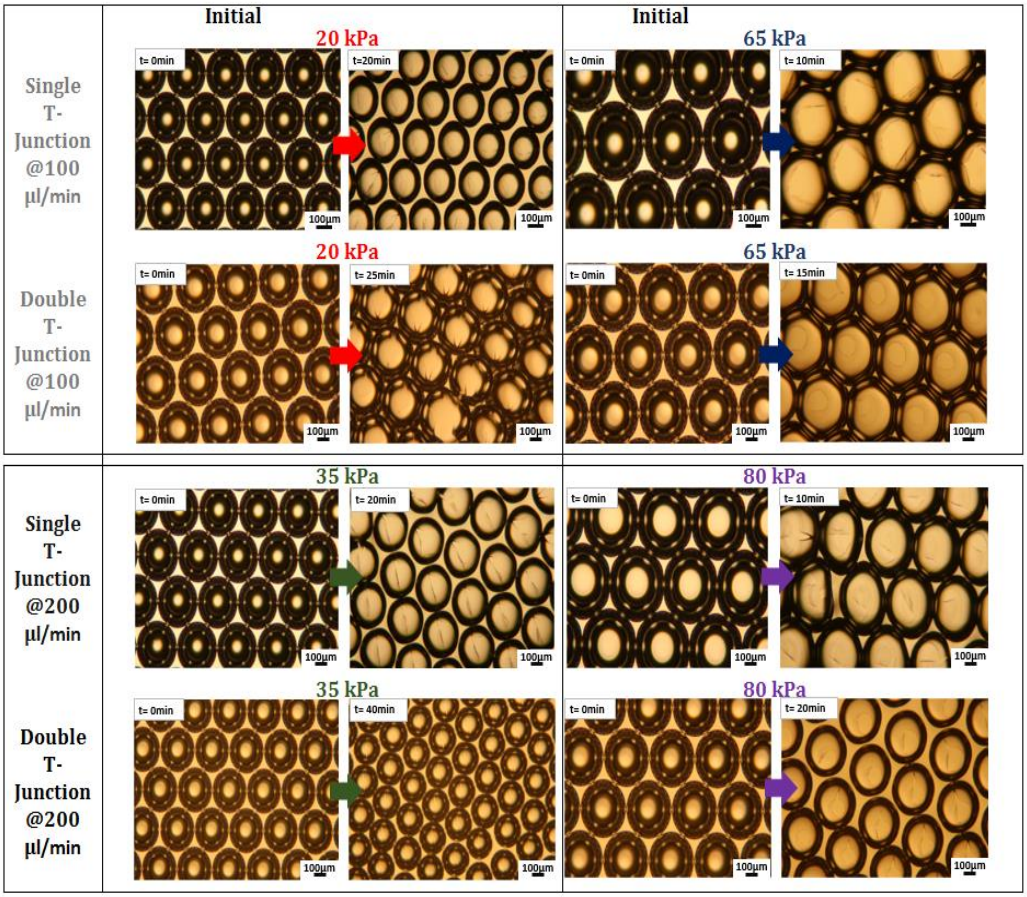

Figure.4-23: Micrographs showing the lifetime of microbubbles for both single and double T-junctions at both flow rates studied (100 and 200 µl/min) and various gas pressures.

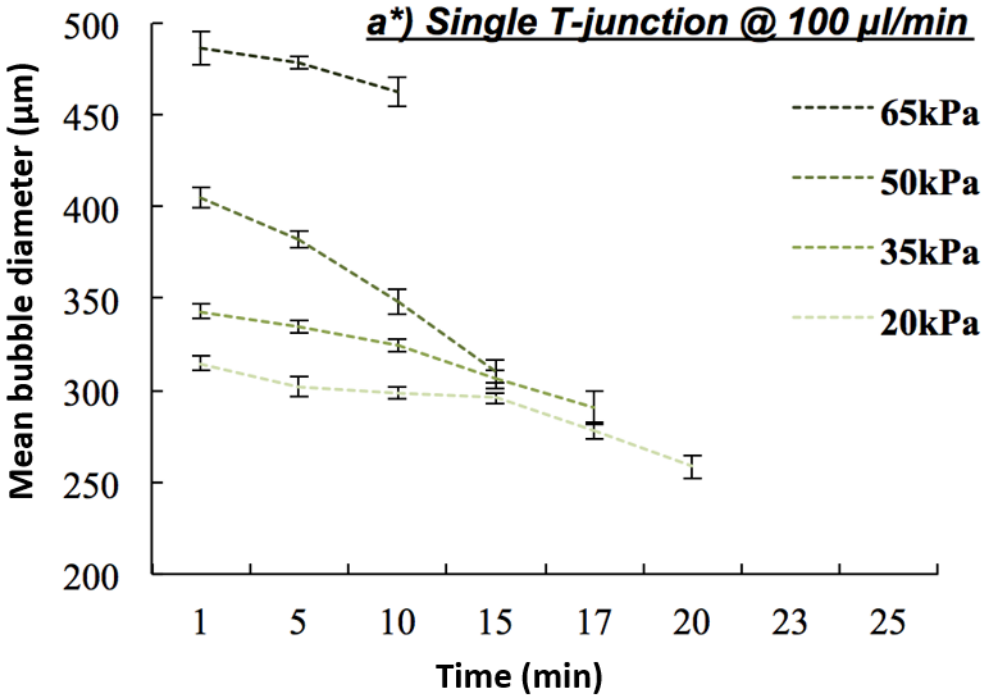
a*) Single T-junction @ 100 µl/min
Mean bubble diameter (µm)
500
450
400
350
300
250
200
1
5
10
15
17
20
23
25
Time (min)
65kPa
50kPa
35kPa
20kPa

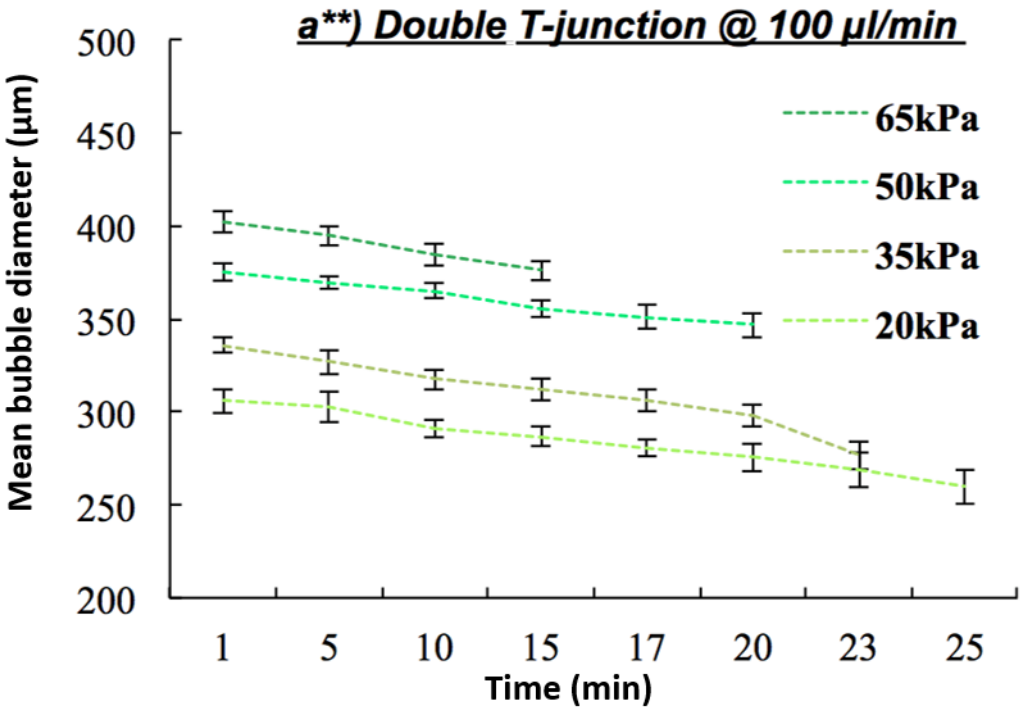
a**) Double T-junction @ 100 µl/min
Mean bubble diameter (µm)
500
450
400
350
300
250
200
1
5
10
15
17
20
23
25
Time (min)
65kPa
50kPa
35kPa
20kPa

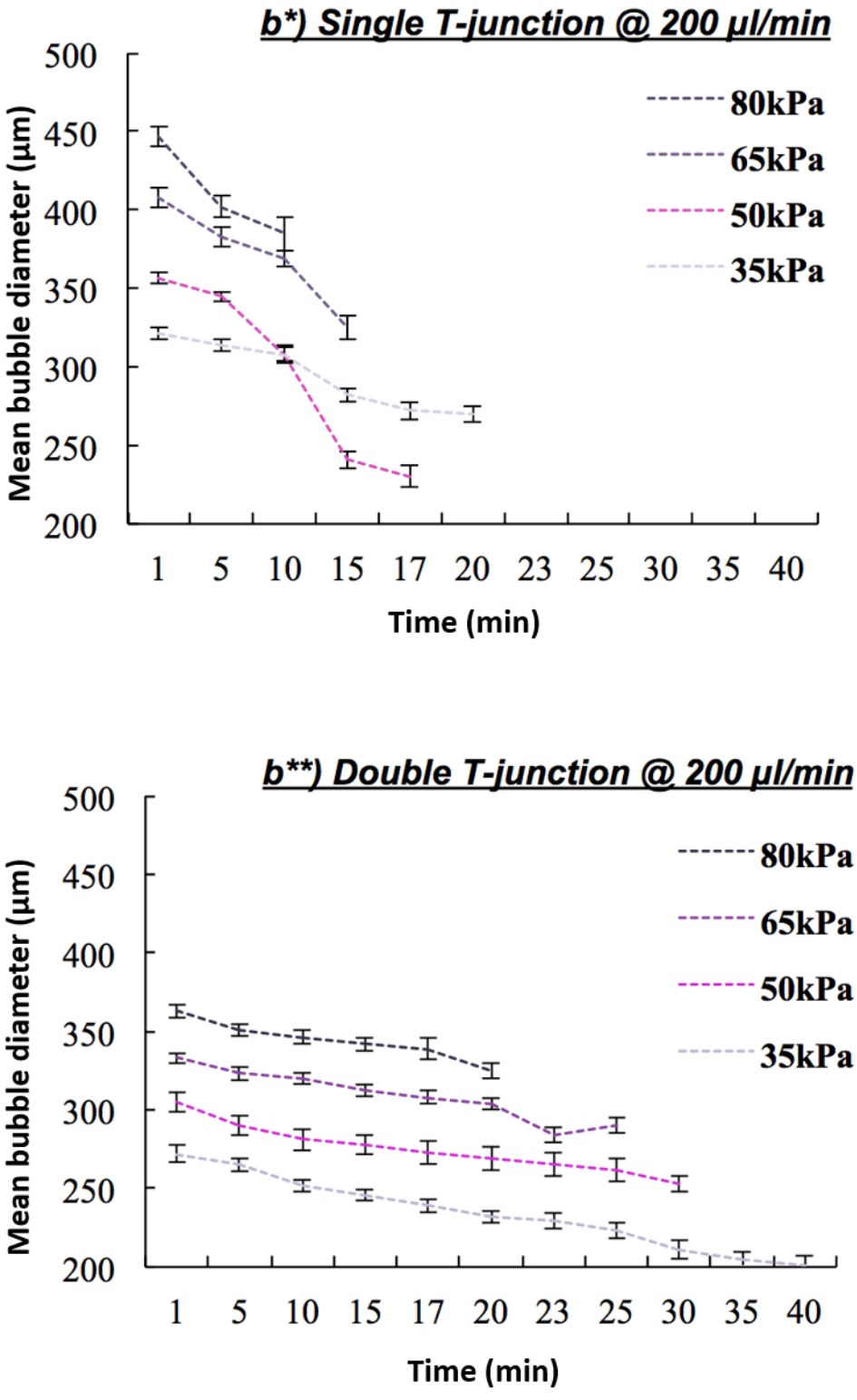

Figure. 4-24: Graphs showing the reduction of microbubble diameter with time (after collection) for microbubbles produced in a*) single T-junction, a) double T-junction at 100 µl/min and b*) single T-junction, b**) double T-junction at 200 µl/min.**

4.2.3 Verification experiments

4.2.3.1 Effect of flow rate and geometry on glycerol microbubble diameter

Figure. 4-27 describes that at a fixed flow rate and gas pressure, the diameter of BSA microbubbles generated by double T-junction was smaller than those from single T-junction. Then, there is a concern that whether the reduction of microbubble size is caused by the material property of BSA or the geometry of double T-junction. For the sake of solving this concern, experimental solution has been changed to 50% w/w glycerol mixed with 2% w/w polyoxyethylene 40 stearate instead of 15% w/w BSA. The effect of flow rate and geometry on the diameter of glycerol microbubbles have also been investigated by using single and double T-junctions. To conduct a consistent comparison experiments, the gas pressure was increased to 75 kPa with increment of 5 kPa.

Flow rate of 100 µl/min was chosen and used for both single and double T-junctions. The flow rate ratio and geometry decide the minimum gas pressure for microbubble formation. Then, the gas pressure increases systematically from the minimum gas pressure at flow rate of 100 µl/min for both single and double T-junctions experiments. Both experiments have been repeated three times which show in Figure. 4-25 and Figure. 4-26. for the relationship between microbubbles diameter and single and double T-junctions, respectively. As demonstrated in Figure. 4-27, the largest microbubble size (315 µm) was produced from the single T-junction at fixed liquid flow rate of 100 µl/min and at the highest gas pressure of 75kPa. At the same liquid flow rate, the smallest microbubbles size (220 µm) was generated at the lowest gas pressure of 45 kPa by double T-junction. Moreover, microbubbles generated from

double T-junction were around 18% smaller than those from single T-junction. This trend of the variance of microbubble diameter is the same with that of BSA microbubbles obtained from single and double T-junctions according to the same process gas-liquid parameter conditions (Figure. 4-28). As a result, the reduction of diameter of microbubbles is relevant to the geometry of double T-junctions other than the property of BSA solution.

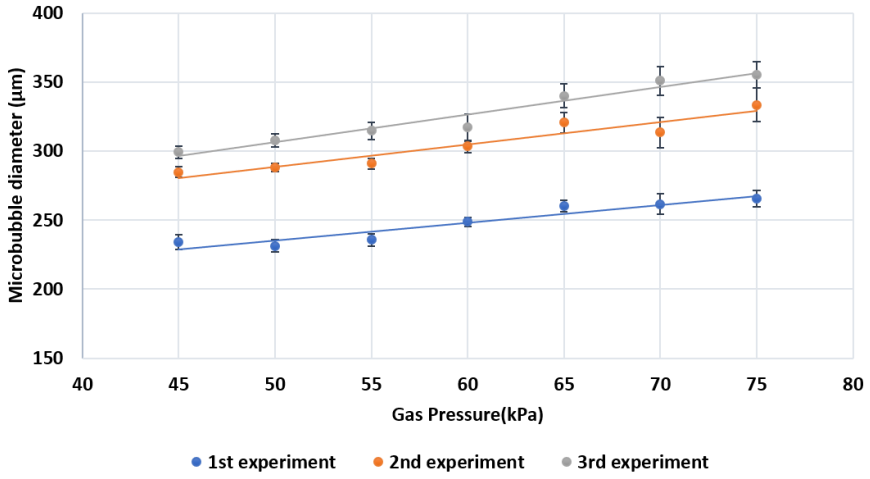

Figure. 4-25: The range of microbubble diameters produced by single T-junction at various gas pressures for liquid flow rate of 100 µl/min. Experiments repeated three times.

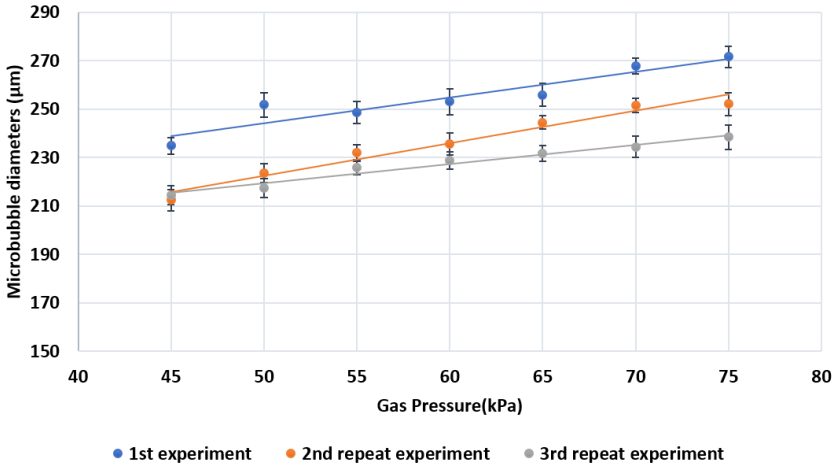

Figure. 4-26: The range of microbubbles diameters generated by double T-junction at different gas pressure for given liquid flow rate of 100 µl/min.

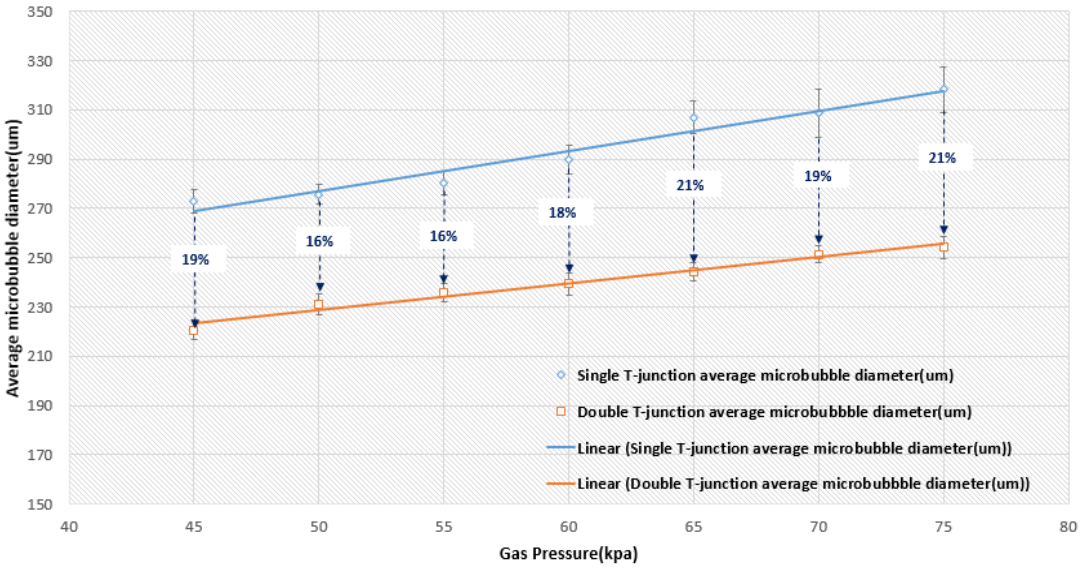

Figure. 4-27: The range of average microbubble diameters obtained by single and double T-junction microfluidic devices at various gas pressure at liquid flow rate of 100 µl/min. 1T, 2T represents single and double T-junction respectively.

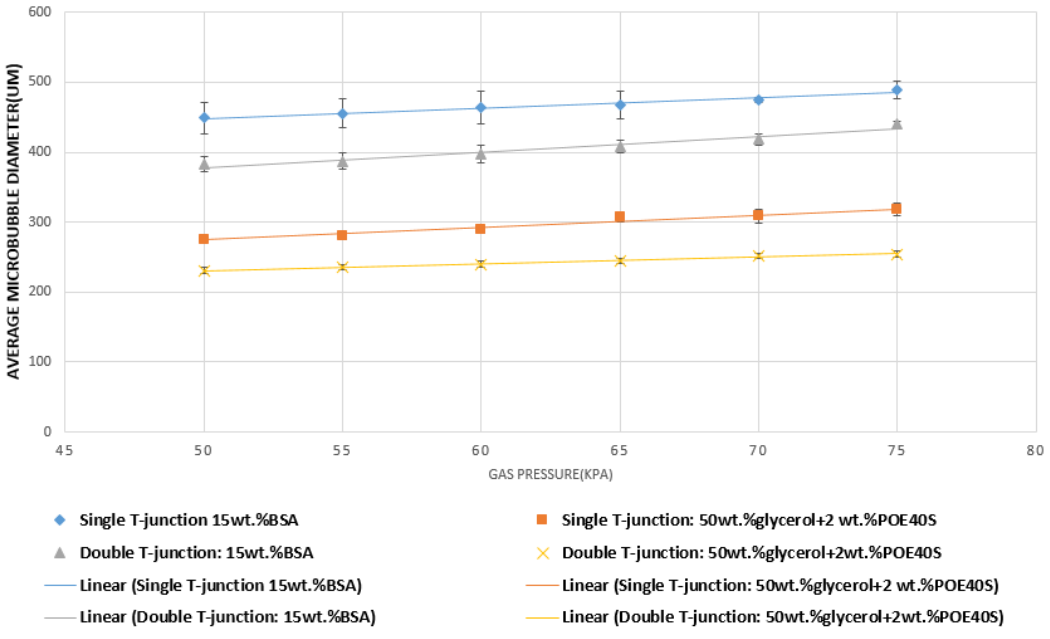

Figure. 4-28: The trend of microbubbles size generated from single and double T-junctions by different materials for various gas pressure at fixed liquid flow rate of 100 µl/min.

4.2.3.2 Effect of triple T-junction on the formation of microbubbles

To study the triple T-junction on the microbubble formation, flow rate of 100 µl/min was selected and employed to all the single, double and triple T-junctions. 15% w/w BSA was chosen to use as polymeric solution for single, double and triple T-junction experiments. The microbubble generation process for triple T-junction is the same with that of single and double T-junctions. Once the microbubbles were generated at the minimum gas pressure at a certain given liquid flow rate, the gas pressure was systematically increased. The minimum gas pressure for microbubble formation by triple T-junction was 50 kPa at the liquid flow rate 100 µl/min. The minimum gas pressure was 15 kPa and 20 kPa for single and double T-junction respectively for the formation of microbubbles at the liquid flow rate 100 µl/min. As a result, at the same liquid flow rate, the minimum gas pressure of microbubble formation is increased with the number of T-junction combined due to the increase of liquid amount fed into the microfluidic system. In microfluidic device, the microbubble formation is based on the liquid-gas pressure balance (Castro-Hernández et al., 2011). To form microbubbles by microfluidic devices, minimum gas pressure is enhanced along with the increase of liquid pressure. Triple T-junction experiments were repeated three times with gas pressure increment of 5 kPa until 75 kPa (results shown in Figure. 4-29). From Figure. 4-30, it has shown that the average diameters of microbubbles generated from triple T-junction were smaller than those from single and double T-junctions. Furthermore, this graph also illustrates that the diameter of microbubbles produced by triple T-junction can also be tuned by gas-liquid flow rate ratio, which is the same with that from single and double T-junctions. For instance, in Figure. 4-30,

diameters of microbubbles went up with the increase of supplied gas pressure for the fixed liquid flow rate of 100 µl/min.

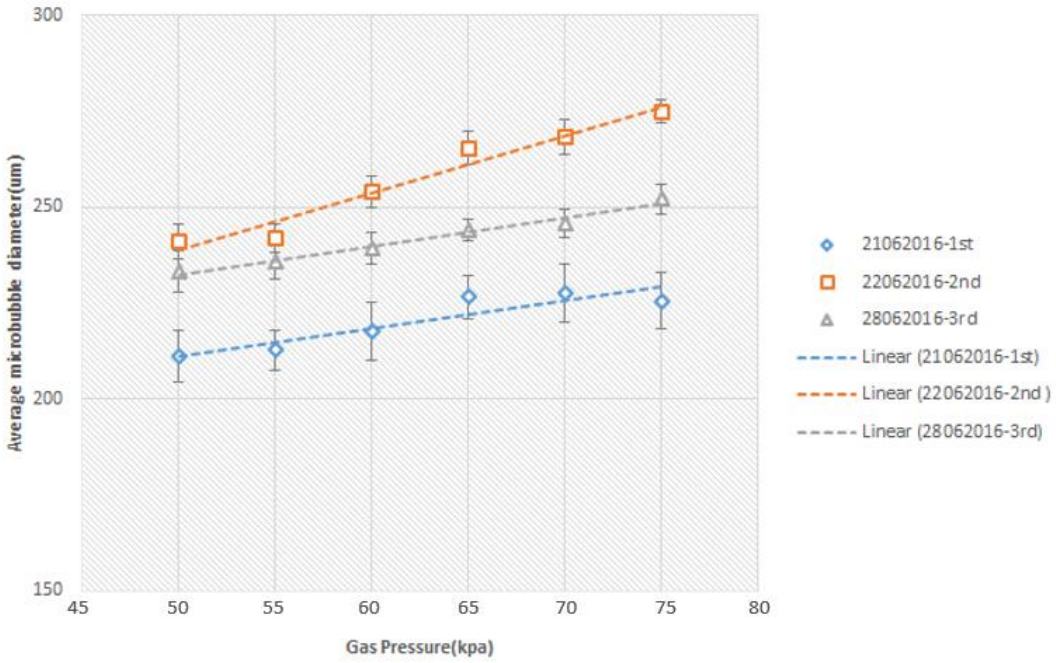

Figure. 4-29: Plot illustrating the range of the diameters of microbubbles generated at various gas pressure at liquid flow rate of 100 µl/min for triple T-junction configuration.

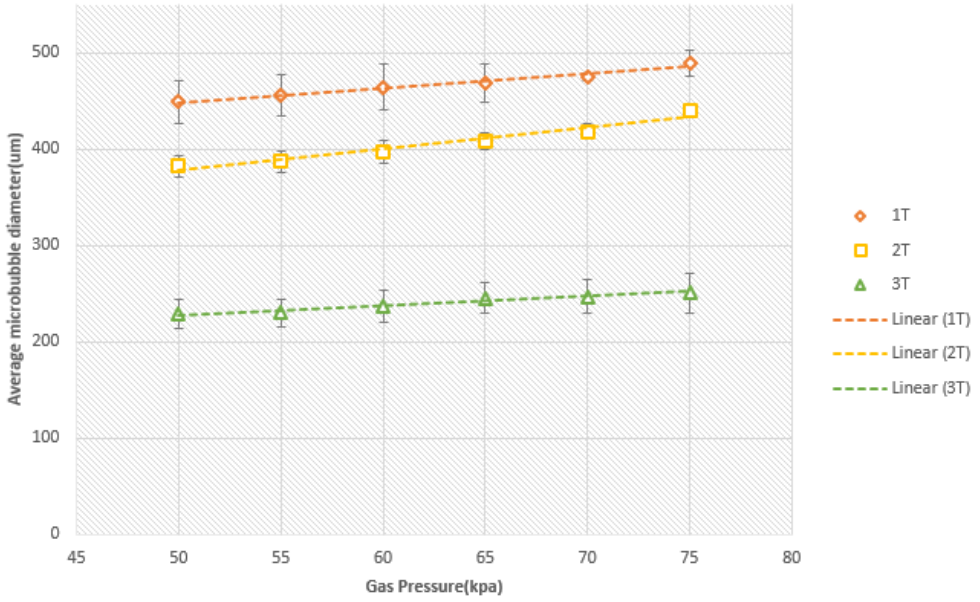

Figure. 4-30: Average diameters of microbubbles obtained at single, double and triple T-junction.

4.2.4 Double layered microbubbles produced by double T-junction

In this work, double T-junction device was introduced to study the potential for generating double layered microbubbles. Double layered microbubble is one types of double emulsion, which viewed as systems consisting of at least two immiscible liquids (Garti & Bisperink, 1998). According to the definition of double emulsions, two immiscible materials were selected as inner layer and outer layer of microbubbles, separately. 15% w/w BSA as water phase material was chosen to feed into the first T-junction, which acted as microbubble inner layer, later, 50 mPa.s pure silicone oil as oil phase was supplied to the second T-junction to form a protective oil phase outer layer of microbubbles. To produce double layered microbubbles, varies combinations of liquid flow rate ratios and gas pressure were selected to test the potential of generating double layered microbubbles by double T-junction. Two sets of experiments were conducted. They were conducted at fix inner layer liquid flow rate at 50 µl/min and 55 µl/min for BSA separately, meanwhile, increasing silicone outer layer liquid flow rate (Table 4-8).

Liquid flow rate of BSA/silicone (uL/min)	The amount of single layer percentage (%)	The amount of double layer percentage (%)
50/40	6	94
50/50	27	73
50/55	23	76
50/60	50	50
50/65	37	63
50/100	44	56
50/150	79	21
55/25	20	80
55/85	4	96
55/90	14	86
55/95	9	91
55/100	5	95
55/110	8	92

Table 4-8: The percentage of the amount of single layered and double layered microbubble under different liquid flow rate combinations through double T-junction.

According to Table 4-8, 400 microbubbles were counted under each liquid flow rate combination. The best combinations have been highlighted, to figure out suitable liquid flow rate ratio to produce double layered microbubbles by double T-junction. Amongst the three-highlighted liquid flow rate combinations, 94% out of 400 microbubbles double layered microbubbles can be obtain at liquid flow rate of BSA and silicone at 50 µl/min and 40 µl/min, which reason can be explained as the lower liquid flow rate (40 µl/min) of silicone oil as outer layer has relatively smaller shear force to avoid rupture of the inner microbubbles. When increasing BSA inner layer liquid flow rate from 50 µl/min to 55 µl/min, the average percentage of the amount of double layered microbubbles enhanced from 62% to 90% out of 400 microbubbles, which can be shown vividly from Figure.4-31. This result can be exploited as high liquid flow rate produced high shear force for primary gas-liquid emulsion, which leads to more stable and smaller size microbubbles generated from first T-junction.

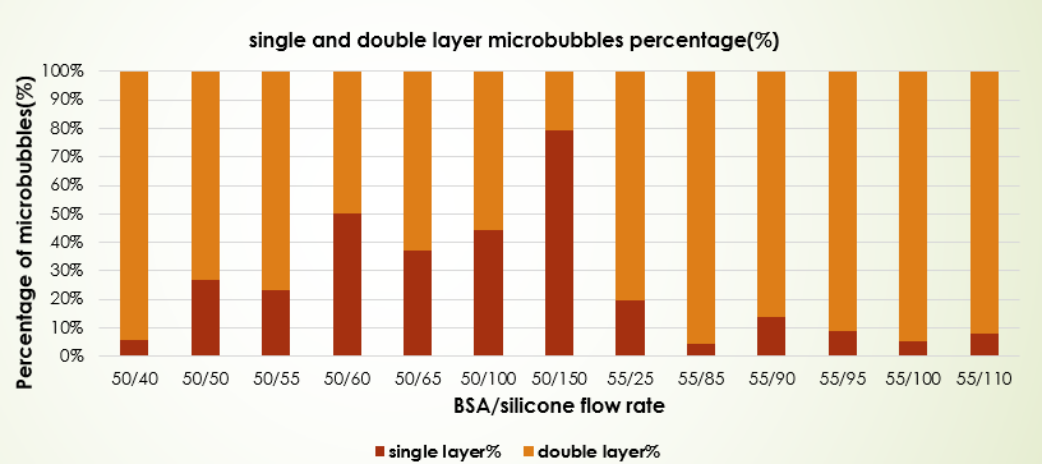

Figure.4-31: The percentage of the amount of single layered and double layered microbubble under different liquid flow rate combinations through double T-junction.

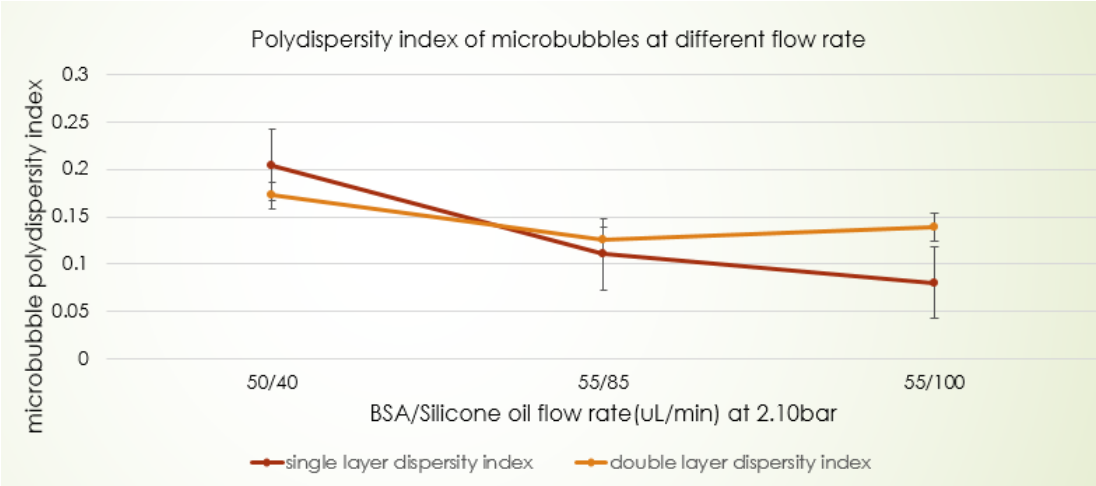

Figure. 4-32: Polydispersity index of single layered and double layered microbubbles under varies liquid flow rate ratio for fixed gas pressure of 210kpa.

To find the best process parameter conditions for double layered monodispersed microbubbles, the polydispersity of double layered microbubbles was investigated under the three-highlighted liquid flow rate ratio (Figure. 4-32). Figure. 4-32 illustrates at the BSA and silicone liquid flow rate at 55 µl/min and 85 µl/min respectively, double layered microbubbles were more monodispersed produced by double T-junction (Figure 4-33), which polydispersity of 0.13 was lower than the other liquid flow rate combinations (Table 4-9). The polydispersity of inner single layered microbubbles and double layered microbubbles have been shown in Table 4-9.

BSA/silicone flow rate(uL/min)	single layer polydispersity index	double layer polydispersity index
50/40	0.204582	0.17232
55/85	0.110129	0.124935
55/100	0.080086	0.138894

Table 4-9: Polydispersity index of single layered and double layered microbubbles under varies liquid flow rate ratio for fixed gas pressure of 210kpa.

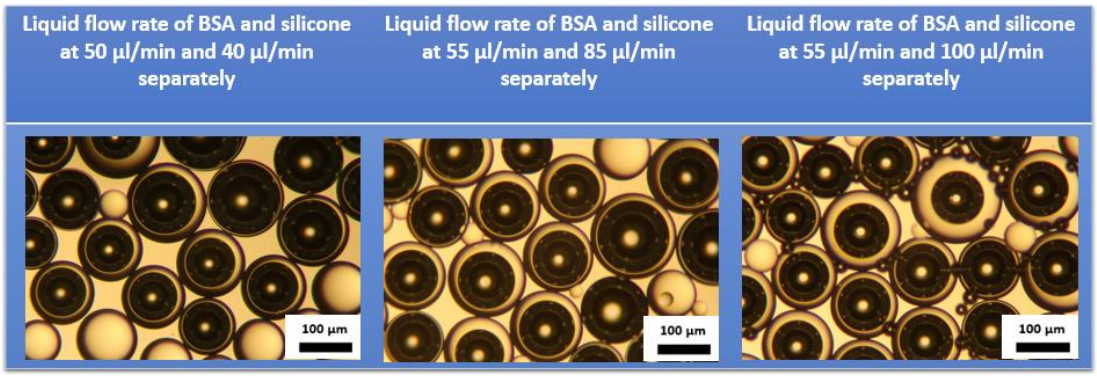

Figure 4-33: double layered microbubbles produced by double T-junction under highlighted liquid flow rate ratio in table 3.

4.2.5 Summary

In this work, a new double T-junction device was tested to investigate the potential for producing microbubbles. It was shown that the size and production of microbubbles could be manipulated by introduction of a second junction into the commonly used single T-junction device. A comparison study was conducted to produce BSA microbubbles both with a single T-junction and then a double T-junction. The microbubbles produced via the double T-junction were different in size and stability for a given flow rate and gas pressure. It was shown that for the highest liquid flow rate (200 µl/min) at the lowest gas pressure (35kPa), microbubbles generated were smaller (272 ±5.2 µm) in the double T-junction. This can be described by the diffusion of gas into the liquid phase due to a longer residence time inside the microchannels, compared to a single T-junction system. While the diffusion of gas takes place, the velocity of the mixed flow is increased by the additional liquid flow rate through the second T-junction and therefore the production rate is not compromised by keeping the microbubbles in microchannels by increasing the length of the single T-junction exit channel length. Furthermore, it is shown that the stability

of microbubbles was improved by inserting the second T-junction. Two verification experiments have been conducted to further investigate the characteristics of double T-junction. According to the verification experiment, the variance of glycerol microbubble size was the same with the size trend line of BSA microbubbles obtained from both single and double T-junctions, which exploits that the reduction of microbubble size is more relevant to the geometry of double T-junction instead of the material property of BSA. Moreover, under the same flow rates of 100 µl/min for all single, double and triple T-junctions, the minimum gas pressure of bubble formation was increased with the number of T-junctions. Microbubble size produced by triple T-junction was similar with the microfluidic channel size which is around 200 µm under gas pressure of 75 kPa. In addition, it has been shown that double layered microbubbles can be produced by double T-junction. To get monodispersed double layered microbubbles, more materials and process parameter combinations need to be investigated in the future. Good encapsulation results were produced from similar densities of liquid and oil phases. Furthermore, the flow rate ratio of liquid and oil phases was proportional to the viscosity ratio of liquid and oil phases in this work. Material properties and gas-liquid flow rate ratio play a vital role in the formation of double layered microbubbles. In the future, a systematically research can be done to study the effect of anionic, nonionic and cationic surfactant on BSA surface tension. Different surfactant types can be added into BSA solution to alter the material surface tension. In order to better study the encapsulation formation mechanics, both hydrophilic and hydrophobic dyes can added into experimental liquid and oil phases and the formation can be recorded by high speed camera.

4.3 Triple T-junction and bubble fission regime

4.3.1 Overview of triple T-junction microfluidic device processing

To further bring down the size of microbubbles, a triple T-junction device was assembled after connecting an additional T-junction block with the outlet channel of the double T-junction with a coarse capillary of 200 μm internal diameter. In section 4.2.3.2 , Figure. 4-30 shows that the size of microbubbles can be reduced by using a triple T-junction microfluidic device, when gas pressure was lower than 75 kPa with a constant liquid flow rate of 100 μl/min. Moreover, the size of microbubbles can be further reduced by microbubble fission, when increasing the gas pressure over 75 kPa. The microbubble fission regime here refers to the mother bubble splitting into a number of daughter bubbles as the mother bubble crosses the third T-junction. The bubbles produced from the outlet of the double T-junction is named as the mother bubbles. The resultant bubbles after the fission of mother bubbles inside the outlet channel of triple T-junction are called daughter bubbles in this work. Hence, this chapter focuses on the investigation of fission regimes inside a triple T-junction microfluidic device.

Systematic research has been conducted on the effect of the operating parameters (gas pressure, liquid flow rate and gap size) on the fission of microbubbles. The relationship between capillary numbers and microbubble fission has been studied. The critical capillary number has been found which will indicate the onset of the bubble fission regime. The effect of gas pressure, gap size and resultant capillary number on microbubble fission is presented in section 4.3.2. The influence of liquid flow rate, gap size and resultant capillary number on microbubble fission is shown in

section 4.3.3. The correlation between bubble formation mechanism and gap size is demonstrated in section 4.3.4. The feasibility of a triple T-junction device to split microbubbles has been illustrated in section 4.3.5.

4.3.2 Effect of gas inlet pressure, gap size on microbubble splitting

In this experiment, control variable method was adopted to investigate the effect of gas pressure on the microbubble fission regime. Hence, liquid flow rate was held constant at 100μL/min for all the three liquid inlet channels, gas pressure was adjusted from 177 to 300Kpa under a fixed gap size of 200 μm (results in Figure 4-34). Subsequently, in order to study the effect of gap size under given liquid flow rates on bubble fission regime, the gap size of the third T-junction was altered to 200 μm, 150 μm and 100 μm (results in Figure 4-35). The size of the mother bubbles was only measured under high speed camera footage and the size of daughter bubbles were measured by high speed camera and microscope.

4.3.2.1 Effect of gas pressure on the microbubble fission regime

In Figure 4-34, the microbubble fission regime occurred with the increase of gas pressure from 177 kPa to 300 kPa, whilst the size of the mother bubbles increased from 280 μm to 315 μm respectively. The size of daughter bubbles was reduced from 216 μm to 136 μm when measured under optical microscope (under ambient pressure), whilst the size of the same daughter bubbles (measured from high speed camera footage) was reduced from 113 μm to 58 μm inside channel. Daughter bubble diameter was larger when measured by optical microscope than from high speed camera footage (Figure 4-35 a)). This is due to ambient pressure being lower than the channel pressure resulting in daughter bubble expansion under ambient pressure

after leaving the channel. For example, for a mother bubble size at 280 µm diameter split into 2 daughter bubbles, the daughter bubble size at ambient pressure is 216 µm and in high speed camera is 113 µm.

In Figure 4-35 a), along with the increase of system pressure, the diameter of mother bubbles increased. The number of daughter bubbles was increased, and the size of daughter bubbles was reduced. This is due to the classical Rayleigh-Plateau instability. When the bubble slug length exceeds its circumference, a cylindrical liquid or gas thread can minimize its total surface area by breaking. Thus a larger bubble size generated at high pressure tends to break more easily compared to a smaller bubble size (Link, Anna, Weitz, & Stone, 2004). It has been shown in Figure 4-34 that the number of daughter bubbles increased from 2 to 5 along with gas pressure adjusted from 177kPa to 300kPa. The size of the daughter bubbles was reduced because of the increase in the split number. It is due to the total sum of daughter bubbles size is proportional to the size of mother bubble. For a specified mother bubble size, the size of the daughter bubbles is reduced with an increase in the bubble split number.

In microfluidic devices, surface tension and viscous force are important, inertial forces are typically ignored (Brody, Yager, Goldstein, & Austin, 1996; Thorsen et al., 2001; Zabow et al., 2002). In fluid dynamics, capillary number (Ca) is used to represent the relative effect of viscous drag forces versus surface tension forces acting across an interface between a liquid and a gas, or between two immiscible liquids (Shi, Zhang, Liu, Hanaor, & Gan, 2018). The formation of microbubbles and droplets is dominated by the competition between surface tension and shear forces

(Johnson, Kendall, & Roberts, 1971; Thorsen et al., 2001). Importantly, microbubbles or droplets split when the viscous force exerted by the continuous phase produces a critical asymmetric stress on the microbubbles or droplets which causing an imbalance of the surface tension (Briscoe, Lawrence, & Mietus, 1999; Y. Tan, Fisher, Lee, Cristini, & Lee, 2004). Therefore, the reason bubble fission phenomena only occurred at the third T-junction can be explained by the capillary number. Capillary number can be written as(Jiang, Zhang, Edirisinghe, & Parhizkar, 2016):

Equation 6

$$Ca = \frac{\eta v}{\Upsilon}$$

Where η is the viscosity of the continuous phase, v is the velocity of the bubble inside channels, and Υ is the interfacial tension between nitrogen gas and BSA liquid phase. Dynamic viscosity and surface tension are constants of the solution, therefore capillary number only depends upon bubble travelling velocity v inside microchannel. A high speed camera was used to measure the bubble travelling distance and its residence time inside the channel. Then, the capillary number of mother and daughter bubbles was calculated using bubble travelling velocities in the inlet and outlet capillaries of the third T-junction respectively.

The critical capillary number is the index of breaking and nonbreaking bubbles(Briscoe et al., 1999; Link et al., 2004).It can be calculated as(Briscoe et al., 1999; Link et al., 2004; Y. Tan et al., 2004)

Equation 7

$$Ca_{crit} = \frac{Cav}{w}$$

Where, v is the velocity of bubbles inside channel and w is the channel width. Critical capillary number varies depends on different solution properties from Equation 6 and Equation 7. In the first experiment, the capillary number of mother bubbles in the upper channel is between 0.009 and 0.019 from 177kPa to 300kPa respectively. Ca of daughter bubbles in the lower channel is between 0.018 and 0.030 from 177kPa to 300kPa respectively. The increase in capillary number across the T-junction gap is greater than the critical capillary number for BSA which indicates why mother bubbles start to split at a gas pressure of 177 kPa in this work.

Figure 4-35 b) demonstrates the relationship between capillary number and the size of mother and daughter bubbles. It shows that smaller daughter bubbles can be produced by increasing the capillary numbers. Larger mother bubbles were also generated by increasing the capillary numbers. As capillary number increased, mother bubbles split into more, smaller daughter bubbles. Hence, the intrinsic reason bubble fission regime occurred by changing the gas pressure is due to the change of capillary number. Capillary number is in positive correlation to the gas pressure. i.e. Capillary number increases with the elevation of gas pressure (Table 4-10). Additionally, the splitting number of microbubbles is increased with the increment of capillary number. Size of microbubbles is in negative correlation to capillary number.

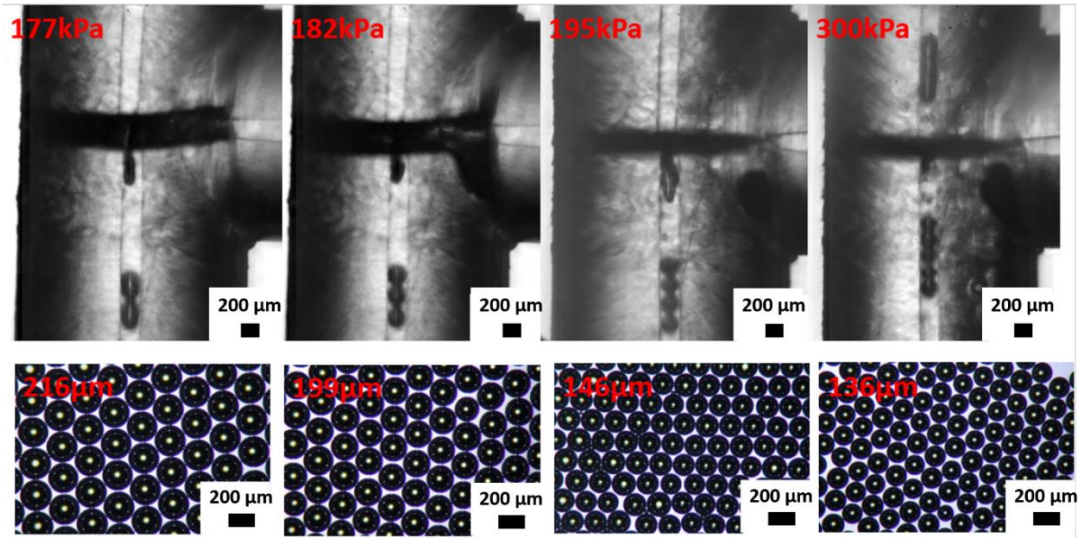

Figure 4-34: High speed camera images and micrographs showing the number of split microbubbles and the relevant range of microbubbles diameters collected at various gas pressure from 177kPa to 300kPa for all liquid flow rate fixed at 100µl/min at the third T-junction of triple T-junction geometry. Then, gas pressures of 177,182, 195 and 300kPa. The relevant diameter of microbubbles is 216,199,146 and 136µm, respectively.

Gas pressure / Capillary number	177 kPa	182 kPa	195 kPa	300 kPa
Ca_{mother}	0.009±0.003	0.010±0.003	0.014±0.0012	0.019±0.001
$Ca_{daughter}$	0.018±0.003	0.021±0.002	0.023±0.002	0.030±0.001

Table 4-10: the relation between gas pressure and capillary number of mother and daughter microbubbles. Gas pressure is in a positive correlation to capillary number at the given flow rates of 100 µl/min and gap size of 200 µm.

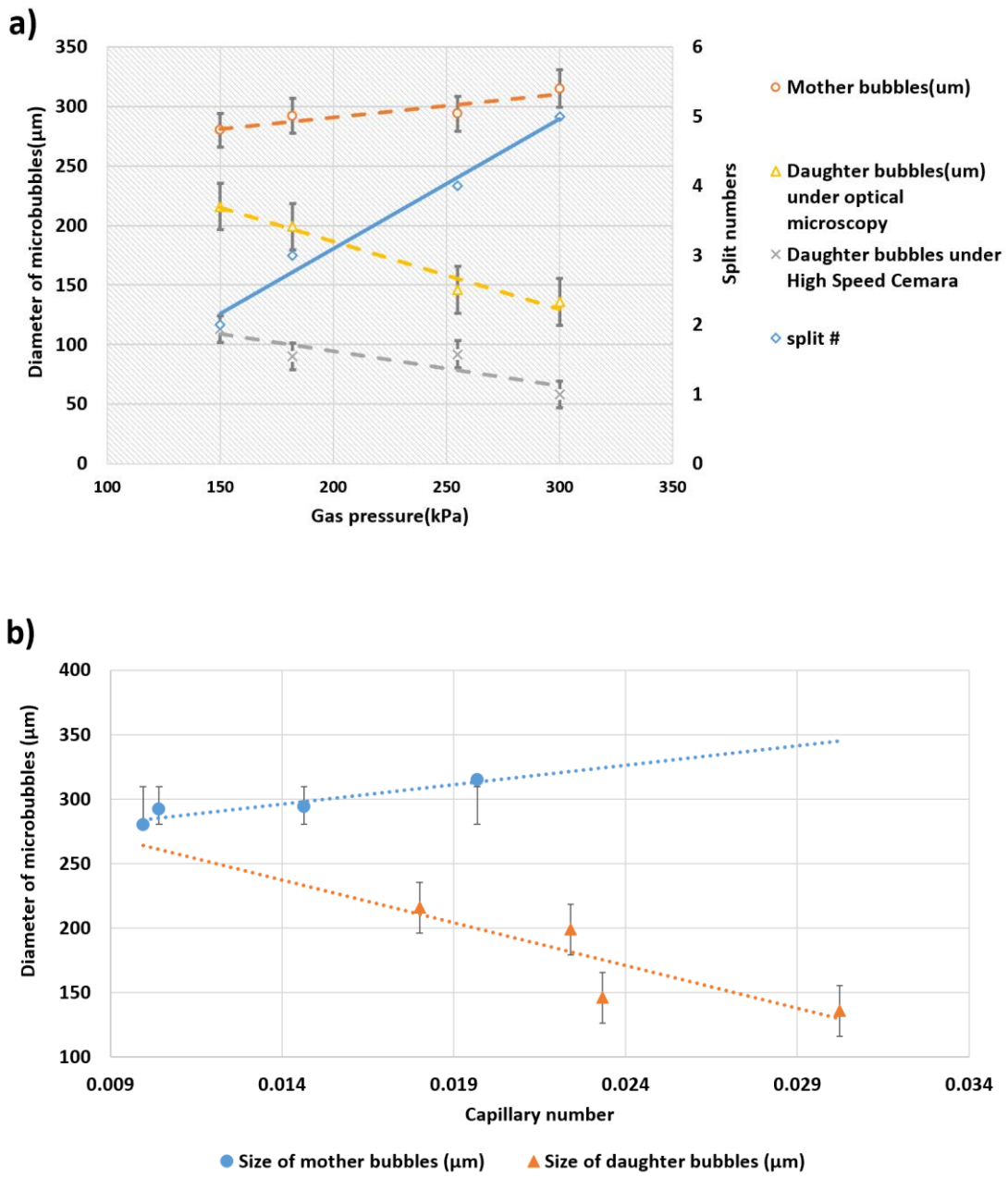

Figure 4-35: This graph reveals: When liquid flow rates are fixed at 100 µl/min and gas pressure was increased from 177kPa to 300kPa under gap size of 200 µm, a) The size variation between mother and daughter bubbles; b) the relation of capillary number between mother bubbles (Ca mother) and daughter bubbles (Ca daughter).

4.3.2.2 Effect of gap size under given flow rate on bubble fission regime

In this section, gap size has been taken into consideration for bubble fission regime.

Here, the relationship amongst gas pressure, gap size and capillary number has been

investigated. Microbubble splitting regimes will occur when the experimental capillary number exceeds the critical capillary number (De Menech et al., 2008; Rallison, 1984; Zhu, Kong, et al., 2016). Hence, it is necessary to figure out how capillary number changes along gap size and the critical capillary number in the system.

Figure 4-36 a) shows that a larger gap size requires higher gas pressure to initiate the microbubble fission regime. For instance, mother bubbles can be split into 2 daughter bubbles at a gas pressure of 132 kPa under a gap size of 100 μm or a gas pressure of 240 kPa under a gap size of 200 μm. This is due to the greater hydrodynamic resistance across the gap size of 200 μm. In microfluidics, hydrodynamic resistance of the channel depends on the channel length and size of bubble inside the channel (Belloul, Courbin, & Panizza, 2011; Cristobal, Benoit, Joanicot, & Ajdari, 2006). Hence, sufficient gas pressure is required to compensate for the pressure drop caused by the greater hydrodynamic resistance at the gap size of 200 μm. Additionally, higher gas pressure was required to split mother bubbles into large number of daughter bubbles (Jiang et al., 2016). For instance, under a gap size of 100 μm, when the gas pressure reached 155 kPa, a mother bubble can split into 3 daughter bubbles. However, a mother bubble was split into 2 daughter bubbles, when the gas pressure was 132 kPa.

Figure 4-36 b) demonstrates that a larger gap size creates a higher capillary number due to the larger gap size associating with higher gas pressure to split mother bubbles. For instance, under a gap size of 200 μm, the mother bubble starts to split at a gas pressure of 188 kpa and capillary number of 0.022. Under a gap size of 100

μm, the mother bubble starts to split at a gas pressure of 132 kpa and capillary number of 0.015.

Figure 4-36 c) shows that splitting number increases with an increase in the capillary number of both mother and daughter bubbles. This is due to the larger bubble being less stable and intending to split into greater numbers of smaller bubbles (Elemans, Bos, Janssen, & Meijer, 1993). When elevating gas pressure from 100 to 445 kPa, the residence time of bubbles was reduced owing to the increase of bubble travelling velocity inside channels for both mother and daughter bubbles. Meanwhile, the capillary number of the daughter bubbles is larger than the capillary number of the mother bubbles based on the boost of its velocity by the extra polymeric feeding supplied by the extra third T-junction. Bubble travelling velocity was increased also due to the smaller size of daughter bubbles relative to the mother bubbles. Smaller bubble size causes relatively smaller hydrodynamic resistance inside the channel (Belloul et al., 2011; Cristobal et al., 2006). From Figure 4-36 c), the capillary numbers of non-breaking mother bubbles are smaller than 0.01. Capillary number of daughter bubbles under three different gaps (100, 150 and 200 μm) were all greater than 0.01. Hence critical capillary number (Ca_{crit}). was found experimentally to be 0.01. Therefore, mother bubble capillary number smaller than 0.01 were not split under three liquid inlet flow rates fixed at 100 μL/min in this work. To ensure uniformed daughter bubbles from bubble fission regime, the future microfluidic device should be designed and operated above the Ca_{crit} of 0.01.

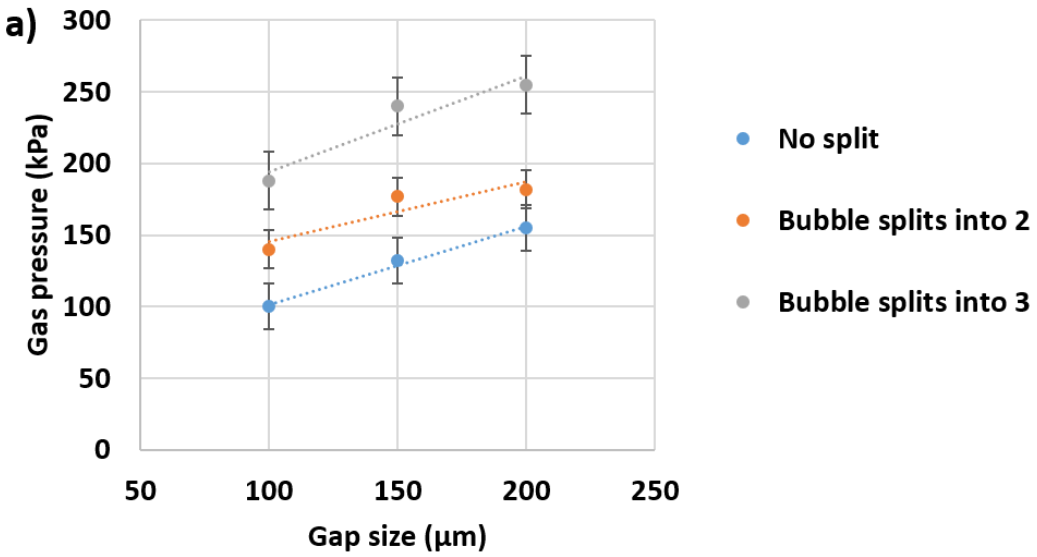
a)
300
250
200
150
100
50
0
Gas pressure (kPa)
50
100
150
200
250
Gap size (µm)
No split
Bubble splits into 2
Bubble splits into 3

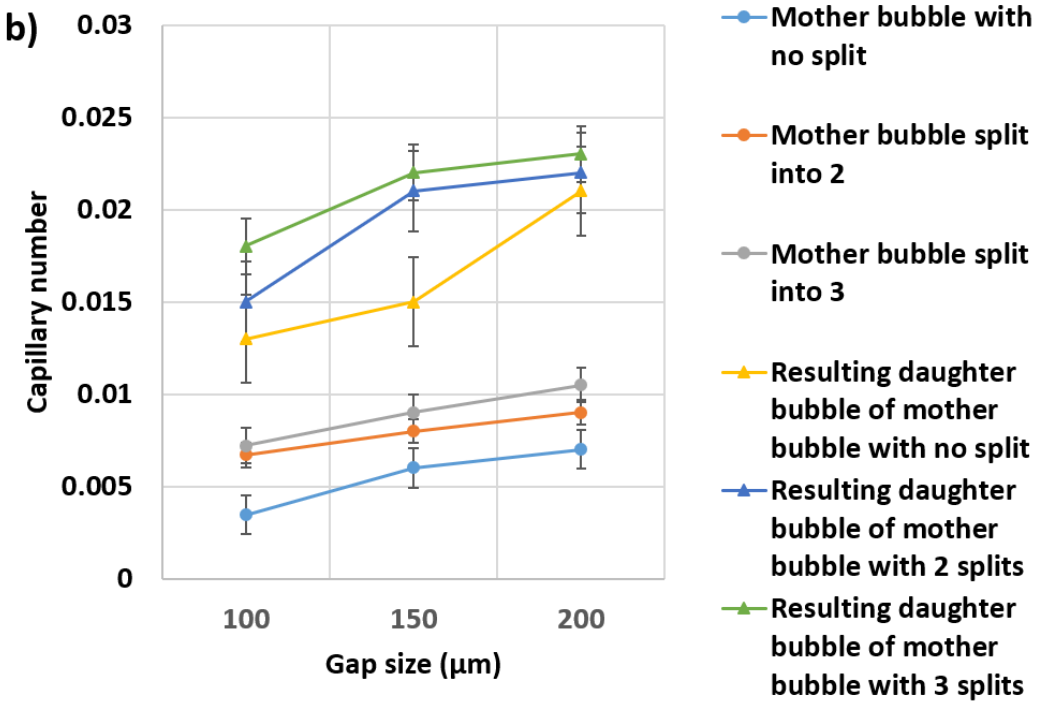
b)
0.03
0.025
0.02
0.015
0.01
0.005
0
Capillary number
100
150
200
Gap size (µm)
Mother bubble with no split
Mother bubble split into 2
Mother bubble split into 3
Resulting daughter bubble of mother bubble with no split
Resulting daughter bubble of mother bubble with 2 splits
Resulting daughter bubble of mother bubble with 3 splits

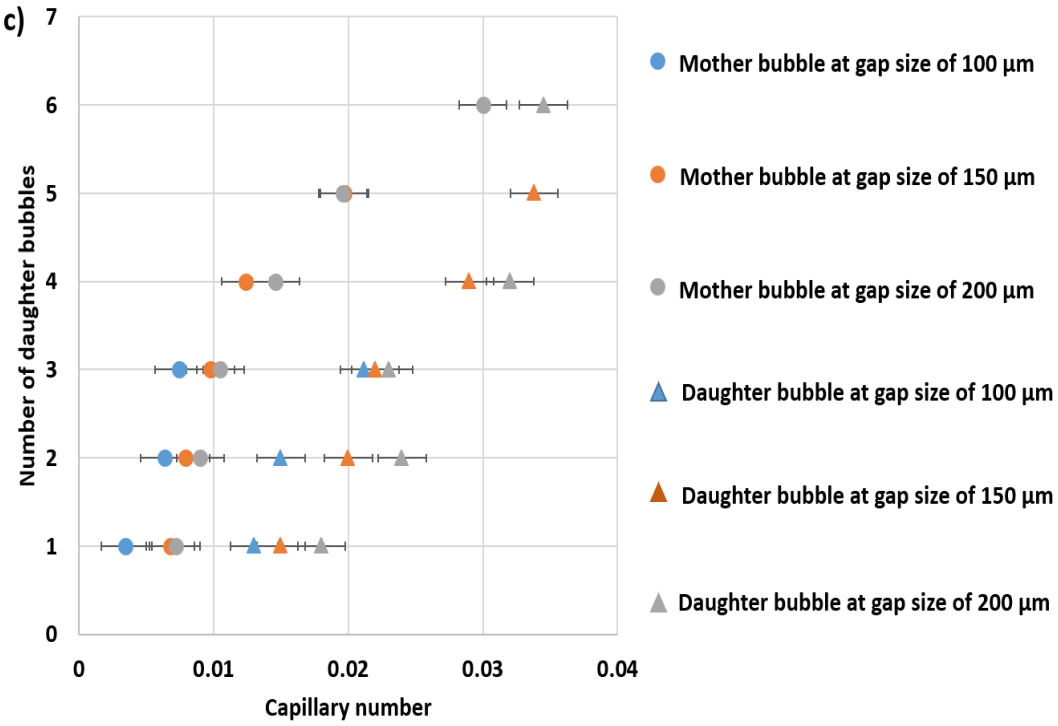

Figure 4-36: under three different gap sizes of 100 µm, 150 µm and 200 µm and constant liquid flow rates of 100 µl/min for all three liquid inlets: These experiments investigates a) the relationship between gap size and gas pressure; b) the relationship between gap size and its corresponding capillary number of mother and daughter bubbles; c) the relationship between capillary number and the resultant number of splitting.

4.3.3 Effect of liquid flow rate on bubble size and number of daughter bubbles per mother bubble

In this experiment, the relationship between liquid flow rate, capillary number and bubble fission regime was studied. Liquid flow rate at the third T-junction was varied from 100ul/min to 400ul/min at a constant gas pressure of 295 kPa under a gap size of 150 µm. To verify the experiment reproducibility and find the critical capillary number, above experiments were repeated under a gas pressure of 211 kPa. The size of the mother bubbles was measured from high speed camera video footages with Image J. To investigate the effect of gap size under a given gas pressure of 150 kPa,

gap size was changed to 90 µm. The flow rates at the liquid inlets of the first and second T-junctions were both constant at 100 µl/min

In Figure 4-37, monodispersed initial cylindrical mother bubbles were generated from the first two T-junctions at a gas pressure of 295 kPa and constant liquid flow rate of 100ul/min for first two T-junction, whilst liquid flow rate at the third T-junction inlet increased from 100ul/min to 400ul/min. Mother bubbles split into one to seven daughter microbubbles whose size decreased from 323 um to 147 um respectively. Figure 4-37 shows that control of the size and polydispersity of daughter bubbles can be achieved by simply tuning the liquid flow rates of the third T-junction inlet and splitting regimes only occurred at the third T-junction. Numbers of split daughter was controlled by tuning the flow rate at the third T-junction.

Capillary number (Equation 6) plays an important role on microbubble fission. The capillary number can be considered as the ratio of restoring force from the surface tension and the deforming viscous stress. There are two ways to generate daughter bubbles from mother bubbles by varying Ca. If Ca greatly exceeds the critical Ca value, bubbles deform into a long thin filament which is metastable and bursts into a huge number of small daughter bubbles owing to capillary waves.(Briscoe et al., 1999) However, if Ca only slightly exceeds the critical Ca value, tip streaming formation occurs, ejecting small daughter bubbles at the conical pointed end of mother bubbles (Rallison, 1984). The microbubble fission regime will stop, if mother bubble size is small enough to overcome the system hydrodynamic condition (Briscoe et al., 1999).

An increase in liquid inlet flow rate increases Ca of the exit channel. High Ca contributes to the higher perturbation in the system, which leads to the fission of microbubbles. Thus, a relatively large numbers of daughter bubbles occurs during one breakup event due to the action of capillary wave. For instance, the range of capillary number of daughter bubbles is between 0.03 and 0.09 in this work, which is greater than the critical Ca of 0.03 (result from Figure 4-38 b)). When capillary number is far greater than critical capillary number, transient flow occurs, where slender bubbles disintegrate into lines of bubbles due to disturbances driven by interfacial tension (Elemans et al., 1993). Once the size of bubbles become large enough, it will exhibit initially Rayleigh distortion (sinusoidal distortion). When the amplitude of the sinusoidal distortion is equivalent to the average slender radius, the breakup of droplets/bubbles happens(Elemans et al., 1993). Tomotika's results indicate that the growth rate of the instability was a function of the varicosity wavelength, with a maximum at a particular wavelength, which meant that the numbers of daughter bubbles with a definite size would be generated on break-up (Briscoe et al., 1999; Tomotika, 1934, 1936). Thus, initial mother bubbles started to split into 2, 3, 5 and more at the third T-junction of triple T-junction (Figure 4-37). The reason bubble is split into 3 daughter bubbles periodically semi-monodispersed is that the liquid and gas system were not balanced yet.

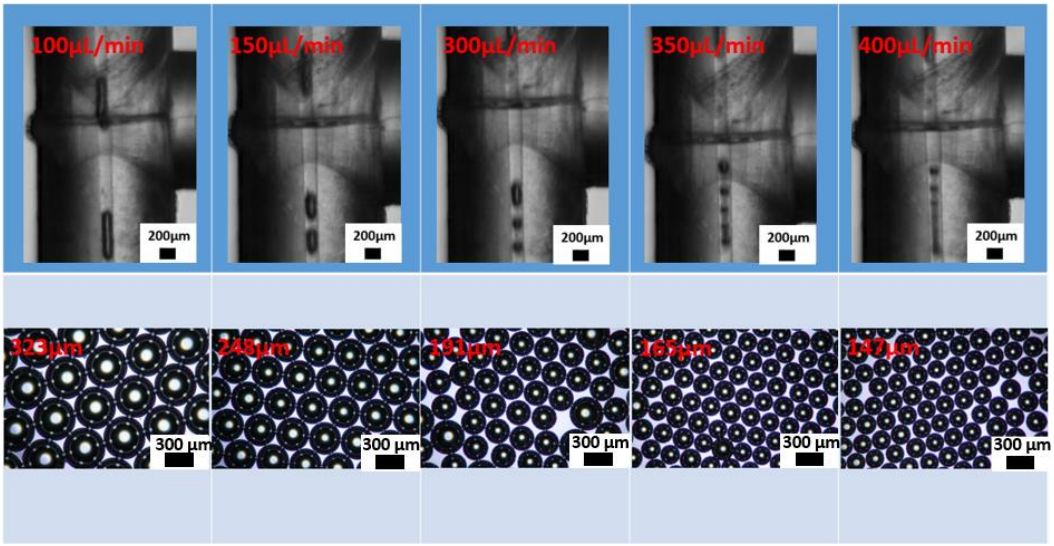

Figure 4-37: Daughter microbubbles size from 323 µm to 147 µm with increase liquid flow rate of the third inlet from 100uL/min to 400uL/min at gas pressure fixed at 295 kpa and gap size of 150 µm.

4.3.3.1 Effect of liquid flow rate on capillary number and splitting number of bubbles

In this section, gas pressure was set at 211 kPa and 295 kpa both under a gap size of 150 µm. Liquid flow rates for the first two T-junctions were both set to 100 µL/min and gap size of both fixed at 200 µm. The liquid flow rate for the third T-junction was increased from 100 µl/min to 600 µl/min in increments of 100 µl/min.

Figure 4-38 a) shows that capillary number of daughter bubbles is proportional to liquid flow rates. Capillary number of mother bubbles is inversely proportional to liquid flow rate. This is due to the high perturbation retarding the travelling velocity of mother bubbles. The high perturbation is caused by the high liquid inlet flow rate pumped into the third T-junction

Figure 4-38 b) illustrates that as the capillary number of mother bubbles was reduced, this changes the number of daughter bubbles from 8 to 1. In Figure 4-38 b) the mother bubble started to split when the capillary number is 0.03 which suggests that a capillary number of 0.03 is the critical capillary number in this experiment. The reason bubble was only split into 6 daughter bubbles under gas pressure of 295kPa is that the increase of capillary number broadens the size distribution (Rallison, 1984). Larger microbubbles are not as stable as smaller size microbubbles (Jiang et al., 2016). Larger capillary number enhances the imposed flow fluid distortion on bubbles inside the channel. Therefore, under the gas pressure of 295 kPa, daughter bubbles were produced in the outlet tubing before collecting from mother bubbles bursting.

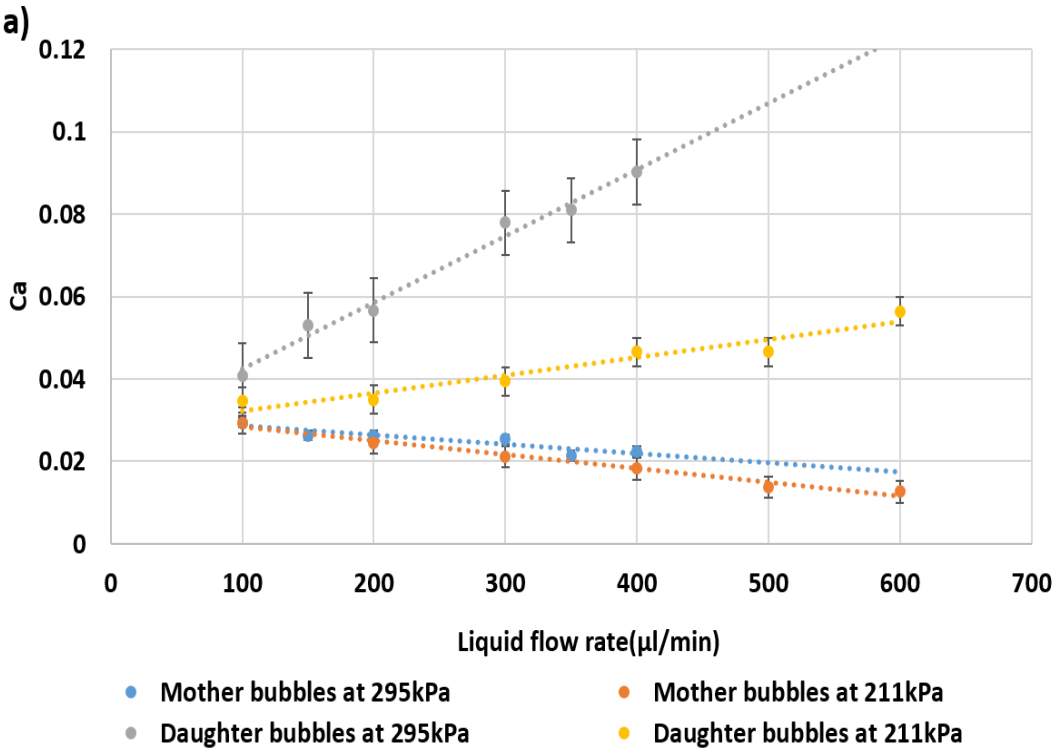

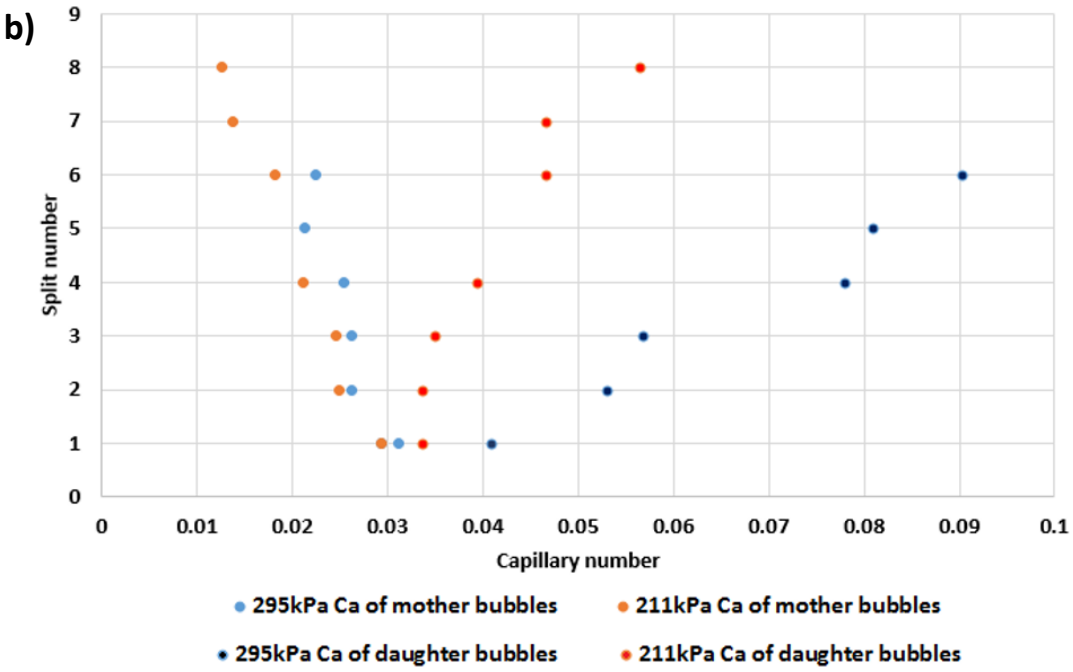

Figure 4-38: the effect of liquid flow rates on capillary numbers of mother and daughter bubbles and the number of splitting bubbles. a) shows how liquid flow rates influences the capillary number of mother and daughter bubbles relatively. b) illustrates how the capillary number affects the split number of bubbles, when liquid flow rate increases from 100 to 600 µl/min.

4.3.3.2 The effect of gap size under given gas pressure on microbubble fission regime

Rallison (Briscoe et al., 1999; Rallison, 1984) concludes that the deformation and breakage of a small bubble in a shear flow is relevant to the local velocity gradient experienced, and if the local shear rate is big enough, droplet or bubbles will split into two or more daughter droplets or bubbles. However, he also mentioned that rapid changes in flow rate can accelerate break-up of droplets or bubbles even far below the force normally considered enough to break. This effect is not only on the force required to break a bubble but also on the number of droplets/bubbles produced

later on (Briscoe et al., 1999; Rallison, 1984). When the daughter bubble size is small enough to overcome the prevailing hydrodynamic condition, mother bubbles stop splitting at the cross-sectional area of T-junction (Briscoe et al., 1999).

In Figure 4-39 and Figure 4-40, at a fixed gas pressure of 150 kPa and liquid flow rates of 100 uL/min for first two T-junctions. The gap size at the third T-junction was fixed at 90 µm (decreased from 150 µm in the previous experiment). As the third T-junction liquid flow rate was varied from 100 µl/min to 400 µl/min gradually, mother microbubbles breakage stopped, which is due to smaller gap size of 90 µm reduce its size and surrounding outer flow vorticity. This bubble size is smaller enough to overcome the prevailing hydrodynamic conditions in the triple T-junction condition. Another reason for failure of mother bubble breakup is due to the capillary number at a gap size of 90 µm being smaller than the critical number of 0.03 in this system. Figure 4-40 shows that the smallest microbubble size of 25 µm can be produced at a gas pressure of 150 kPa and liquid flow rate of 350 µL/min.

In summary, rapid production of monodispersed daughter microbubbles is readily achieved by a triple T-junction configuration because mother bubbles are split into different number of daughter microbubbles simply by adjusting the liquid flow rates at the third T-junction.

In Figure 4-40, it shows the relationship among liquid flow rates, gap size and bubble sizes. Sizes are inversely related to liquid flow rate due to mother bubbles having a shorter residence time to expand inside the channel. The size of daughter bubbles depends on the size of mother bubbles. Additionally, larger bubbles were produced

under a greater gap size. For instance, the largest mother bubble was 400 µm diameter, at gas pressure of 295kpa and liquid flow rate of 100 µl/min. The smallest mother bubble was 25 µm diameter, at gas pressure of 150 kPa and liquid flow rate of 350 µl/min.

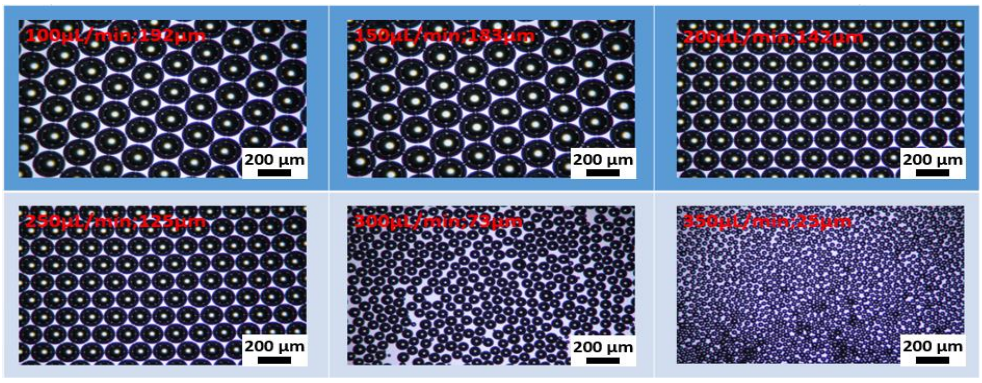

Figure 4-39: Microbubbles size decreased to 25um at 150 kPa and liquid flow rate of 350ul/min; gap size 90µm. Mother bubble size is smaller enough to overcome fluidic hydraulic resistance. Hence, splitting phenomenon didn't occur at gap size of 90 µm.

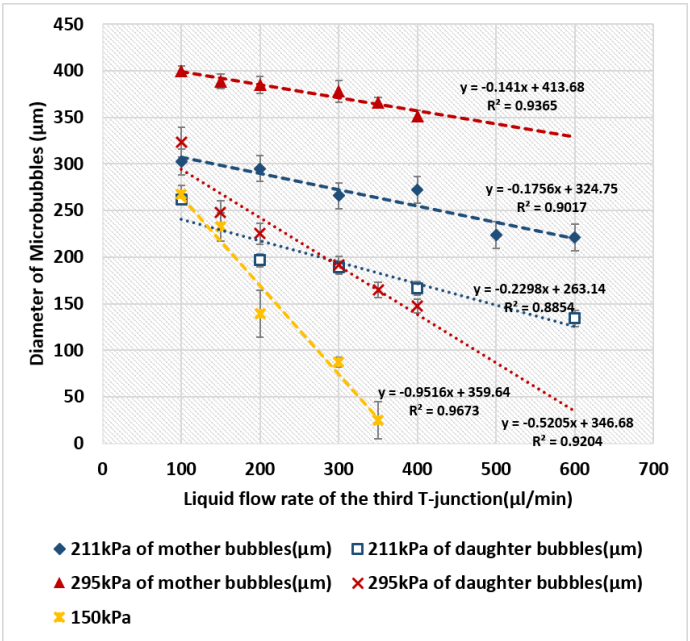

Figure 4-40: The diameter of mother bubbles produced by first two T-junctions and measured from high speed camera images. This graph reveals the relationship between mother and daughter bubbles at given gas pressure of 211 and 295 kPa under gap size of 150 µm varying liquid inlet from 100 µl/min to 600 µl/min. Gap size was 90 µm under gas pressure of 150 kPa.

4.3.4 The Effect of gap size on microbubbles fission mechanism

Mother microbubbles were produced upstream in the first two T-junctions. The first T-junction generated microbubbles with a narrow size distribution, bubble diameters were further reduced by second T-junction(Jiang et al., 2016). According to the studies above, two studies have been carried out systematically on the effect of gap size on microbubbles fission under certain gas pressure and liquid flow rates. Hence, this study here focusses on how the gap size of the third T-junction affects the fission mechanism of mother and daughter microbubbles, relatively. The gap size of the third T-junction was adjusted until bubbles did not split at the third T-junction. Monodispersed microbubbles were generated by altering the gas inlet pressure, and the all the liquid flow rates were at 100 µl/min.

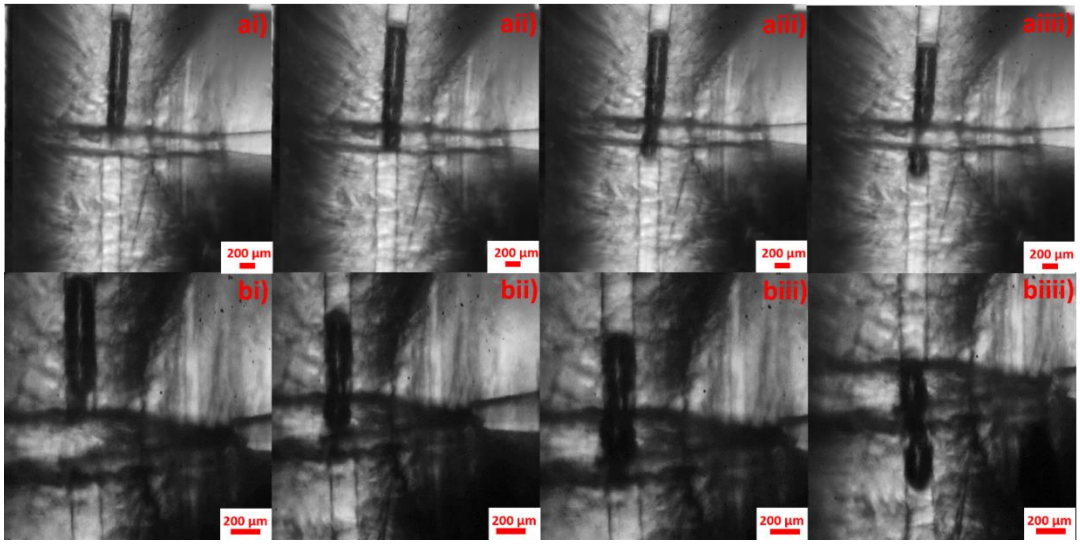

Figure 4-41: Formation methods for split microbubbles at gap size of 200 µm and 350 µm. Daughter bubbles were formed at the gap size of 200 µm by cone shape tip formation: ai), aii), aiii) and aiiii). Daughter bubbles were generated at the gap size of 350 µm by spindle shape tip formation: bi), bii), biii) and biiii).

According to Zhu and co-authors (Zhu, Kong, et al., 2016), the geometry of microfluidic channels, such as gap size, changes the flow velocity inside the channels

which notably affects the bubble behaviour. For instance, in our microfluidic device shown above, bubbles travelled from a narrow capillary with diameter of 200 μm to an expanded cylindrical area with a diameter of 1600 μm and width of 200 μm. Then bubbles were squeezed into the bottom capillary again with a diameter of 200 μm. Here, the width of the expand cylindrical area is referred as gap size in this work. The microchannel geometry in this microfluidic device can be simplified as confined area to expansion to confined area where the flow velocity increase owing to the channel contraction increases the shearing force, which causes the breakup of bubbles in the channel (Zhu, Kong, et al., 2016).

In this work, two methods of microbubble fission have been observed dependent on the gap size of the third T-junction. At a small gap size (circa 200 μm) cone shape tip formation occurred (Figure 4-41: ai), aii), aiii), aiiii)). The cone shaped tip formed within the T-junction gap could be explained by Zhu and co-authors. (Zhu, Tang, Tian, & Wang, 2016) that small gap size enhances the shear stresses contrast which causes the cone-shape tip. The cone shape was formed in the gap area due to the sharp contrast in viscous stresses seen in Figure 4-41 aiiii). According to Garsteki et. al (Garstecki et al., 2006a), the droplets/bubbles breakup occurs when the distortion of droplets/bubbles caused by viscous stress is greater than the effect of surface tension of droplets/bubbles. The monodispersed droplets/bubbles are produced in a dripping manner, when assuming the shearing force is constant during the experiments. Hence, daughter bubbles with controlled sizes were produced from the fission of primary mother bubbles.

At larger gap sizes (between 200 µm and 350 µm) spindle shape tip formation occurred (Figure 4-41: bi), bii), biii), biiii)). The mother bubble tip expanded within the gap due to the velocity drop within the gap. In Newtonian fluids, shear stress is linearly proportional to the velocity gradient. Hence, the increase of gap size decreases the differences in local shear stresses which results in a spindle-shaped tip. At a gap size of 500 µm and above, the mother bubble entering the gap shifts from the central axis to the side-wall of the gap. Occasionally mother bubbles become trapped in the gap which results in the splitting of mother bubbles into different sizes of daughter bubbles. It could be explained by Tan and co-authors (Y.-C. Tan, Collins, & Lee, 2003) that the mother bubble is no longer aligned with the shear force at the centre of the gap. Non-symmetric viscous shear force was exerted on the bubbles, which leading to fission of the mother bubbles in an uncontrolled manner.

4.3.5 Proof of concept

In this session, microbubble fission was investigated in glycerol/PEG40S solution. This demonstrates the feasibility of using a triple T-junction configuration to instigate the bubble fission phenomena and reduce bubble size for versatile polymeric materials besides BSA solution. Aqueous glycerol solutions were selected because of their wide use in experimental study of flow phenomena. Periodically partial-monodispersed microbubbles were generated in the triple T-junction via glycerol/PEG40S with a polydispersity index of 15 This is due to the amount of surfactant in the glycerol/PEG40S solution.

Surfactant plays a vital role in the polydispersity of microbubbles generated in glycerol/PEG40S. Stebe et al. Fuerstman et al. and Fu et al. have shown that the

motion of a surfactant-laden bubble with high surfactant concentration is the same as that of a surfactant-free bubble, due to the even spread of surfactant at the bubble surface by the Marangoni effect (Fu, Ma, & Li, 2014; Fuerstman et al., 2007; Stebe, Lin, & Maldarelli, 1991). Therefore, there is no surface tension gradient between the surface of the bubbles and the imposed liquid flow.

However, for intermediate or low surfactant concentrations a surfactant concentration gradient will occur at the bubble surface. Hydrodynamic pressure reduces rapidly along the body of bubbles, which reinforces tangential tractions on surface tension (Marangoni traction). This Marangoni traction can immobilize the interface and give rise to the shear stresses which create a pressure drop along the bubble length. In this study, the surfactant PEG40S is added to the continuous phase with a concentration of 2% w/w, which is below the critical micelle concentration of PEG40S. We hypothesise that the concentration of PEG40S is not sufficient to create an interface with uniform surfactant concentration such that bubbles act like surfactant-free bubbles. Furthermore, the high Marangoni force will tear the mother bubble into polydispersed daughter bubbles (Figure 4-42).

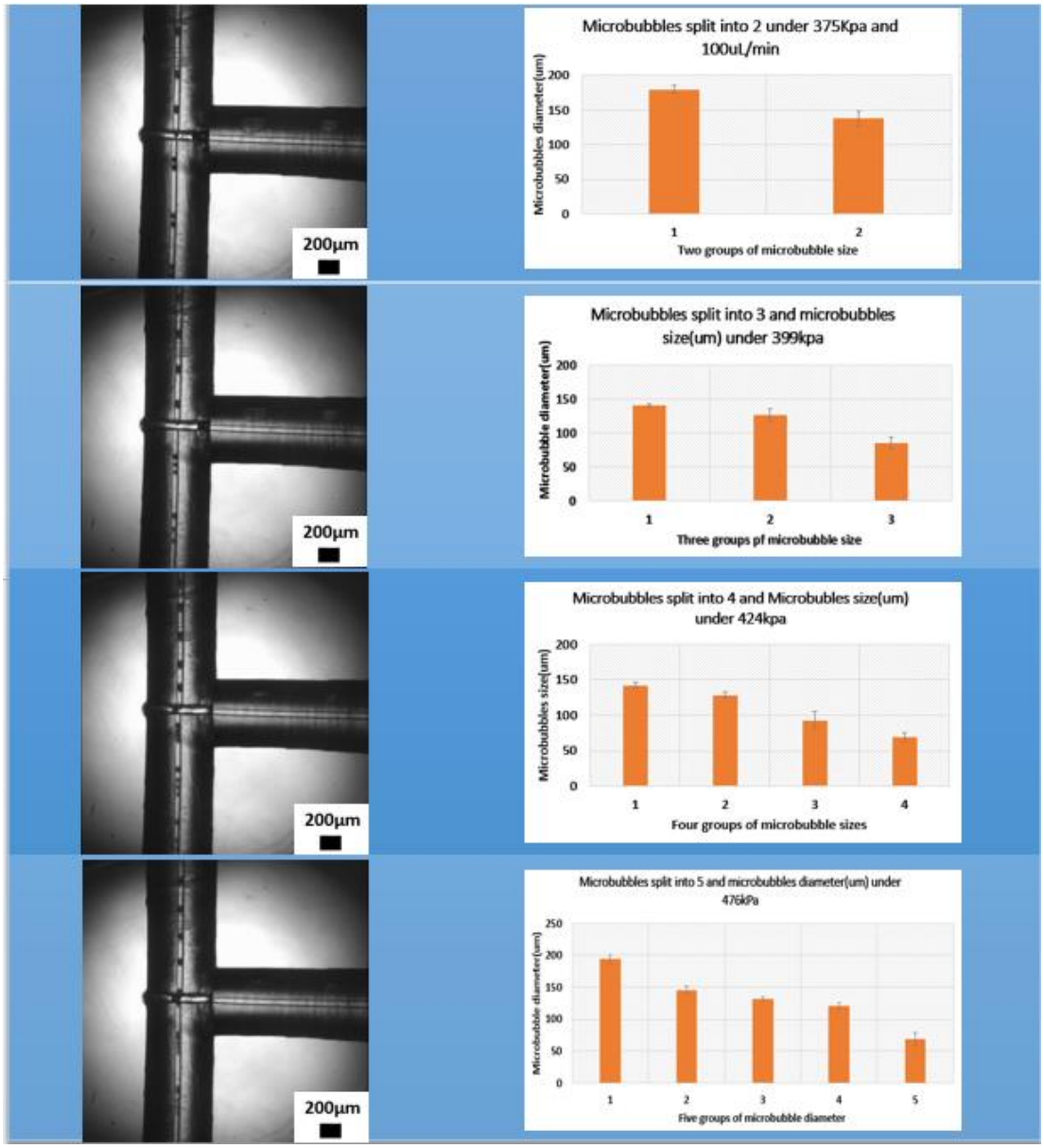

Figure 4-42: Fission regimes were reproduced by 50% w/w glycerol mixed with 2%w/w PEG40S in triple T-junction.

4.3.6 Summary

In this work, the microbubble fission regime occurred with a gas pressure over 75 kPa. Capillary number has been taken into consideration for the effect of microbubble fission. Critical capillary number, which is the indicator for breaking and

non-breaking microbubbles, was found experimentally. The relationship amongst the effects of gas pressure, liquid flow rates and gap size on the capillary number has been systematically studied separately in this work. Under a constant liquid flow rate of 100 µl/min, capillary number increases with the increase of gas pressure. Capillary number was elevated with an increase in gap size. This is due to the high gas pressure which was required to compensate for the hydrodynamic pressure drop in the larger gap size. Under a constant gas pressure of 295 kPa or 211 kPa, capillary number increases with an increase in liquid flow rates. This is due to the increase of bubble travelling velocity inside the channel. Under a gap size of 90 µm, bubble fission did not occurr with an increase in liquid flow rates as the capillary number of bubbles was lower than the critical capillary number. Hence, this work will be helpful for future microfluidic chips designed for microbubble fission.

Chapter 5 Conclusions and future work

5.1 Conclusions for this thesis

In this work, in Chapter 4 , various bioproducts have been fabricated with a microfluidic single T-junction device. The size of bubbles/scaffolds/nanoparticles can be altered either by flow rate ratio, solution concentration or device configuration. In section 4.1.2, here this section represents an interesting approach to fabricate 2D and 3D scaffolds with uniform porosity and desirable surface morphology. The uniform porosity of scaffolds was produced from monodispersed micro-droplets generated with a microfluidic single T-junction device. The surface was modified with nanoparticle deposition on the scaffolds. This is achieved by nanoparticle precipitation on the scaffold surface. Furthermore, nanoparticle deposition can enhance the surface roughness, which can be beneficial for cell adhesion and later for tissue formation. The density of nanoparticle deposit on the surface can be altered with amphiphilic polymer concentration. In section 4.1.3, monodispersed nanoparticle was formed inside microfluidic single T-junction device. The polydispersity index of nanoparticles produced with the microfluidic method is lower than that in the conventional method due to the confined mixing time in the microfluidic device. Both the concentration and the liquid flow rate ratio play an important role on the size of nanoparticles. The size of nanoparticles is decreased with the elevation of polymer solution concentration. Compared to polymer concentration, liquid flow rate plays a minor role for the size variance. After drying the sessile droplets containing nanoparticles, two types of pattern was formed due to the different size of nanoparticles. A snow flake pattern was formed in this

experiment with PLGA-b-PEG nanoparticles 150 nm in size. Micro-stripe pattern formation occured, when PLGA-b-PEG size is around 100 nm. The stripe pattern formation is due to the Marangoni flow inside sessile droplets.

A new double T-junction device was tested to investigate the potential for producing microbubbles with confined sizes.in section 4.2.2. It was shown that the size and production of microbubbles could be manipulated by introduction of a second junction into the commonly used single T-junction device. A comparison study was conducted to produce BSA microbubbles both with a single T-junction and then a double T-junction. The microbubbles produced via the double T-junction were different in size and stability for a given flow rate and gas pressure. It was shown that for the highest liquid flow rate (200 µl/min) at the lowest gas pressure (35kPa), microbubbles generated were smaller (272 ±5.2 µm) in the double T-junction. This can be described by the diffusion of gas into the liquid phase due to a longer residence time inside the microchannels, compared to a single T-junction system. While the diffusion of gas takes place, the velocity of the mixed flow is increased by the additional liquid flow rate through the second T-junction and therefore the production rate is not compromised by keeping the microbubbles in microchannels by increasing the length of the single T-junction exit channel length. From the experimental data, for the range of the ratio of the gas/liquid flows studied, a scaling predictive model was obtained where the normalized microbubble diameter can be estimated for a given number of T-junctions connected. The experimental results and the predictive data were plotted and the proximity of the experimental data to the parity line shows that the predictive model is in agreement with the experimental

data. A key feature from this predictive model is to investigate whether it is possible to reduce the microbubble size progressively by connecting more T-junctions to the current setup to enable production of microbubbles with diameters <8 μm (such as would be required for intravenous administration in biomedical applications). It is shown from the predictive model that achieving this with the same coarse channel diameter of 200 μm is viable by increasing the number of T-junctions. Furthermore, it is shown that the stability of microbubbles was improved by inserting the second T-junction.

In section 4.2.3, two verification experiments have been conducted to further investigate the characteristics of double T-junction, as well. The range of microbubble diameters generated by the triple T-junction device was in agreement with the predicted diameter of microbubbles from predicted scaling model based on single and double T-junctions brought up in this work. Furthermore, the experimental microbubble size obtained from triple T-junction was 18% smaller than those predicted by the scaling law, which suggests that a microbubble size ≤ 10 μm can be achieved with fewer than six T-junctions combined together. Moreover, according to the verification experiment, the variance of glycerol microbubble size was the same with the size trend line of BSA microbubbles obtained from both single and double T-junctions, which highlights the fact that the reduction of microbubble size is more relevant to the geometry of double T-junction rather than the material properties of BSA. In addition, it has been shown that double layered microbubbles can be produced with a double T-junction device. In order to get monodispersed double

layered microbubbles, more materials and process parameter combinations need to be investigated in the future.

In section 4.3, demonstrates the ability of a triple T-junction microfluidic device to control the size and quantity of monodispersed daughter microbubbles. Microbubble fission regime occurred when gas pressure is over 75 kPa. Here a systematic study has been carried out to investigate the effects of gas pressure, liquid flow rate and gap size on microbubble fission regimes. Capillary number is a non-dimensional parameter to represent the relationship between surface tension and viscous shear forces. Hence, this research focuses on the effect of capillary number on the microbubble fission regime. Critical capillary number is the index of breaking and non-breaking microbubbles. Therefore, the critical capillary number has been found to be 0.01 for a given liquid flow rate of 100 µl/min and 0.03 for a given gas pressure of 211 kPa and 295 kPa. The relationship among the effect of gas pressure, liquid flow rates and gap size on capillary number has been systematically studied separately in this work. Under the constant liquid flow rate of 100 µl/min, capillary number increases with the increase of gas pressure. Capillary number is elevated with an increase in gap size, which is due to the higher gas pressure required to compensate for the hydrodynamic pressure drop in the larger gap size. Under the constant gas pressure of 295 kPa or 211 kPa, capillary number increases with the increment of liquid flow rates, which is owing to the increase of bubble travelling velocity inside the channel. Under gap size of 90 µm, bubble fission did not occur with an increase in liquid flow rates, which is due to the capillary number of bubbles being lower than

the critical capillary number. The relationship between gap size and capillary number was also studied in this work.

The relationship between gas pressure, liquid flow rate, gap size and number of splitting is represented separately here. At a fixed liquid flow rate of 100uL/min for all three liquid inlets and gap size of 200 μm, mother bubbles fission occurred at the third T-junction and the numbers of daughter bubble per mother bubble can be manipulated by simply varying gas pressure. In detail, the numbers of daughter bubbles per mother bubble is proportional to the increase of gas pressure in this work. When gas pressure fixed at 211kPa and 295kPa respectively at given liquid flow rate of 100uL/min for first two T-junctions, the numbers of daughter bubbles arose with increase of third T-junction liquid flow rate from 100uL/min to 600uL/min. Then, the effect of geometries difference on microbubble fission conducted by enlarging the gap size from 90 μm to 400 μm. The size of daughter bubbles is positively correlated to the gap size. Microbubble survived at gap size of 90 μm, no break-up occurred because of the bubble is smaller enough to overcome the prevailing capillary hydrodynamic resistance. Fission regimes happened when gap size is bigger than 150 μm (capillary channel size is constantly 200 μm). The threshold pressure of bubble generation and split increased with the broaden gap size from 150 μm to 400 μm.

To prove the concept, glycerol/PEG40S was used as solution instead of BSA in the triple T-junction device. As a result, fission also occurred when altering the solution from BSA to glycerol/PEG40S. Critical capillary numbers for microbubbles fission were found experimentally under different operating conditions. Critical capillary

number can help future researchers to design their experiments and predict when and where microbubble fission occurs. Thus, the special structure of triple T-junction can create microbubbles fission regimes and improve the productivity of microbubbles which is also reproducible

5.2 Future work

According to previous work, the scaffolds and nanoparticles produced by single T-junction have great potential to be used as scaffolds for tissue engineering application and carriers for therapeutic drug delivery system. To carry on the study of PLGA-b-PEG scaffolds, indirect MTT assay will be first conducted to test the scaffolds cytotoxicity and biocompatibility. Then direct cell work will be done to assess tissue formation on scaffolds. Later on, more advanced PLGA-b-PEG scaffolds with optimised spatial architecture could be achieved by simple, reliable and reproducible single T-junction microfluidic method. Numerous functional molecules such as growth factors and antimicrobial drugs could be encapsulated inside scaffolds or coated on the surface of scaffolds to fabricate uniformed porous scaffolds with desirable biocompatibility and antimicrobial properties. Furthermore, amphiphilic polymer PLGA-b-PEG is not the only material to fabricate scaffolds for tissue engineering. Due to the versatility of microfluidics preparation method, natural materials such as protein and gelatin or biocomposite materials such as PLGA loaded with hydroxyapatite could be incorporated to manufacture scaffolds with suitable mechanical properties like viscoelasticity, mechanical strength and Young's modulus.

To carry on the investigation of PLGA-b-PEG nanoparticles, a drug can be loaded within the particles, and cell work and animal studies could be done to show the

interaction of cells and nanoparticles. Prior to cell work and animal study, *in vitro* drug release could be done with a UV-vis spectrophotomer and drug encapsulation efficiency could be determined.

Secondly, the remarkable characteristics of double T-junction and combining more than two T-junctions together have been investigated. Further studies can be based on the production of double or multi-layered microbubbles in the future. Moreover, monodispersity and stability are two key factors for industry applications such as coated ultrasound contrast agents and therapeutic drug delivery carries. Previously, double T-junction already has been proven in its ability to generate double layered microbubbles in section 4.6. The issue of how to produce monodispersed double layered microbubbles is the first issue to be solved in the future. In order to address this problem, the different materials and various liquid-gas flow rate ratio combinations have to be tried by using double T-junction. Additionally, the microfluidic method has excellent advantages in producing monodispersed microbubbles, droplets and multiple emulsions. Meanwhile, there are three main types of microfluidic devices such as co-flowing, flow-focusing and cross-flowing (T-junction) devices (R. Chen et al., 2012). Therefore, double or multiple layered microbubbles can be generated by not only double T-junction, but also any two geometry combinations from the three main types of microfluidic devices (R. Chen et al., 2012; Wan et al., 2008). Inspired by this thought, a new device comprising of a single T-junction referred as cross-flowing microfluidic device combined with a single V-junction (Figure 5-1) regarded as flow-focusing microfluidic device combined together can also be tested for their potential to make double or multiple layered

microbubbles at the same time. Once monodispersed microbubble are produced, by adding a photo-initiator, UV irradiation experiments can be done to solidify the outer layer of double layered microbubbles. Then, the thickness of double layered microbubbles can be investigated by laser scanning confocal microscope and scanning electron microscopy experiments.

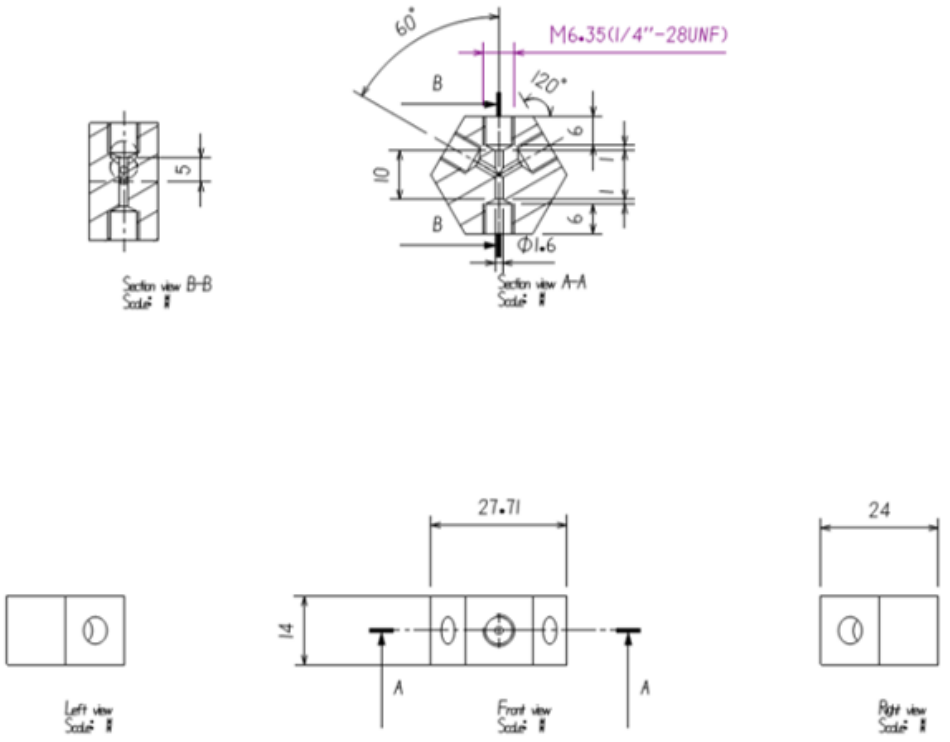

Figure 5-1: CAD design of microfluidic Y-junction.

For the triple T-junction research, COMSOL software could be introduced to simulate the bubble fission regime to help us systematically understand the formation, fission of microbubbles fabricated by triple T-junction. Moreover, this simulation study has the potential to predict the physical operation parameters for the different size range of microbubbles, which can be useful for biomedical applications, especially for ultrasound contrast agents.

Bibliography

Abbaspourrad, A., Duncanson, W. J., Lebedeva, N., Kim, S. H., Zhushma, A. P., Datta, S. S., … Weitz, D. A. (2013). Microfluidic fabrication of stable gas-filled microcapsules for acoustic contrast enhancement. *Langmuir*, *29*(40), 12352–12357. https://doi.org/10.1021/la402598p

Ago, K. I., Nagasawa, K., Takita, J., Itano, R., Morii, N., Matsuda, K., & Takahashi, K. (2005). Development of an aerobic cultivation system by using a microbubble aeration technology. *Journal of Chemical Engineering of Japan*, *38*(9), 757–762. https://doi.org/10.1252/jcej.38.757

Ahmad, B., Stride, E., & Edirisinghe, M. (2012). Calcium Alginate Foams Prepared by a Microfluidic T-Junction System: Stability and Food Applications. *Food and Bioprocess Technology*, *5*(7), 2848–2857. https://doi.org/10.1007/s11947-011-0650-3

Alter, J., Sennoga, C. A., Lopes, D. M., Eckersley, R. J., & Wells, D. J. (2009). Microbubble Stability is a Major Determinant of the Efficiency of Ultrasound and Microbubble Mediated in vivo Gene Transfer. *Ultrasound in Medicine & Biology*, *35*(6), 976–984. https://doi.org/10.1016/j.ultrasmedbio.2008.12.015

Andrieux, S., Drenckhan, W., & Stubenrauch, C. (2018). Generation of solid foams with controlled polydispersity using microfluidics. *Langmuir*, *34*, 1581–1590. https://doi.org/10.1021/acs.langmuir.7b03602

Anna, G. F. C. and S. L. (2007). Microfluidic methods for generating continuous

droplet streams. *Journal of Physics D: Applied Physics*, *40*(19), R319. Retrieved from http://stacks.iop.org/0022-3727/40/i=19/a=R01

Baroud, C. N., Gallaire, F., & Dangla, R. (2010). Dynamics of microfluidic droplets. *Lab Chip*, *10*, 2032–2045. https://doi.org/10.1039/c001191f

Barratt, G. M. (2000). Therapeutic applications of colloidal drug carriers. *Pharmaceutical Science and Technology Today*, *3*(5), 163–171. https://doi.org/10.1016/S1461-5347(00)00255-8

Basova, E. Y., & Foret, F. (2014). Droplet microfluidics in (bio)chemical analysis. *Analyst*, *140*(1), 22–38. https://doi.org/10.1039/C4AN01209G

Baysal, I., Ucar, G., Gultekinoglu, M., Ulubayram, K., & Yabanoglu-Ciftci, S. (2017). Donepezil loaded PLGA-b-PEG nanoparticles: their ability to induce destabilization of amyloid fibrils and to cross blood brain barrier in vitro. *Journal of Neural Transmission*, *124*, 33–45. https://doi.org/10.1007/s00702-016-1527-4

Belloul, M., Courbin, L., & Panizza, P. (2011). Droplet traffic regulated by collisions in microfluidic networks. *Soft Matter*, *7*, 9453–9458. https://doi.org/10.1039/c1sm05559c

Borden, M. (2010). NIH Public Access. *Bubble Sci Eng Technol.*, *1*, 3–17. https://doi.org/10.1179/175889709X446507.Microbubble

Borden, M. A., & Longo, M. L. (2002). Dissolution behavior of lipid monolayer-coated,

air-filled microbubbles: Effect of lipid hydrophobic chain length. *Langmuir*, *18*(24), 9225–9233. https://doi.org/10.1021/la026082h

Borrelli, M. J., O'Brien, W. D., Bernock, L. J., Williams, H. R., Hamilton, E., Wu, J., … Culp, W. C. (2012). Production of uniformly sized serum albumin and dextrose microbubbles. *Ultrasonics Sonochemistry*, *19*(1), 198–208. https://doi.org/10.1016/j.ultsonch.2011.05.010

Briscoe, B. J., Lawrence, C. J., & Mietus, W. G. P. (1999). A review of immiscible fluid mixing. *Advances in Colloid and Interface Science*, *81*, 1–17.

Brody, J. P., Yager, P., Goldstein, R. E., & Austin, R. H. (1996). Biotechnology at low reynolds numbers. *Biophysical*, *71*, 3430–3441.

Browning, R. J., Mulvana, H., Tang, M.-X., Hajnal, J. V., Wells, D. J., & Eckersley, R. J. (2012). Effect of albumin and dextrose concentration on ultrasound and microbubble mediated gene transfection in vivo. *Ultrasound in Medicine and Biology*, *38*(6), 1067–1077. https://doi.org/10.1016/j.ultrasmedbio.2012.02.020

Bružauskaitė, I., Bironaitė, D., Bagdonas, E., & Bernotienė, E. (2016). Scaffolds and cells for tissue regeneration: different scaffold pore sizes-different cell effects. *Cytotechnology*, *68*(3), 355–369. https://doi.org/10.1007/s10616-015-9895-4

Butler, B. D., & Hills, B. A. (1979). The lung as a filter for microbubbles. *Journal of Applied Physiology*, *47*(3), 537–543. Retrieved from

http://eutils.ncbi.nlm.nih.gov/entrez/eutils/elink.fcgi?dbfrom=pubmed&id=533747&retmode=ref&cmd=prlinks%5Cnpapers2://publication/uuid/365C22C0-3C4C-4AE6-A47C-1B83B6668527

Cai, Y., & Newby, B. Z. (2008). Marangoni flow-induced self-assembly of hexagonal and stripelike nanoparticle patterns. *JACS Communications*, *130*, 6076–6077.

Campbell, G. (1999). Creation and characterisation of aerated food products. *Trends in Food Science & Technology*, *10*(9), 283–296. https://doi.org/10.1016/S0924-2244(00)00008-X

Campbell, G. M., & Mougeot, E. (1999). Creation and characterisation of aerated food products. *Trends in Food Science & Technology*, *10*(9), 283–296. https://doi.org/10.1016/S0924-2244(00)00008-X

Cao, C., Gao, Y., Kang, L., & Luo, H. (2010). Self-assembly and synthesis mechanism of vanadium dioxide hollow microspheres. *CrystEngComm*, *12*(12), 4048. https://doi.org/10.1039/c0ce00321b

Cassell, E. A., Kaufman, K. M., & Matuevic, E. (1975). The effects of bubble size on microflotation. *Water Research*, *9*(12), 1017–1024. https://doi.org/10.1016/0043-1354(75)90095-0

Castro-Hernández, E., van Hoeve, W., Lohse, D., & Gordillo, J. M. (2011). Microbubble generation in a co-flow device operated in a new regime. *Lab on a Chip*, *11*(12), 2023–2029. https://doi.org/10.1039/c0lc00731e

Chahine, G. L., Kapahi, A., Choi, J.-K., & Hsiao, C.-T. (2016). Modeling of surface cleaning by cavitation bubble dynamics and collapse. *Ultrasonics Sonochemistry*, *29*, 528–549. https://doi.org/10.1016/j.ultsonch.2015.04.026

Chen, J. L., Dhanaliwala, A. H., Dixon, A. J., Klibanov, A. L., & Hossack, J. A. (2014). Synthesis and Characterization of Transiently Stable Albumin-Coated Microbubbles via a Flow-Focusing Microfluidic Device. *Ultrasound in Medicine & Biology*, *40*(2), 400–409. https://doi.org/10.1016/j.ultrasmedbio.2013.09.024

Chen, Q. Z. (2011). Foaming technology of tissue engineering scaffolds - a review. *Bubble Science, Engineering & Technology*, *3*(2), 34–47. https://doi.org/10.1179/1758897911Y.0000000003

Chen, R., Dong, P.-F., Xu, J.-H., Wang, Y.-D., & Luo, G.-S. (2012). Controllable microfluidic production of gas-in-oil-in-water emulsions for hollow microspheres with thin polymer shells. *Lab on a Chip*, *12*(20), 3858–3860. https://doi.org/10.1039/c2lc40387k

Chen, Y., Wang, Z., He, Y., Yoon, Y. J., Jung, J., Zhang, G., & Lin, Z. (2018). Light-enabled reversible self-assembly and tunable optical properties of stable hairy nanoparticles. In *Proceedings of the National Academy of Sciences* (pp. 1391–1400). https://doi.org/10.1073/pnas.1714748115

Cheng, J., Teply, B. A., Sherifi, I., Sung, J., Luther, G., Gu, F. X., … Farokhzad, O. C. (2007). Formulation of functionalized PLGA-PEG nanoparticles for in vivo targeted drug delivery. *Biomaterials*, *28*, 869–876.

https://doi.org/10.1016/j.biomaterials.2006.09.047

Choi, S. U. S. (2008). Nanofluids: a new field of scientific research and innovative applications. *Heat Transfer Engineering*, *29*, 429–431. https://doi.org/10.1080/01457630701850778

Christopher, G. F., Noharuddin, N. N., Taylor, J. A., & Anna, S. L. (2008). Experimental observations of the squeezing-to-dripping transition in T-shaped microfluidic junctions. *Physical Review E*, *78*, 1–12. https://doi.org/10.1103/PhysRevE.78.036317

Chung, H. J., & Park, T. G. (2007). Surface engineered and drug releasing pre-fabricated scaffolds for tissue engineering. *Advanced Drug Delivery Reviews*, *59*(4–5), 249–262. https://doi.org/10.1016/j.addr.2007.03.015

Chung, K. Y., Mishra, N. C., Wang, C. C., Lin, F. H., & Lin, K. H. (2009). Fabricating scaffolds by microfluidics. *Biomicrofluidics*, *3*(2). https://doi.org/10.1063/1.3122665

Collins, D. J., Neild, A., DeMello, A., Liu, A.-Q., & Ai, Y. (2015). The Poisson distribution and beyond: methods for microfluidic droplet production and single cell encapsulation. *Lab Chip*, *15*, 3439–3459. https://doi.org/10.1039/C5LC00614G

Cristobal, G., Benoit, J., Joanicot, M., & Ajdari, A. (2006). Microfluidic bypass for efficient passive regulation of droplet traffic at a junction. *Applied Physics Letters*, *89*, 1–3. https://doi.org/10.1063/1.2221929

Cui, W., Bei, J., Wang, S., Zhi, G., Zhao, Y., Zhou, X., … Xu, Y. (2005). Preparation and evaluation of poly(L-lactide-co-glycolide) (PLGA) microbubbles as a contrast agent for myocardial contrast echocardiography. *Journal of Biomedical Materials Research - Part B Applied Biomaterials*, *73*(1), 171–178. https://doi.org/10.1002/jbm.b.30189

De Menech, M., Garstecki, P., Jousse, F., & Stone, H. A. (2008). Transition from squeezing to dripping in a microfluidic T – shaped junction. *Journal of Fluid Mech.*, *595*, 141–161.

Deegan, R. D., Bakajin, O., Dupont, T. F., Huber, G., Nagel, S. R., & Witten, T. A. (1997). Capillary flow as the cause of ring stains from dried liquid drops. *Nature*, *389*, 827–829. https://doi.org/10.1038/39827

Desgouilles, S., Vauthier, C., Bazile, D., Vacus, J., Grossiord, J.-L., Veillard, M., & Couvreur, P. (2003). The Design of Nanoparticles Obtained by Solvent Evaporation: A Comprehensive Study. *Langmuir*, *19*(22), 9504–9510. https://doi.org/10.1021/la034999q

Dijkmans, P. A., Juffermans, L. J. M., Musters, R. J. P., van Wamel, A., ten Cate, F. J., van Gilst, W., … Kamp, O. (2004). Microbubbles and ultrasound: From diagnosis to therapy. *European Journal of Echocardiography*, *5*(4), 245–256. https://doi.org/10.1016/j.euje.2004.02.001

Elemans, P. H. M., Bos, H. L., Janssen, J. M. H., & Meijer, H. E. H. (1993). Transient phenomena in dispersive mixing. *Chemical Engineering Science*, *48*, 267–276.

Elsayed, M., Kothandaraman, A., Edirisinghe, M., & Huang, J. (2016). Porous polymeric films from microbubbles generated using a T-Junction microfluidic device. *Langmuir*, *32*(50), 13377–13385. https://doi.org/10.1021/acs.langmuir.6b02890

Enayati, M., Ahmad, Z., Stride, E., & Edirisinghe, M. (2010). One-step electrohydrodynamic production of drug-loaded micro- and nanoparticles. *Journal of the Royal Society, Interface / the Royal Society*, *7*(45), 667–675. https://doi.org/10.1098/rsif.2009.0348

Epstein, P. S., & Plesset, M. S. (1950). On the Stability of Gas Bubbles inLiquid-Gas Solutions. *Journal of Chemical Physics*, *18*(11), 1505–1509. https://doi.org/10.1063/1.1747520

Farook, U., Stride, E., & Edirisinghe, M. J. (2009). Preparation of suspensions of phospholipid-coated microbubbles by coaxial electrohydrodynamic atomization. *Journal of the Royal Society, Interface / the Royal Society*, *6*(32), 271–277. https://doi.org/10.1098/rsif.2008.0225

Farook, U., Zhang, H. B., Edirisinghe, M. J., Stride, E., & Saffari, N. (2007). Preparation of microbubble suspensions by co-axial electrohydrodynamic atomization. *Medical Engineering & Physics*, *29*(7), 749–754. https://doi.org/10.1016/j.medengphy.2006.08.009

Ferreira, L. S., & Trierweiler, J. O. (2009). Modeling and simulation of the polymeric nanocapsule formation process. *IFAC Proceedings Volumes (IFAC-PapersOnline)*,

7(PART 1), 405–410. https://doi.org/10.1002/aic

Fonslow, B. R., Stein, B. D., Webb, K. J., Xu, T., Choi, J., Kyu, S., & Iii, J. R. Y. (2013). NIH Public Access, *10*(1), 54–56. https://doi.org/10.1038/nmeth.2250.Digestion

Fu, T., Ma, Y., Funfschilling, D., & Li, H. Z. (2009). Bubble formation and breakup mechanism in a microfluidic flow-focusing device. *Chemical Engineering Science*, *64*(10), 2392–2400. https://doi.org/10.1016/j.ces.2009.02.022

Fu, T., Ma, Y., & Li, H. Z. (2014). Hydrodynamic feedback on bubble breakup at a T-junction within an asymmetric loop. *American Institude of Chemical Engineers*, *60*, 1920–1929. https://doi.org/10.1002/aic

Fuerstman, M. J., Lai, A., Thurlow, M. E., Shevkoplyas, S. S., Stone, H. A., & Whitesides, G. M. (2007). The pressure drop along rectangular microchannels containing bubbles. *Lab Chip*, *7*, 1479–1489. https://doi.org/10.1039/b706549c

Gañán-Calvo, A. M., & Gordillo, J. M. (2001). Perfectly monodisperse microbubbling by capillary flow focusing. *Physical Review Letters*, *87*, 1–4. https://doi.org/10.1103/PhysRevLett.87.274501

Garstecki, P., Fuerstman, M. J., Stone, A., & Whitesides, G. M. (2006a). Formation of droplets and bubbles in a microfluidic T-junction — scaling and mechanism of break-up. *Lab Chip*, *6*, 437–446. https://doi.org/10.1039/b510841a

Garstecki, P., Fuerstman, M. J., Stone, H. a, & Whitesides, G. M. (2006b). Formation of droplets and bubbles in a microfluidic T-junction-scaling and mechanism of

break-up. *Lab Chip*, *6*, 437–446. https://doi.org/10.1039/b510841a

Garstecki, P., Fuerstman, M. J., & Whitesides, G. M. (2005). Nonlinear Dynamics of a Flow-Focusing Bubble Generator: An Inverted Dripping Faucet. *Physical Review Letters*, *94*(23), 234502. https://doi.org/10.1103/PhysRevLett.94.234502

Garstecki, P., & Whitesides, G. M. (2006). Flowing Crystals: Nonequilibrium Structure of Foam. *Physical Review Letters*, *97*(2), 24503. https://doi.org/10.1103/PhysRevLett.97.024503

Garti, N., & Bisperink, C. (1998). Double emulsions: Progress and applications. *Current Opinion in Colloid & Interface Science*, *3*(6), 657–667. https://doi.org/10.1016/S1359-0294(98)80096-4

Ge, H., Hu, Y., Jiang, X., Cheng, D., Yuan, Y., Bi, H., & Yang, C. (2002). Preparation, characterization, and drug release behaviors of drug nimodipine-loaded poly(caprolactone)-poly(ethylene oxide)-poly(caprolactone) amphiphilic triblock copolymer micelles. *Journal of Pharmaceutical Sciences*, *91*(6), 1463–1473. https://doi.org/10.1002/jps.10143

Gerber, F., Pierre Krafft, M., Waton, G., & Vandamme, T. F. (2006). Microbubbles with exceptionally long life—synergy between shell and internal phase components. *New Journal of Chemistry*, *30*(4), 524–527. https://doi.org/10.1039/b600061b

Glawdel, T., Elbuken, C., & Ren, C. L. (2012). Droplet formation in microfluidic T-junction generators operating in the transitional regime. I. Experimental

observations. *Physical Review E - Statistical, Nonlinear, and Soft Matter Physics*, *85*(1), 1–9. https://doi.org/10.1103/PhysRevE.85.016322

Gorce, J. M., Arditi, M., & Schneider, M. (2000). Influence of bubble size distribution on the echogenicity of ultrasound contrast agents: a study of SonoVue. *Investigative Radiology*, *35*(11), 661–671. https://doi.org/10.1097/00004424-200011000-00003

Gotoh, K., Harayama, K., & Handa, K. (2015). Combination effect of ultrasound and shake as a mechanical action for textile cleaning. *Ultrasonics Sonochemistry*, *22*, 412–421. https://doi.org/10.1016/j.ultsonch.2014.05.005

Greish, K. (2010). Enhanced Permeability and Retention (EPR) Effect for Anticancer Nanomedicine Drug Targeting BT - Cancer Nanotechnology: Methods and Protocols. In S. R. Grobmyer & B. M. Moudgil (Eds.), *Cancer nanotechnology* (pp. 25–37). Humana Press. https://doi.org/10.1007/978-1-60761-609-2_3

Grzelczak, M., Vermant, J., Furst, E. M., & Liz-Marza, L. M. (2010). Directed self-assembly of nanoparticles. *ACS Nano*, *4*, 3591–3605. https://doi.org/10.1021/nn100869j

Guggenheimer, J., & Moore, P. A. (2003). Xerostomia: Etiology, recognition and treatment. *The Journal of the American Dental Association*, *134*(1), 61–69. https://doi.org/10.14219/jada.archive.2003.0018

Gultekinoglu, M., Jiang, X., Bayram, C., Ulubayram, K., & Edirisinghe, M. (2018).

Honeycomb-like PLGA-b-PEG Structure Creation with T-junction Micro Droplets. *Langmuir*, *34*, 7989–7997. https://doi.org/10.1021/acs.langmuir.8b00886

Günther, A., & Jensen, K. F. (2006). Multiphase microfluidics: from flow characteristics to chemical and materials synthesis. *Lab on a Chip*, *6*(12), 1487–1503. https://doi.org/10.1039/b609851g

Guzman, R., & Vasquez, D. A. (2016). Surface tension driven flow on a thin reaction front. *European Physical Journal: Special Topics*, *225*, 2573–2580. https://doi.org/10.1140/epjst/e2016-60026-4

Hernot, S., & Klibanov, A. L. (2008a). Microbubbles in ultrasound-triggered drug and gene delivery. *Advanced Drug Delivery Reviews*, *60*(10), 1153–1166. https://doi.org/10.1016/j.addr.2008.03.005

Hernot, S., & Klibanov, A. L. (2008b). Microbubbles in ultrasound-triggered drug and gene delivery. *Advanced Drug Delivery Reviews*, *60*(10), 1153–1166. https://doi.org/10.1016/j.addr.2008.03.005

Herrero-Vanrell, R., Rincón, A. C., Alonso, M., Reboto, V., Molina-Martinez, I. T., & Rodríguez-Cabello, J. C. (2005). Self-assembled particles of an elastin-like polymer as vehicles for controlled drug release. *Journal of Controlled Release*, *102*(1), 113–122. https://doi.org/https://doi.org/10.1016/j.jconrel.2004.10.001

Hu, H., & Larson, R. G. (2005a). Analysis of the effects of marangoni stresses on the microflow in an evaporating sessile droplet. *Langmuir*, *21*, 3972–3980.

https://doi.org/10.1021/la0475270

Hu, H., & Larson, R. G. (2005b). Analysis of the microfluid flow in an evaporating sessile droplet. *Langmuir*, *21*, 3963–3971. https://doi.org/10.1021/la047528s

Hutli, E., Nedeljkovic, M. S., Bonyár, A., Radovic, N. A., Llic, V., & Debeljkovic, A. (2016). The ability of using the cavitation phenomenon as a tool to modify the surface characteristics in micro- and in nano-level. *Tribology International*, *101*, 88–97. https://doi.org/10.1016/j.triboint.2016.04.006

Ikeura, H., Kobayashi, F., & Tamaki, M. (2011). Removal of residual pesticides in vegetables using ozone microbubbles. *Journal of Hazardous Materials*, *186*(1), 956–959. https://doi.org/10.1016/j.jhazmat.2010.11.094

Jayasinghe, S. N., & Sullivan, A. C. (2006). Electrohydrodynamic Atomization: An Approach to Growing Continuous Self-Supporting Polymeric Fibers. *The Journal of Physical Chemistry B*, *110*(6), 2522–2528. https://doi.org/10.1021/jp0555089

Jiang, X., Zhang, Y., Edirisinghe, M., & Parhizkar, M. (2016). Combining microfluidic devices with coarse capillaries to reduce the size of monodisperse microbubbles. *RSC Advances*, *6*, 63568–63577. https://doi.org/10.1039/C6RA09802A

Johnson, K. L., Kendall, K., & Roberts, A. D. (1971). Surface energy and the contact of elastic solids. *Proceedings of the Royal Society A Mathematical, Physical and Engineering Sciences*, *324*(1558). Retrieved from https://doi.org/10.1098/rspa.1971.0141

Kamaly, N., Fredman, G., Subramanian, M., Gadde, S., Pesic, A., Cheung, L., … Cameron Farokhzad, O. (2013). Development and in vivo efficacy of targeted polymeric inflammation-resolving nanoparticles. In *Proceedings of the National Academy of Sciences* (Vol. 110, pp. 6506–6511). https://doi.org/10.1073/pnas.1303377110

Kang, S.-T., & Yeh, C.-K. (2011). Ultrasound microbubble contrast agents for diagnostic and therapeutic applications: current status and future design. *Chang Gung Medical Journal*, *35*(2), 125–139. https://doi.org/10.4103/2319-4170.106159

Kapellas, K., Jamieson, L. M., Do, L. G., Bartold, P. M., Wang, H., Maple-Brown, L. J., … Skilton, M. R. (2014). Associations between periodontal disease and cardiovascular surrogate measures among Indigenous Australians. *International Journal of Cardiology*, *173*(2), 190–196. https://doi.org/10.1016/j.ijcard.2014.02.015

Karimpoor, M., IIIangakoon, E., Reid, A. G., Claudiani, S., Edirisinghe, M., & Khorashad, J. S. (2018). Development of artificial bone marrow fibre scaffolds to study resistance to anti-leukaemia agents.pdf. *British Journal of Haematology*, *182*, 909–943.

Karnik, R., Gu, F., Basto, P., Cannizzaro, C., Dean, L., Kyei-Manu, W., … Farokhzad, O. C. (2008). Microfluidic platform for controlled synthesis of polymeric nanoparticles. *Nano Letters*, *8*, 2906–2912.

Karpitschka, S., Liebig, F., & Riegler, H. (2017). Marangoni contraction of evaporating sessile droplets of binary mixtures. *Langmuir*, *33*, 4682–4687. https://doi.org/10.1021/acs.langmuir.7b00740

Katiyar, A., & Sarkar, K. (2010). Stability analysis of an encapsulated microbubble against gas diffusion. *Journal of Colloid and Interface Science*, *343*(1), 42–47. https://doi.org/10.1016/j.jcis.2009.11.030

Katz, J., Leiman, B. C., & Butler, B. D. (1988). Effect of Inhalation Anaesthetics on Filtration of Venous Gas Emboli by The Pulmonary Vasculature. *British Journal of Anaesthesia*, *61*(2), 200–205. https://doi.org/10.1093/bja/61.2.200

Kawaguchi, S., & Ito, K. (2005). Dispersion Polymerization. In M. Okubo (Ed.), *Dispersion polymerization* (pp. 299–328). Berlin, Heidelberg: Springer Berlin Heidelberg. https://doi.org/10.1007/b100118

Keiser, L., Bense, H., Colinet, P., Bico, J., & Reyssat, E. (2017). Marangoni bursting: evaporation-induced emulsification of binary mixtures on a liquid layer. *Physical Review Letters*, *118*, 1–5. https://doi.org/10.1103/PhysRevLett.118.074504

Khademhosseini, A., & Langer, R. (2007). Microengineered hydrogels for tissue engineering. *Biomaterials*, *28*(34), 5087–5092. https://doi.org/https://doi.org/10.1016/j.biomaterials.2007.07.021

Kim, D., Chesler, N. C., & Beebe, D. J. (2006). A method for dynamic system characterization using hydraulic series resistance. *Lab Chip*, *6*, 639–644.

https://doi.org/10.1039/b517054k

Kooiman, K., Böhmer, M. R., Emmer, M., Vos, H. J., Chlon, C., Shi, W. T., … van Wamel, A. (2009). Oil-filled polymer microcapsules for ultrasound-mediated delivery of lipophilic drugs. *Journal of Controlled Release*, *133*(2), 109–118. https://doi.org/10.1016/j.jconrel.2008.09.085

Kreuter, J. (1994). *Colloidal drug delivery systems*. (J. Kreuter, Ed.). New York, NY: Marcel Dekker.

Kukizaki, M., & Goto, M. (2007). Spontaneous formation behavior of uniform-sized microbubbles from Shirasu porous glass (SPG) membranes in the absence of water-phase flow. *Colloids and Surfaces A: Physicochemical and Engineering Aspects*, *296*(1), 174–181. https://doi.org/10.1016/j.colsurfa.2006.09.042

Kwon, H. Y., Lee, J. Y., Choi, S. W., Jang, Y., & Kim, J.-H. (2001). Preparation of PLGA nanoparticles containing estrogen by emulsification-diffusion method. *Colloids and Surfaces A: Physicochemical and Engineering Aspects*, *182*(1–3), 123–130.

Lamprecht, A., Ubrich, N., Yamamoto, H., Schäfer, U., Takeuchi, H., Maincent, P., … Lehr, C.-M. (2001). Biodegradable Nanoparticles for Targeted Drug Delivery in Treatment of Inflammatory Bowel Disease. *Journal of Pharmacology and Experimental Therapeutics*, *299*(2), 775 LP – 781.

Lau, C. K., & Dickinson, E. (2005). Instability and structural change in an aerated system containing egg albumen and invert sugar. *Food Hydrocolloids*, *19*(1),

111–121. https://doi.org/10.1016/j.foodhyd.2004.04.020

Lee, M., Lee, E. Y., Lee, D., & Park, B. J. (2015). Stabilization and fabrication of microbubbles: applications for medical purposes and functional materials. *Soft Matter*, *11*, 2067–2079. https://doi.org/10.1039/C5SM00113G

Leung, M. H. M., & Shen, A. Q. (2018). Microfluidic assisted nanoprecipitation of PLGA nanoparticles for curcumin delivery to leukemia jurkat cells. *Langmuir*, *34*, 3961–3970. https://doi.org/10.1021/acs.langmuir.7b04335

Li, B., Kan, L., Zhang, X., Li, J., Li, R., Gui, Q., … Wei, H. (2017). Biomimetic bone-like hydroxyapatite by mineralization on supramolecular porous fiber networks. *Langmuir*, *33*, 8493–8502. https://doi.org/10.1021/acs.langmuir.7b02394

Lien, S.-M., Ko, L.-Y., & Huang, T.-J. (2009). Effect of pore size on ECM secretion and cell growth in gelatin scaffold for articular cartilage tissue engineering. *Acta Biomaterialia*, *5*(2), 670–679. https://doi.org/10.1016/j.actbio.2008.09.020

Liger-Belair, G., Polidori, G., & Jeandet, P. (2008). Recent advances in the science of champagne bubbles. *Chemical Society Reviews*, *37*(11), 2490. https://doi.org/10.1039/b717798b

Lin, P.-J., Chuang, M.-C., & Chang, S.-C. (2015). Research on the Cleaning Efficacy of Micro-bubbles on Dental Plaque. *Procedia Manufacturing*, *3*, 13–20. https://doi.org/10.1016/j.promfg.2015.07.102

Link, D. R., Anna, S. L., Weitz, D. A., & Stone, H. A. (2004). Geometrically mediated

breakup of drops in microfluidic devices. *Physical Review Letters*, *92*, 1–4. https://doi.org/10.1103/PhysRevLett.92.054503

Liu, X., & Ma, P. X. (2009). Phase separation, pore structure, and properties of nanofibrous gelatin scaffolds. *Biomaterials*, *30*(25), 4094–4103. https://doi.org/10.1016/J.BIOMATERIALS.2009.04.024

Luque-Alcaraz, A. G., Lizardi-Mendoza, J., Goycoolea, F. M., Higuera-Ciapara, I., & Argüelles-Monal, W. (2016). Preparation of chitosan nanoparticles by nanoprecipitation and their ability as a drug nanocarrier. *RSC Advances*, *6*, 59250–59256. https://doi.org/10.1039/c6ra06563e

Ma, P X, & Choi, J. W. (2001). Biodegradable polymer scaffolds with well-defined interconnected spherical pore network. *Tissue Engineering*, *7*(1), 23–33. https://doi.org/10.1089/107632701300003269

Ma, Peter X, & Langer, R. (1999). Fabrication of Biodegradable Polymer Foams for Cell Transplantation and Tissue Engineering BT - Tissue Engineering Methods and Protocols. In J. R. Morgan & M. L. Yarmush (Eds.), *Tissue Engineering Methods and Protocols* (pp. 47–56). Totowa, NJ: Humana Press. https://doi.org/10.1385/0-89603-516-6:47

Mahalingam, S, Meinders, M. B., & Edirisinghe, M. (2014). Formation, stability, and mechanical properties of bovine serum albumin stabilized air bubbles produced using coaxial electrohydrodynamic atomization. *Langmuir*, *30*(23), 6694–6703. https://doi.org/10.1021/la5011715

Mahalingam, Suntharavathanan, Xu, Z., & Edirisinghe, M. (2015). Antibacterial activity and biosensing of PVA-Lysozyme microbubbles formed by pressurized gyration. *Langmuir*, *31*, 9771–9780. https://doi.org/10.1021/acs.langmuir.5b02005

Majumder, M., Rendall, C. S., Eukel, J. A., Wang, J. Y. L., Behabtu, N., Pint, C. L., … Pasquali, M. (2012). Overcoming the "coffee-stain" effect by compositional marangoni-flow-assisted drop-drying. *Journal of Physical Chemistry B*, *116*, 6536–6542. https://doi.org/10.1021/jp3009628

Manisha P., D., Vinod, L., Elka, W., Roberts J., L., & Gordon L., A. (1997). The mechanism of uptake of biodegradable microparticles in caco-2 cells is size dependent.

Manuscript, A., & Proximity, I. (2011). NIH Public Access, *4*(164), 400–409. https://doi.org/10.1126/scisignal.2001449.Engineering

Maske, S. K., Rai, D. S., Kale, V. S., Raut, B. D., Chintale, G. A., & College, I. (2012). I NTERNATIONAL J OURNAL OF P HARMACY & L IFE S CIENCES Microbubble and its applications. *International Journal of Pharmacy and Life Sciences*, *3*(12), 2228–2235.

Mason, T. J. (2016). Ultrasonic cleaning: An historical perspective. *Ultrasonics Sonochemistry*, *29*, 519–523. https://doi.org/10.1016/j.ultsonch.2015.05.004

Mikhailov, D. N. (2012). Oil recovery in the presence of microbubbles in the filtration

flow. *Journal of Applied Mechanics and Technical Physics*, *53*(3), 366–378. https://doi.org/10.1134/S002189441203008X

Moghimi, S. M., Hunter, A. C., & Murray, J. C. (2001). Long-Circulating and Target-Specific Nanoparticles: Theory to Practice. *Pharmacological Reviews*, *53*(2), 283 LP – 318.

Mohamedi, G., Azmin, M., Pastoriza-santos, I., Huang, V., Pe, J., Liz-marza, L. M., … Stride, E. (2012). E ff ects of Gold Nanoparticles on the Stability of Microbubbles. *ACS Nano*, (7), 5767–5783.

Mulvana, H., Browning, R. J., Tang, M.-X., Hajnal, J. V., & Eckersley, R. J. (2012). Albumin Coated Microbubble Optimization: Custom Fabrication and Comprehensive Characterization. *Ultrasound in Medicine & Biology*, *38*(9), 1599–1607. https://doi.org/10.1016/j.ultrasmedbio.2012.05.002

Nair, A., Yang, J., & Tang, L. (2006). A novel preparation of degradable scaffolds using BSA microbubbles as porogen. *2007 IEEE Dallas Engineering in Medicine and Biology Workshop*, *10*(1109), 1–4.

Nance, W. C., Dowd, S. E., Samarian, D., Chludzinski, J., Delli, J., Battista, J., & Rickard, A. H. (2013). A high-throughput microfluidic dental plaque biofilm system to visualize and quantify the effect of antimicrobials. *Journal of Antimicrobial Chemotherapy*, *68*(11), 2550–2560. https://doi.org/10.1093/jac/dkt211

Nisisako, T., Torii, T., & Higuchi, T. (2002). Droplet formation in a microchannel

network. *Lab Chip*, *2*, 24–26. https://doi.org/10.1039/b108740c

Nyborg, W. L. (2001). Biological effects of ultrasound: Development of safety guidelines. Part II: General review. *Ultrasound in Medicine & Biology*, *27*(3), 301–333. https://doi.org/10.1016/S0301-5629(00)00333-1

O'Brien, F. J. (2011). Biomaterials & scaffolds for tissue engineering. *Materials Today*, *14*(3), 88–95. https://doi.org/10.1016/S1369-7021(11)70058-X

Ozkan, O., & Erbil, H. Y. (2017). Interpreting contact angle results under air, water and oil for the same surfaces. *Surface Topography: Metrology and Properties*, *5*, 024002. https://doi.org/10.1088/2051-672X/aa6e02

Panyam, J., & Labhasetwar, V. (2003). Biodegradable nanoparticles for drug and gene delivery to cells and tissue. *Advanced Drug Delivery Reviews*, *55*(3), 329–347. https://doi.org/https://doi.org/10.1016/S0169-409X(02)00228-4

Parhizkar, M., Edirisinghe, M., & Stride, E. (2013). Effect of operating conditions and liquid physical properties on the size of monodisperse microbubbles produced in a capillary embedded T-junction device. *Microfluidics and Nanofluidics*, *14*(5), 797–808. https://doi.org/10.1007/s10404-012-1098-0

Parhizkar, Maryam. (2014). Preparation of monodisperse microbubbles in a capillary embedded T-Junction device and the influence of process control parameters on bubble size and stability.

Parhizkar, Maryam, Sofokleous, P., Stride, E., & Edirisinghe, M. (2014). Novel

preparation of controlled porosity particle/fibre loaded scaffolds using a hybrid micro-fluidic and electrohydrodynamic technique. *Biofabrication*, *6*(4), 045010. https://doi.org/10.1088/1758-5082/6/4/045010

Parhizkar, Maryam, Stride, E., & Edirisinghe, M. (2014). Preparation of monodisperse microbubbles using an integrated embedded capillary T-junction with electrohydrodynamic focusing. *Lab on a Chip*, 2437–2446. https://doi.org/10.1039/c4lc00328d

Parsa, M., Harmand, S., & Sefiane, K. (2018). Mechanisms of pattern formation from dried sessile drops. *Advances in Colloid and Interface Science*, *254*, 22–47. https://doi.org/10.1016/j.cis.2018.03.007

Peng, H., Xu, Z., Chen, S., Zhang, Z., Li, B., & Ge, L. (2015). An easily assembled double T-shape microfluidic devices for the preparation of submillimeter-sized polyacronitrile (PAN) microbubbles and polystyrene (PS) double emulsions. *Colloids and Surfaces A: Physicochemical and Engineering Aspects*, *468*, 271–279. https://doi.org/10.1016/j.colsurfa.2014.12.016

Peyman, S. a., Abou-Saleh, R. H., McLaughlan, J. R., Ingram, N., Johnson, B. R. G., Critchley, K., … Evans, S. D. (2012). Expanding 3D geometry for enhanced on-chip microbubble production and single step formation of liposome modified microbubbles. *Lab on a Chip*, *12*(21), 4544. https://doi.org/10.1039/c2lc40634a

Pitt, G. G., Gratzl, M. M., Kimmel, G. L., Surles, J., & Sohindler, A. (1981). Aliphatic polyesters II. The degradation of poly (DL-lactide), poly (ε-caprolactone), and

their copolymers in vivo. *Biomaterials*, *2*(4), 215–220. https://doi.org/https://doi.org/10.1016/0142-9612(81)90060-0

Pliable, O. F., Tissues, S., & Engineer, F. T. O. (1996). Fabrication of Pliable Biodegradable Polymer Soft Tissues, *5*(4), 465–473. https://doi.org/10.1016/0963-6897(96)00025-5

Pluta, K., Malina, D., & Sobczak-kupiec, A. (2015). SCAFFOLDS FOR TISSUE ENGINEERING. *Technical Transactions Chemistry*, *1*(17), 17–27.

Prasad, A., Sankar, M. R., & Katiyar, V. (2017). State of Art on Solvent Casting Particulate Leaching Method for Orthopedic ScaffoldsFabrication. *Materials Today: Proceedings*, *4*(2, Part A), 898–907. https://doi.org/https://doi.org/10.1016/j.matpr.2017.01.101

Rallison, J. M. (1984). The deformation of small viscous drops and bubbles in shear flows. *Annual Review of Fluid Mechanics*, *16*, 45–66.

Rodrigues, R. T., & Rubio, J. (2007). DAF–dissolved air flotation: Potential applications in the mining and mineral processing industry. *International Journal of Mineral Processing*, *82*(1), 1–13. https://doi.org/10.1016/j.minpro.2006.07.019

Rongy, L., & De Wit, A. (2006). Steady Marangoni flow traveling with chemical fronts. In *Journal of Chemical Physics* (Vol. 124). https://doi.org/10.1063/1.2186313

Rowley, J. A., Madlambayan, G., & Mooney, D. J. (1999). Alginate hydrogels as synthetic extracellular matrix materials. *Biomaterials*, *20*(1), 45–53.

https://doi.org/https://doi.org/10.1016/S0142-9612(98)00107-0

Rudin, A., & Choi, P. (2013). Chapter 10 - Dispersion and Emulsion Polymerizations. In A. Rudin & P. B. T.-T. E. of P. S. & E. (Third E. Choi (Eds.), *The elements of polymer science and engineering* (pp. 427–447). Boston: Academic Press. https://doi.org/https://doi.org/10.1016/B978-0-12-382178-2.00010-9

Sánchez-Iglesias, A., Grzelczak, M., Altantzis, T., Goris, B., Pérez-Juste, J., Bals, S., … Liz-Marzán, L. M. (2012). Hydrophobic interactions modulate self-assembly of nanoparticles. *ACS Nano*, *6*, 11059–11065. https://doi.org/10.1021/nn3047605

Sari, E., Tunc-Sarisozen, Y., Mutlu, H., Shahbazi, R., Ucar, G., & Ulubayram, K. (2015). ICAM-1 targeted catalase encapsulated PLGA- b -PEG nanoparticles against vascular oxidative stress. *Journal of Microencapsulation*, *32*, 687–698. https://doi.org/10.3109/02652048.2015.1073384

Schantz, G. (2014). MICROBUBBLES AS A METHOD OF DRUG DELIVERY FOR TUMOROUS MICROBUBBLE TREATMENT OF, 1–8.

Seeber, A. (1989). Neurobehavioral toxicity of long-term exposure to tetrachloroethylene. *Neurotoxicology and Teratology*, *11*(6), 579–583. https://doi.org/10.1016/0892-0362(89)90041-X

Sharma, P. K., Gibcus, M. J., Van Der Mei, H. C., & Busscher, H. J. (2005). Influence of fluid shear and microbubbles on bacterial detachment from a surface. *Applied and Environmental Microbiology*, *71*(7), 3668–3673.

https://doi.org/10.1128/AEM.71.7.3668-3673.2005

Shashank, S., Jameel, F., James, K., Shunichi, H., & Mark, B. (2010). Effect of Microbubble Size on Fundamental Mode High Frequency Ultrasound Imaging in Mice. *Ultrasound in Medicine and Biology*, *36*(6), 935–948. https://doi.org/10.1016/j.ultrasmedbio.2010.03.015.Effect

Shen, X., Ho, C.-M., & Wong, T.-S. (2010). Minimal size of coffee ring structure. *Journal of Physical Chemistry B*, *114*, 5269–5274. https://doi.org/10.1021/jp912190v

Shen, Y., Longo, M. L., & Powell, R. L. (2008). Stability and rheological behavior of concentrated monodisperse food emulsifier coated microbubble suspensions. *Journal of Colloid and Interface Science*, *327*(1), 204–210. https://doi.org/10.1016/j.jcis.2008.07.047

Shi, Z., Zhang, Y., Liu, M., Hanaor, D. A. H., & Gan, Y. (2018). Dynamic contact angle hysteresis in liquid bridges. *Colloids and Surfaces A: Physicochemical and Engineering Aspects*, *555*, 365–371. https://doi.org/https://doi.org/10.1016/j.colsurfa.2018.07.004

Shih, R., Hall, T., Hill, C., & Lee, A. P. (2013). NIH Public Access, *4*(1), 12–20. https://doi.org/10.1179/1758897912Y.0000000004.Scaled-Up

Silva, M. M. C. G., Cyster, L. A., Barry, J. J. A., Yang, X. B., Oreffo, R. O. C., Grant, D. M., … Rose, F. R. A. J. (2006). The effect of anisotropic architecture on cell and tissue infiltration into tissue engineering scaffolds. *Biomaterials*, *27*(35), 5909–5917.

https://doi.org/10.1016/j.biomaterials.2006.08.010

Şimşek, S., Eroğlu, H., Kurum, B., & Ulubayram, K. (2013). Brain targeting of Atorvastatin loaded amphiphilic PLGA-b-PEG nanoparticles. *Journal of Microencapsulation*, *30*, 10–20. https://doi.org/10.3109/02652048.2012.692400

Soetanto, K., & Chan, M. (2000). Fundamental studies on contrast images from different-sized microbubbles: Analytical and experimental studies. *Ultrasound in Medicine and Biology*, *26*(1), 81–91. https://doi.org/10.1016/S0301-5629(99)00107-6

Song, C. X., Labhasetwar, V. D., Murphy, H., Qu, X., Humphrey, W. R., Shebuski, R. J., & Levy, R. J. (1997). Formulation and characterization of biodegradable nanoparticles for intravascular local drug delivery. *Journal of Controlled Release*, *43*(2–3), 197–212.

Stebe, K. J., Lin, S. Y., & Maldarelli, C. (1991). Remobilizing surfactant retarded fluid particle interfaces. I. Stress-free conditions at the interfaces of micellar solutions of surfactants with fast sorption kinetics. *Physics of Fluids A*, *3*, 3–20. https://doi.org/10.1063/1.857862

Stride, E. (2008). The influence of surface adsorption on microbubble dynamics. *Philosophical Transactions. Series A, Mathematical, Physical, and Engineering Sciences*, *366*(1873), 2103–2115. https://doi.org/10.1098/rsta.2008.0001

Stride, E, & Edirisinghe, M. (2008). Novel microbubble preparation technologies. *Soft Matter*, *4*, 2350–2359. https://doi.org/10.1039/b809517p

Stride, E, & Saffari, N. (2003). Microbubble ultrasound contrast agents: a review. *Proceedings of the Institution of Mechanical Engineers. Part H, Journal of Engineering in Medicine*, *217*(6), 429–447. https://doi.org/10.1243/09544110360729072

Stride, Eleanor. (2009). Physical principles of microbubbles for ultrasound imaging and therapy. *Cerebrovascular Diseases*, *27*(SUPPL. 2), 1–13. https://doi.org/10.1159/000203122

Stride, Eleanor, & Edirisinghe, M. (2008). Novel microbubble preparation technologies. *Soft Matter*, *4*, 2350–2359. https://doi.org/10.1039/b809517p

Stride, Eleanor, & Edirisinghe, M. (2009). Novel preparation techniques for controlling microbubble uniformity: A comparison. *Medical and Biological Engineering and Computing*, *47*(8), 883–892. https://doi.org/10.1007/s11517-009-0490-8

Subia, B., Kundu, J., & Kundu, S. C. (2010). Biomaterial Scaffold Fabrication Techniques for Potential Tissue Engineering Applications. In D. Eberli (Ed.), *Tissue engineering* (pp. 141–158). IntechOpen. https://doi.org/10.5772/8581

Swarbrick, J., & Boylan, J. C. (2003). Encyclopaedia of Pharmaceutical Technology, 2nd edition Edited by J. Swarbrick and J. C. Boylan. 2002, Marcel Dekker: New

York. 2002. 3 Volumes. 3032 + 64 pp. ISBN 0-8247-2822-X (Vol. 1), 0-8247-2823-8 (Vol. 2), 0-8247-2824-6 (Vol. 3), 0-8247-2825-4 (Prep. *Organic Process Research & Development*, *7*(4), 609–610. https://doi.org/10.1021/op0340356

Takahashi, M., Kawamura, T., Yamamoto, Y., Ohnari, H., Himuro, S., & Shakutsui., H. (2003). Effect of shrinking microbubbles on gas hydrate formation. *Physical Chemistry B*, *107*(107), 2171–2173.

Tan, Y.-C., Collins, J., & Lee, A. P. (2003). Controlled fission of droplet emulsion in bifurcating microfluidic channels. In *Transducers 03 The 12th International Conference on Solid-State Sensors, Actuators and Microsystems, Boston, June 8-12, 2003* (Vol. 1, pp. 28–31). https://doi.org/10.1109/SENSOR.2003.1215245

Tan, Y., Fisher, J. S., Lee, A. I., Cristini, V., & Lee, A. P. (2004). Design of microfluidic channel geometries for the control of droplet volume, chemical concentration, and sorting. *Lab Chip*, *4*, 292–298.

Thorsen, T., Roberts, R. W., Arnold, F. H., & Quake, S. R. (2001). Dynamic pattern formation in a vesicle-generating microfluidic device. *Physical Review Letters*, *86*, 4163–4166. https://doi.org/10.1103/PhysRevLett.86.4163

Tomotika, S. (1934). On the instabilty of a cylindrical thread of a viscous liquid surrounded by another viscous fluid. *Proceedings of the Royal Society A: Mathematical, Physical and Engineering Sciences*, *146*, 322–337.

Tomotika, S. (1936). Breaking up of a drop of viscous liquid immersed in another

viscous fluid which is extending at a uniform rate. *Proceedings of the Royal Society A: Mathematical, Physical and Engineering Sciences*, *153*, 302–317.

Trinh, K. T. (2010). On The Critical Reynolds Number For Transition From Laminar To Turbulent Flow. *ArXiv E-Prints*, *1007*(0810), 1–39.

Unger, E. C., Matsunaga, T. O., McCreery, T., Schumann, P., Sweitzer, R., & Quigley, R. (2002). Therapeutic applications of microbubbles. *European Journal of Radiology*, *42*(2), 160–168. https://doi.org/10.1016/S0720-048X(01)00455-7

Unger, E. C., Porter, T., Culp, W., Labell, R., Matsunaga, T., & Zutshi, R. (2004). Therapeutic applications of lipid-coated microbubbles. *Advanced Drug Delivery Reviews*, *56*(9), 1291–1314. https://doi.org/10.1016/j.addr.2003.12.006

Uzma, N., Salar, B. M. K. M., Santhosh Kumar, B., Aziz, N., David, M. A., & Reddy, V. D. (2008). Impact of organic solvents and environmental pollutants on the physiological function in petrol filling workers. *International Journal of Environmental Research and Public Health*, *5*(3), 139–146. https://doi.org/10.3390/ijerph2008050019

Vafaei, S., Borca-Tasciuc, T., Podowski, M. Z., Purkayastha, A., Ramanath, G., & Ajayan, P. M. (2006). Effect of nanoparticles on sessile droplet contact angle. *Nanotechnology*, *17*, 2523–2527. https://doi.org/10.1088/0957-4484/17/10/014

Verhaagen, B., & Fernández Rivas, D. (2016). Measuring cavitation and its cleaning

effect. *Ultrasonics Sonochemistry*, *29*, 619–628. https://doi.org/10.1016/j.ultsonch.2015.03.009

Verstappen, F. T. J., Bernards, J. A., & Kreuzer, F. (1977). Effects of pulmonary gas embolism on circulation and respiration in the dog. iII. excretion of venous gas bubbles by the lung. *Pflugers Arch*.

Visser, C. W., Kamperman, T., Karbaat, L. P., Lohse, D., & Karperien, M. (2018). In-air microfluidics enables rapid fabrication of emulsions, suspensions, and 3D modular (bio)materials. *Science Advances*, *4*, 1–9. https://doi.org/10.1126/sciadv.aao1175

Wan, J., Bick, A., Sullivan, M., & Stone, H. A. (2008). Controllable microfluidic production of microbubbles in water-in-oil emulsions and the formation of porous microparticles. *Advanced Materials*, *20*(17), 3314–3318. https://doi.org/10.1002/adma.200800628

Wang, L. Q., & Zhang, Y. X. (2009). Experimental Investigation of Bubble Formation in a Microfluidic T-Shaped Junction. *Nanoscale and Microscale Thermophysical Engineering*, *13*(4), 228–242. https://doi.org/Doi 10.1080/15567260903276999

Wang, M., & Sultana, N. (2012). PHBV/PLLA-based composite scaffolds fabricated using an emulsion freezing/freeze-drying technique for bone tissue engineering: surface modification and in vitro biological evaluation. *Biofabrication*, *4*(1), 15003.

Wang, S., Dhanaliwala, A. H., & Hossack, J. A. (2012). Modeling Microbubble Production Rates from Expanding Nozzle Flow-Focusing Microfluidic Devices. *2012 IEEE International Ultrasonics Symposium*, *2*(1), 667–670. https://doi.org/10.1109/ULTSYM.2012.0166

Wang, Y., Li, P., Truong-Dinh Tran, T., Zhang, J., & Kong, L. (2016). *Manufacturing Techniques and Surface Engineering of Polymer Based Nanoparticles for Targeted Drug Delivery to Cancer*. *Nanomaterials* (Vol. 6). https://doi.org/10.3390/nano6020026

Wong, K. K., Huang, I., Kim, Y. R., Tang, H., Yang, E. S., Kwong, K. K., & Wu, E. X. (2004). In Vivo Study of Microbubbles As an MR Susceptibility Contrast Agent. *Magnetic Resonance in Medicine*, *452*(52), 445–452. https://doi.org/10.1002/mrm.20181

Xiong, R., Bai, M., & Chung, J. N. (2007). Formation of bubbles in a simple co-flowing micro-channel. *Journal of Micromechanics and Microengineering*, *17*(5), 1002–1011. https://doi.org/10.1088/0960-1317/17/5/021

Xu, J. H., Li, S. W., Wang, Y. J., & Luo, G. S. (2006a). Controllable gas-liquid phase flow patterns and monodisperse microbubbles in a microfluidic T-junction device. *Applied Physics Letters*, *88*(13), 22–25. https://doi.org/10.1063/1.2189570

Xu, J. H., Li, S. W., Wang, Y. J., & Luo, G. S. (2006b). Controllable gas-liquid phase flow patterns and monodisperse microbubbles in a microfluidic T-junction device. *Applied Physics Letters*, *88*(13), 10–13. https://doi.org/10.1063/1.2189570

Xu, Jian Hong, Li, S. W., Tan, J., & Luo, G. S. (2008). Correlations of droplet formation in T-junction microfluidic devices: from squeezing to dripping. *Microfluidics and Nanofluidics*, *5*, 711–717. https://doi.org/10.1007/s10404-008-0306-4

Xu, Q., Nakajima, M., Ichikawa, S., Nakamura, N., & Shiina, T. (2008a). A comparative study of microbubble generation by mechanical agitation and sonication. *Innovative Food Science & Emerging Technologies*, *9*(4), 489–494. https://doi.org/10.1016/j.ifset.2008.03.003

Xu, Q., Nakajima, M., Ichikawa, S., Nakamura, N., & Shiina, T. (2008b). A comparative study of microbubble generation by mechanical agitation and sonication. *Innovative Food Science & Emerging Technologies*, *9*(4), 489–494. https://doi.org/10.1016/j.ifset.2008.03.003

Yoon, D. H., Hasegawa, K., Kaneko, Y., Arakawa, T., Go, J. S., Sekiguchi, T., & Shoji, S. (2015). Formation of polymeric hollow microcapsules and microlenses using gas-in-organic-in-water droplets. *Micromachines*, *6*(5), 622–633. https://doi.org/10.3390/mi6050622

Zabow, G., Assi, F., Jenks, R., Prentiss, M., Zabow, G., Assi, F., … Prentiss, M. (2002). Guided microfluidics by electromagnetic capillary focusing. *Applied Physics Letters*, *80*, 1483–1485. https://doi.org/10.1063/1.1449531

Zambaux, M. F., Bonneaux, F., Gref, R., Maincent, P., Dellacherie, E., Alonso, M. J., … Vigneron, C. (1998). Influence of experimental parameters on the characteristics of poly(lactic acid) nanoparticles prepared by a double emulsion method.

Journal of Controlled Release, *50*(1), 31–40. https://doi.org/https://doi.org/10.1016/S0168-3659(97)00106-5

Zhang, F., He, C., Cao, L., Feng, W., Wang, H., Mo, X., & Wang, J. (2011). Fabrication of gelatin-hyaluronic acid hybrid scaffolds with tunable porous structures for soft tissue engineering. *International Journal of Biological Macromolecules*, *48*(3), 474–481. https://doi.org/10.1016/j.ijbiomac.2011.01.012

Zhang, X., Reagan, M. R., & Kaplan, D. L. (2009). Electrospun silk biomaterial scaffolds for regenerative medicine. *Advanced Drug Delivery Reviews*, *61*(12), 988–1006. https://doi.org/10.1016/j.addr.2009.07.005

Zhao, C.-X., & Middelberg, A. P. J. (2011). Two-phase microfluidic flows. *Chemical Engineering Science*, *66*(7), 1394–1411. https://doi.org/10.1016/j.ces.2010.08.038

Zhao, Y.-Z., Liang, H.-D., Mei, X.-G., & Halliwell, M. (2005). Preparation, characterization and in vivo observation of phospholipid-based gas-filled microbubbles containing hirudin. *Ultrasound in Medicine & Biology*, *31*(9), 1237–1243. https://doi.org/10.1016/j.ultrasmedbio.2005.05.007

Zhong, X., Crivoi, A., & Duan, F. (2015). Sessile nanofluid droplet drying. *Advances in Colloid and Interface Science*, *217*, 13–30. https://doi.org/10.1016/j.cis.2014.12.003

Zhu, P., Kong, T., Lei, L., Tian, X., Kang, Z., & Wang, L. (2016). Droplet breakup in

expansion- contraction microchannels. *Scientific Reports*, *6*, 1–11. https://doi.org/10.1038/srep21527

Zhu, P., Tang, X., Tian, Y., & Wang, L. (2016). Pinch-off of microfluidic droplets with oscillatory velocity of inner phase flow. *Scientific Reports*, *6*, 1–10. https://doi.org/10.1038/srep31436

Zúñiga, R. N., & Aguilera, J. M. (2008). Aerated food gels: fabrication and potential applications. *Trends in Food Science and Technology*, *19*(4), 176–187. https://doi.org/10.1016/j.tifs.2007.11.012